Pontificia Universidad Católica del Perú

Escuela de Posgrado

New insights on the empirical predictability of spectral indicators for PV performance

Tesis para obtener el grado académico de Doctor en Física que presenta:

Miguel Ángel Sevillano Bendezú

Asesores:

Prof. Dr. Jan Amaru Palomino Töfflinger

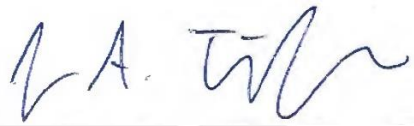### Prof. Dr. Juan de la Casa Higueras

Lima, 2023

Informe de Similitud

Yo, Jan Amaru Palomino Töfflinger, docente de la Escuela de Posgrado de la Pontificia Universidad Católica del Perú, y yo, Juan de la Casa Higueras, docente de la Universidad de Jaén, asesores de la tesis titulada *"New insights on the empirical predictability of spectral indicators for PV performance"* del autor Miguel Ángel Sevillano Bendezú, para la obtención del Doble Título de Doctor en Régimen de Cotutela Internacional, dejamos constancia de lo siguiente:

- El mencionado documento tiene un índice de puntuación de similitud de 22%, pero se tiene que omitir las referencias 50 y 106 del informe dado que estas son artículos elaborados por el mismo alumno y producto de la tesis doctoral. El índice de similitud, omitiendo las referencias señaladas, es de 8%, lo que está dentro del límite establecido. Así lo consigna el reporte de similitud emitido por el software Turnitin el 12 de septiembre de 2023.
- Hemos revisado con detalle dicho reporte y confirmamos que cada una de las coincidencias detectadas no constituyen plagio alguno.
- Las citas a otros autores y sus respectivas referencias cumplen con las pautas académicas.

Lugar y fecha: Lima, 12 de septiembre de 2023

Apellidos y nombres de asesor 1: Palomino Töfflinger, Jan Amaru	
DNI: 48866095	Firma:
ORCID: https://orcid.org/0000-0002-2076-4046	

Lugar y fecha: Jaén, 12 de septiembre de 2023

Apellidos y nombres de asesor 2: de la Casa Higueras, Juan	
DNI: 26001227A	Firma:
ORCID: https://orcid.org/0000-0002-1781-3417	

Acknowledgements

I express these profound thanks on behalf of my folks and me:

I have been extremely fortunate to have the permanent mentoring and accompaniment of outstanding mentors who helped and guided me early in my scientific research career. Firstly, I must thank Dr.rer.nat. J. Amaru Töffliger was my primary supervisor and best friend during the last three and a half years and my master's studies. Amaru stimulated my interest in photovoltaics research. He was always very attentive to sharing his experience, his investigative spirit, his outstanding contribution to my scientific writing, and doing everything possible to find funding for presentations, internships, publications, and lunches, among others. Thank you very much, Amaru. I extend these thanks to Gabi Töfflinger.

I also thank Dr. Juan de la Casa Higueras, who co-supervised my doctoral thesis work. Juan was not only a supervisor but even a spiritual guide. He has great intuition and experience to decide the best path for my doctoral work. I am particularly grateful to Juan for all the support, facilities, and hospitality I received in Jaén during my research stay at the University of Jaén. This stay was very productive, thanks to Juan's constant advice.

Another early mentor during this stage was Dr.rer.nat. Carolin Ulbrich, whom I thank for receiving me twice at the Competence Center Photovoltaics Berlin (PVcomB) of the Helmholtz Zentrum Berlin (Germany). My first stay at the PVcomB involved me in outdoor PV topics, with the seriousness and rigor that scientific research deserves. In the second stay, significant results in this thesis were obtained. I must also thank Dr. Mark Khenkin (also from PVComB), who directly supervised my work during my stay in Berlin. I am particularly indebted to Mark for his continued interest in my work and for sharing his enthusiasm for each finding revealed at each research stage during extensive discussions with his fresh insights.

Abstract

Accurate produced PV energy estimation is critical to business decisions under long-term investments in PV on a utility scale. PV energy yield is affected by different sites' specific conditions. The variability of the spectral distribution after temperature and irradiation is a site condition that impacts energy yield estimates. Evaluating the impact of the spectral irradiance distribution on the PV performance generally requires accurate information about the PV device's spectral response and the site's measured spectra. Detailed spectral and device information may not always be available. This study analyzes the interrelations between device-dependent and device-independent energetic spectral indicators with spectral data from nine sites with different climates and latitudes, aiming to relax the requirement for detailed device and spectral information. First, an apparent correlation of each site's spectral distributions' yearly Average Photon Energy with the corresponding latitude is observed. As the commonly applied device-dependent spectral indicator, it can be observed that the monthly mismatch factors of all nine sites exhibit a global linear relationship with the monthly average photon energies. This linear relationship with measured spectral data provides a predictive character for each PV device technology by allowing the estimation of the annual spectral impact from the annual Average Photon Energy, potentially for any site. This work also analyzes the validity of the Spectral Average Useful Fraction and the Spectral Enhancement Factor as alternative device-dependent spectral indicators. These require average spectra and, thus, would reduce the calculation complexity for spectral indicators. Finally, the proposed method was validated qualitatively using synthetic spectral data from the National Solar Radiation Database. The trends of the scatter plot between the synthetic Spectral Mismatch Factor and the Average Photon Energy that follow the experimental linear regression give an idea of the proposed method's functionality, despite the synthetic data's uncertainties.

Resumen

La estimación precisa de la energía fotovoltaica producida es fundamental para las decisiones comerciales en el marco de inversiones a largo plazo en proyectos fotovoltaicos. El rendimiento de la energía fotovoltaica se ve afectado por las condiciones locales epecíficas. La variabilidad de la distribución espectral después de la temperatura y la irradiación es una condición del sitio que afecta las estimaciones de rendimiento energético. Uno de los desafíos al evaluar el impacto de la variabilidad espectral es reducir la complejidad del cálculo. Esto implica realizar una estimación precisa y rápida del impacto espectral con la mínima información requerida a priori. Con este fin, la presente tesis busca analizar las interrelaciones entre los indicadores espectrales energéticos dependientes e independientes del dispositivo fotovoltaico con datos espectrales de varios climas y latitudes en todo el mundo. Debido al enfoque reduccionista que proveen los indicadores espectrales, analizamos la dependencia de la distribución espectral representada por la energía fotónica promedio con la latitud en diferentes escalas de tiempo mensuales y anuales. Al analizar los indicadores espectrales dependientes del dispositivo, se destaca el *Spectral mismatch factor*, que exhibe una relación lineal global con el la energía fotónica promedio en una escala mensual. El análisis exhaustivo de esta relación con los datos espectrales medidos también proporciona un carácter predictivo al permitir el cálculo del impacto espectral anual a partir de la energía fotónica promedio anual, y por lo tanto tal relación lineal propone ser un modelo empírico para el cálculo directo y sencillo del impacto espectral anual. Adicionalmente, analizamos la validez de manera global de dos indicadores espectrales dependientes del dispositivo, el *Spectral Enhancement Factor* y el *Spectral Average Useful Fraction* para los sitios seleccionados. Con ello se busca ofrecer un catálogo multiclimático

integrado de las interrelaciones de indicadores espectrales en escala de tiempo anual y mensual. Finalmente, se realizó una validación cualitativa del método propuesto utilizando datos espectrales sintéticos de la *National Solar Radiation Database*. Las tendencias de los *Spectral mismatch factor* y *Average Photon Energy* anuales basados en data espectral sintética siguen a la regresión lineal experimental y por ende, dan una idea de la funcionalidad del método propuesto, pese a las incertidumbres propias de la data espectral sintética.

Contents

1. Introduction

1.1. General introduction

In the upcoming decades, solar PV energy production is anticipated to continue to increase. Accordingly, the installed capacity is predicted to rise to around 5,200 GW by 2030 and exceed 14,000 GW by 2050, mainly in utility-scale power [1]. By speeding up the global energy transition and lowering annual CO_2 emissions, this increase attempts to reduce the rate of temperature rise brought on by global warming. It is also crucial for long-term energy security, price stability, and national resilience, aligning with some sustainable development agenda goals [1,2]. To achieve this, the PV market must develop to a mature level, ensuring investors' confidence and promoting the bankability of PV projects [3–5]. For instance, based on accurate yield projections in a particular environment, the appropriate selection of PV module technology for PV projects in a specific area may be of the utmost importance for investors and developers [6]. In recent years, yield estimations in PV projects have been increasingly rated according to their output energy yield under local operating conditions instead of by their power at standard test conditions (STC) [6–10]. Fluctuations in the solar spectral distribution are regarded as one of the influencing factors on PV module performance, along with variations in irradiance and temperature. This makes the lifetime energy yield prediction and the PV module energy rating susceptible to impacts by spectral fluctuations [6,11].

Small percentages of yield estimation error, such as those related to spectral effects over decades of operation, would affect the profit or loss by billions of euros [12–15]. In this context, researchers from around the world have shared their results regarding the spectral impact on various PV technologies. Qualitatively, compared to materials with smaller bandgaps, wide bandgap PV materials are more sensitive to spectrum changes [16]. The Average Photon Energy (APE) is the most common way to represent the spectral distribution. When compared to the AM1.5G spectrum, APE can show how blue- or red-shifted a solar spectrum is [17,18]. For sites with bluer spectra, cell technologies based on broad

bandgap absorber material present gains with regard to their STC efficiency, while those based on narrow bandgap present losses, and vice versa [6]. However, having accurate information on the spectral impact benefits optimizing some upstream processes, including conceptualizing, designing, and producing PV modules. Additionally, estimating the spectral impact accurately is essential for activities in the field, such as PV energy generation assessment and prediction. For instance, since its efficiency rose from 3.8 in 2009 to 25.5% in 2023, perovskite solar cells have impressively gained prominence [19–22]. In recent years it has also shown its attractiveness as a top subcell in tandem cells due to its tunable bandgap [23–25], reaching in this configuration efficiencies of up to 31.3% [22]. Therefore, the spectral behavior of these types of tandems and the subcells that compose them greatly interest the PV community since they contribute to closing the gap between downstream and upstream stakeholders In this technology by optimizing processes from PV module conceptualization to the expected generated energy in the field [26]. Spectral evaluation, therefore, is still an open topic for discussion and analysis. The spectral impact, for instance, can be estimated using the short circuit current or computed using sun spectra. In the case of the short circuit current, isolating the spectrum impacts from temperature impact or the effect of the Angle of Incidence is challenging [27,28]. One of the most critical aspects in characterizing spectral impact on PV performance is the limited availability of experimental spectral information [11]. Furthermore, concerning the available spectral information, most spectroradiometers offer a limited range of wavelengths, which increases the uncertainty in calculating the spectral impact, according to Dirnberger et al. (2015) [29]. One strategy to obtain a broader range of wavelengths is through extrapolation based on the AM1.5G spectrum of spectra measured over a limited range. These extrapolations occur in the ultraviolet region in Neves et al. (2021) [30] from 280 to 350 nm and infrared between 1100 to 4000 nm in Martin and Ruiz (1999) [31]. However, there is yet little information regarding the accuracy of these two methods. Additionally, determining the spectral distribution variation based solely on individual physical parameters is quite complex because it depends on the specific conditions of the location, such as latitude, climate, orientation, diffuse irradiation, albedo, atmospheric components, and cloud cover [32–34]. In this sense, the most popular PV energy yield modeling software offer simplified methods for calculating the spectral impact based on empirical formulas using atmospheric properties [35–41]. However, one of the main limitations when assessing

the spectral impact with empirical methods arises from the scarcity of validation studies of these methods for different climates and latitudes [42,43]. Knowing how the spectral distribution variation depends on different parameters has led to the development of empirical and physical models with varying degrees of complexity to obtain synthetic spectra that allow a spectral characterization with high spatial resolution [34,44–49]. Although synthetic spectra have reached good approximations in clear sky conditions, they still present considerable uncertainties in cloudy-sky conditions [50,51].

Some drawbacks become evident when comparing the results about the PV spectral impact in different locations and times, making it difficult to find a universal formula for the spectral impact: On the one hand, the different time scales, such as instantaneous, monthly, and annual, for which the energetic evaluation is carried out [11], do not allow a direct comparison of the results. On the other hand, different spectral indicators with specific assumptions and associated uncertainties also make finding a general rule even harder. Rodrigo et al. (2017) [52] propose classifying spectral indicators into two groups on the one hand, those independent of the PV device, such as the APE, and, on the other hand, those dependent on information from the PV device to be evaluated. The device-dependent index considered the most accurate to date is the Spectral Mismatch Factor (MM) [53], whose value represents a fraction of the spectral gains or losses in the photocurrent. According to Dirnberger et al. (2015) [29], precise experimental procedures and data, such as a defined PV technology's spectral response (SR) and a set of wide wavelength range recorded spectral irradiances, are necessary to enable a reliable and accurate estimate. Faced with this, the search for a direct quantification of spectral gains and losses based on spectral indicators requiring minimal information has been one of the approaches to evaluating the spectral impact in recent times.

Ishii et al. (2013) [54] reported the experimental relationship between instantaneous MM and APE for different photovoltaic technologies in Kusatsu (Japan). In that study, they proposed a polynomial relationship of variable degree depending on the PV technology between the APE and MM. One of the aspects that allowed a significant advance to the easy estimation of the spectral impact on PV performance was the statistical verification of APE uniqueness for specific locations, initially in Kusatsu and extending to other regions in Japan through the construction of the Percentage to the Total

Irradiance methodology which produces an average spectrum in 71 spectral bands in the range 350 to 1050 nm described in detail in [55,56]. With this criterion, Chantana et al. (2017) [57] showed a quasi-linear relationship between MM of various PV technologies and APE for 71 spectral bands between 350 to 1050 nm in Kusatsu. That work was expanded by Tsuji et al. (2018) [58] for a few more locations, obtaining a more comprehensive range of APEs.

In addition, the quasi-linear relationship using the Percentage to the Total Irradiance methodology was also found when taking different reference devices in calculating the MM [59]. These studies were extended to other regions of Japan, such as Tsukuba, Miyasaki, Naganuma Gifu, Tosu, and Okinoerabu [27,60]. Additionally, expanding the scope for a spectral range from 350 to 1700 nm and eight different SRs. Recently, Takeguchi et al. (2022) [61] presented a set of contour plots to estimate the spectral gain or loss based on an average energetic APE and its standard deviation for seven different SRs. This result was possible by using the MM and APE relationship found in previous studies mentioned above, also assuming a Gaussian distribution for the APE as a function of the available irradiance and extrapolating spectra based on a polynomial fit of the APE for different spectral ranges and in five locations worldwide.

For Jaen, Spain, Nofuentes et al. (2014) [62] in-depth examined the association between the instantaneous APE and an index that is practically the same as the MM. One year later, When comparing instantaneous APE and MM, Dirnberger et al. (2015a) [11] in Freiburg, Germany, ruled out any bijective association between MM and APE but also demonstrated the benefit of directly assessing the spectrum impact through the monthly irradiance-weighted APE. Neves et al. (2021) [30] recently identified linear regressions between monthly MM and APE for two locations in Brazil.

A general linear relationship between MM and APE has not yet been confirmed on an energetic time scale encompassing many latitudes and climates on a global scale, despite the local reports of those linear empirical associations between MM and APE mentioned above. The present work analyzes the spectral distribution and its impact on different PV technologies based on experimental spectral data in various climates and latitudes worldwide. Based on this data, it analyses the interrelationships between different energetic spectral indicators according to three levels of spectral information on the PV device:

4

no spectral information, only knowing the bandgap, and knowing the SR. One of the objectives is to present a general relationship between the monthly MM and APE. The latter gives rise to an empirical method for determining the annual spectral impact based on information from the annual APE. In this way, this work makes a comprehensive study of the straightforward determination of spectral effects on PV energy yield with accuracy depending on the PV technology through the interrelation of different spectral indicators according to the available information about the PV device.

1.2. Research objectives and hypotheses

The objectives and research hypotheses of this thesis are summarized below.

1.2.1 Research Hypothesis

- There is a global and linear relationship between the MM and the APE.

- It is possible to predict annual (monthly) MM using solely annual (monthly) APE from experimental spectral data.

- Synthetic spectral data from the NSRDB predicts the spectral distribution for Lima using the APE.

- Synthetic spectral data from the NSRDB verifies the proposed empirical method

1.2.2. General objective

This work aims to develop a simplified and global procedure for determining the annual (monthly) spectral impact knowing the annual (monthly) APE for six different photovoltaic technologies from experimental spectral data from nine sites worldwide.

1.2.3. Specific objectives

- To analyze the interrelationships between the most representative spectral indicators based on the experimental spectral data of the nine sites worldwide in different time scales (daily, monthly, and annual).

- To validate synthetic spectral data from NSRDB in Lima-Peru using the APE.

- To analyze the spectral indicators on the synthetic spectral data and study their validity in the proposed empirical method.

1.3. Outline

The document is organized as follows:

Chapter 2 describes the fundamentals related to the impact of the varying spectral distribution on PV performance. This includes the description of the main spectral distribution atmospheric parameters, as well as the link between the spectral sensitivity of PV devices and the site's spectral distribution. Additionally, chapter 2 describes the main spectral indicators this work focuses on, including both PV-device-dependent and -independent spectral indicators.

Chapter 3 presents the experimental and synthetic spectral data sets, the methodology used in the present work, and the spectral data analysis methods.

Chapter 4 analyzes the PV device's dependent and independent spectral indicators for one year based on experimental data. This analysis seeks to show the main trends of these spectral indicators throughout the year for different latitudes and climates worldwide.

Once the main annual trends are identified, chapter 5 shows the interrelationships between the PV device's dependent and independent spectral indicators in different time scales. Chapter 6 proposes an empirical method based on the interrelation between MM and APE that has the potential to predict the monthly or annual spectral impact knowing only the monthly or annual APE, respectively. This proposal is tested for two more locations in Brazil. Chapter 7 shows the results of validating the method proposed in chapter 6 with synthetic data for 14 sites covering a broad latitude domain.

2. Fundamentals

2.1. Introduction

The incoming irradiation from the sun or, equivalently, because of the quantum nature of the light, the stream of photons delivered by the sun, interacts in multiple ways with the atmosphere, with several phenomena occurring simultaneously [34,63–65]. Incoming solar irradiance in the atmosphere gives rise to thermal, ionizing, and chemical phenomena. However, solar irradiance is also affected by atmospheric constituents. The atmosphere's mixture of gases and dust particles affects solar irradiance mainly by reflections, scatterings, and absorptions at different wavelengths extended for several thousand kilometers.

The variability of the traveled path and atmospheric conditions is mainly reflected in changes in the spectral distribution of the solar radiation that reaches the Earth's surface and affects the energy harvest of a PV device [34,66]. The photons that reach the earth do so with an energy ε related to the wavelength λ of irradiation through a fundamental equation in Quantum Mechanics called the Planck relation [67] as given in Equation 1.

$$\varepsilon = \frac{hc}{\lambda} \tag{1}$$

hc being the product of the Planck's constant by the light speed (1.986×10^{-16} J nm or 1239.842 eV nm). The quantum solar energy conversion in a PV device after absorbing and emitting incident photons gives rise to useful work [65]. One way to evaluate this conversion's efficiency or measure this device's spectral quality is through the External Quantum Efficiency (EQE), defined as the ratio of collected charge carriers to the number of energetic photons incident on the PV device`s surface [68]. Therefore, the EQE is affected by the different mechanisms involved during the PV conversion, which ultimately also impact the PV device's spectral sensitivity. On the other hand, another index that describes the sensitivity of a photosensitive device is the Spectral Response which alternatively allows accessing information about the EQE. This index quantifies the ability of a PV device to absorb sunlight and convert it into electric current without considering intermediate microscopic phenomena, as shown

in Equation 2 [69–71]. Where $I_{ph}(\lambda)$ represents the generated photocurrent and $G(\lambda)$ the spectral irradiance for a specific wavelength λ.

$$SR(\lambda) = \frac{I_{ph}(\lambda)}{G(\lambda)} \tag{2}$$

The SR and the EQE are related through Equation S3.

$$SR(\lambda) = \frac{q\lambda}{hc} EQE(\lambda) \tag{3}$$

2.2. Spectral indicators

This sub-chapter presents figures of merit that quantify the spectral influences on PV performance, referring to them as spectral indicators. For this purpose, this work focuses on the Rodrigo et al. (2017) [52] classification of spectral indicators. This approach classifies spectral indicators into PV device-independent and -dependent indicators. The latter refers to the information dependence of the PV device, which relates mainly to the bandgap and the SR or EQE.

The most popular device-independent indicator to represent the spectral distribution with a scalar value is the APE (in eV). This device-independent indicator initially presented in Jardine et al. (2002) [17] and Williams et al. (2003) [18] allows a direct way to determine the blueness or redness of a solar spectrum concerning the AM1.5G spectrum [72]. The APE (in eV) is defined as the integrated spectral irradiance of the solar spectrum divided by the integrated photon flux density, as shown in Equation 4.

$$APE = \frac{\int_{350}^{1050} G_{exp}(\lambda)d\lambda}{q \int_{350}^{1050} \phi_{exp}(\lambda)d\lambda} \tag{4}$$

$$\phi_{exp}(\lambda) = G_{exp}(\lambda)\frac{\lambda}{hc} \tag{5}$$

Where $G_{exp}(\lambda)$ (in Wm^{-2}nm^{-1}) is the wavelength-dependent measured irradiance, and $\phi_{exp}(\lambda)$ is the associated photon flux density (in m^{-2}nm^{-1}s^{-1}), as described by Equation 5. The APE for the AM1.5G spectrum ($APE_{AM1.5G}$) in the spectral range of 350 nm – 1050 nm is 1.876 eV. Therefore, a spectrum with an APE higher than this value is considered blue-rich, while a spectrum with an APE less than $APE_{AM1.5G}$ is considered red-rich.

Another indicator agnostic of the PV device that allows the evaluation of the blueness of the solar spectrum is the so-called Blue Fraction (BF) [52,73]. This indicator assumes that the blue portion of the spectrum is below 650 nm. Therefore, its definition represents the fraction of blue irradiation described by Equation 6.

$$BF = \frac{\int_{350}^{650} G_{exp}(\lambda)d\lambda}{\int_{350}^{1050} G_{exp}(\lambda)d\lambda} \tag{6}$$

The BF for the AM1.5 G ($BF_{AM1.5G}$) spectrum is 0.519; therefore, a spectrum with a BF higher than $BF_{AM1.5G}$ corresponds to a bluer spectrum than the standard one, while a BF below $BF_{AM1.5G}$ indicates a reddened spectrum.

The device-dependent Useful Fraction (UF) indicator is defined as the ratio of the irradiance within the spectrally responsive range of the solar cell to the total measured irradiance [74]. The device-dependent index known as the Integrated Useful Fraction Ratio [52] UF/UF^* is the ratio between the UF of the measured spectrum and the UF of the reference spectrum AM1.5G (UF^*) as shown in Equation 7.

$$\frac{UF}{UF^*} = \frac{\int_{280}^{\lambda g} G_{exp}(\lambda)d\lambda}{\int_{280}^{\lambda g} G_{ref}(\lambda)d\lambda} \frac{\int_{280}^{4000} G_{ref}(\lambda)d\lambda}{\int_{280}^{4000} G_{exp}(\lambda)d\lambda} \tag{7}$$

Where λg represents the wavelength associated with the bandgap. Additionally, G_{ref} represents the integrated irradiance of the AM1.5G spectrum.

One of the most representative and widespread indicators of spectral impact is the Spectral Mismatch Factor (MM) according to the standard IEC 60904-7 [75], as given in Equation 8.

$$MM = \frac{\int_{280}^{4000} \mathrm{SR}(\lambda)G_{exp}(\lambda)d\lambda}{\int_{280}^{4000} \mathrm{SR}(\lambda)G_{ref}(\lambda)d\lambda} \frac{\int_{280}^{4000} G_{ref}(\lambda)d\lambda}{\int_{280}^{4000} G_{exp}(\lambda)d\lambda} \tag{8}$$

This device-dependent indicator directly represents a specific PV device's spectral gain or loss under operating conditions relative to standard spectral conditions such as the AM1.5G spectrum. Therefore, MM above one indicates a spectral gain, while MM below one means a spectral loss.

The UF/UF^* expression reduces to Equation 8 when considering a unitary SR (or in general, a flat SR). This can lead to the misconception that a device with such a property has the appropriate characteristics

to absorb light efficiently, which it does not. This is because a unitary SR through Equation 3 translates into a hyperbolic EQE previously reported in [76], far from that of a realistic PV absorbent material.

To estimate their impact in terms of energy evaluation, the instantaneous indicators are averaged by irradiance-weighted average indicators using Equation 9. Such averaging condenses spectral indicators over time, giving their energetic nature.

$$< KPI >_T = \frac{\sum_{i=1}^{N_T} KPI_i \times G_i}{\sum_{i=1}^{N_T} G_i} \qquad (9)$$

Where a Key Performance Indicator (KPI) represents our instantaneous spectral indicator, such as the APE, BF, UF/UF^* and MM. G_i is the integrated spectral irradiance associated with the spectral index, T is the period to consider, such as daily, monthly or annual, and N_T represents the total number of measurements in the period considered. It should be noted that UF/UF^*, when irradiance-weighted, is the Integrated Useful Fraction Ratio (IUF/IUF^*) [52]. The essence of UF/UF^* expressed by Equation 7 and its corresponding energy formulation in Equation 9 (IUF/IUF^*) is to indicate the portion of useful irradiance for the PV device relative to the reference spectrum portion of useful irradiance. If these indicators are higher than 1, the measured spectrum has a higher possible useful irradiance than the reference one. However, this denominated useful fraction of irradiance overestimates the effective irradiance that the device absorbs by its SR, which makes it inaccurate to determine the spectral impact [77].

Additionally, this work adapted two spectral indicators proposed by Rodrigo et al., (2019) [77], which are calculated based on an average spectrum weighted to the irradiance given in Equation 10. This adaptation focuses the calculation on the averaged irradiance spectrum, thus reducing the computational effort of calculating additional averages and integrals.

$$< G_{exp} > (\lambda) = \frac{\sum_{i=1}^{N_T} G_{exp}(\lambda)_i \times G_i}{\sum_{i=1}^{N_T} G_i} \qquad (10)$$

The first index refers to the adapted Spectral Average Useful Fraction (for simplicity, it is kept the notation $SAUF$), which presents the same expression as IUF/IUF^* changing the instantaneous measured spectrum $G_{exp}(\lambda)$ by the $< G_{exp} > (\lambda)$ as represented in Equation 11.

$$SAUF = \frac{\int_{280}^{\lambda g} <G_{exp}>(\lambda)d\lambda}{\int_{280}^{\lambda g} G_{ref}(\lambda)d\lambda} \frac{\int_{280}^{4000} G_{ref}(\lambda)d\lambda}{\int_{280}^{4000} <G_{exp}>(\lambda)d\lambda} \qquad (11)$$

While the adapted Spectral Enhancement Factor (for simplicity, it is also kept the notation SEF) has the same expression as the MM, the only difference is replacing $G(\lambda)$ with the $<G>(\lambda)$ as expressed in Equation 12.

$$SEF = \frac{\int_{280}^{4000} SR(\lambda)<G_{exp}>(\lambda)d\lambda}{\int_{280}^{4000} SR(\lambda)G_{ref}(\lambda)d\lambda} \frac{\int_{280}^{4000} G_{ref}(\lambda)d\lambda}{\int_{280}^{4000} <G_{exp}>(\lambda)d\lambda} \qquad (12)$$

This simplified way of computing energy spectral indicators would reduce the extensive computation required to solve many instantaneous integrals [52].

Since one of the main aims of this work is to assess the interrelationships of the different spectral indicators, for a deeper analysis, it is also helpful to add the equations of some spectral indicators as a function of the energy and photon flux. Thus, it is possible to redefine the BF in terms of energy using Equations 1, 5, and 6.

$$BF = \frac{\int_{1.91}^{3.54} \varepsilon \phi_{exp}(\varepsilon)d\varepsilon}{\int_{1.18}^{3.54} \varepsilon \phi_{exp}(\varepsilon)d\varepsilon} \qquad (10)$$

In the same way, UF/UF^* is rewritten through Equations 1, 5, and 7.

$$\frac{UF}{UF^*} = \left(\frac{\int_{0.31}^{4.43} \varepsilon \phi_{exp}(\varepsilon)d\varepsilon}{\int_{\varepsilon_0}^{4.43} \varepsilon \phi_{exp}(\varepsilon)d\varepsilon} \right) \left(\frac{\int_{0.31}^{4.43} \varepsilon \phi_{ref}(\varepsilon)d\varepsilon}{\int_{\varepsilon_0}^{4.43} \varepsilon \phi_{ref}(\varepsilon)d\varepsilon} \right) \qquad (11)$$

Notice that in Equation 11, the term on the right is constant, therefore by comparing equations 10 and 11 in their indefinite form (without integration limits), then mathematically, $UF/UF^* \propto BF$.

The APE from Equations 1, 4 and 5, is also rewritten, as shown in Equation 12.

$$APE = \frac{\int_{1.18}^{3.54} \varepsilon \phi_{exp}(\varepsilon)d\varepsilon}{\int_{1.18}^{3.54} \phi_{exp}(\varepsilon)d\varepsilon} \qquad (12)$$

Additionally, the MM can be rewritten using Equations 1, 5, and 8. Thus, Equation 13 shows MM as a function of energy.

$$MM = \frac{\int_{0.31}^{4,43} QE_r(\varepsilon)\phi_{exp}(\varepsilon)d\varepsilon}{\int_{0.31}^{4.43} QE_r(\varepsilon)\phi_{ref}(\varepsilon)d\varepsilon} \frac{\int_{0.31}^{4,43} \varepsilon\phi_{ref}(\varepsilon)d\varepsilon}{\int_{0.31}^{4.43} \varepsilon\phi_{exp}(\varepsilon)d\varepsilon} \tag{13}$$

Rearranging Equation 13 conveniently and considering an ideal case of perfect absorbent material $(EQE = 1)$ using Equation 3 gives rise to Equation 14.

$$MM_{ideal} = \left(\frac{\int_{0.31}^{4,43} \phi_{exp}(\varepsilon)d\varepsilon}{\int_{0.31}^{4.43} \varepsilon\phi_{exp}(\varepsilon)d\varepsilon}\right)\left(\frac{\int_{0.31}^{4,43} \varepsilon\phi_{ref}(\varepsilon)d\varepsilon}{\int_{0.31}^{4.43} \phi_{ref}(\varepsilon)d\varepsilon}\right) \tag{14}$$

The term on the right in equation 14 is a constant; therefore, when comparing equations 12 and 14 in their undefined form (indefinite integrals) follows that $MM_{ideal} \propto APE^{-1}$. For the range of about 1.78 to 1.92 eV of monthly weighted APEs considered in this work, MM_{ideal} is approximately linear with the APE in their undefined form.

2.3. Summary

This chapter presented the most relevant definitions and expressions used in the present work. A PV device acts as a photon-to-charge-carrier converter by its associated EQE. Photons have different energies covering a wide spectral range. Since the efficiency with which each photon is converted into a charge carrier is a function of its energy (or wavelength), a variable spectral distribution leads to a variable number of charge carriers generated, i.e., a variable-generated photocurrent. Usually, the variability of the spectral distribution and the effect on the generated current are quantified using the AM1.5G (STC) spectrum as a reference. Spectral indicators presented are separated into two groups following Rodrigo et al. (2017) methodology as dependent (MM, IUF/IUF^*, $SAUF$, SEF) and independent (APE, BF) of the PV device. This chapter presented the most widely used spectral indicators in the PV community in their formulation based on wavelength and photon energy. These spectral indicators will be calculated using experimental and synthetic spectral data from worldwide locations.

3. Spectral datasets and methods

3.1 Introduction

This work piled experimental ground-based spectral data sets from nine locations and synthetic spectral data from 14 locations worldwide, covering various latitudes, climates, and installation conditions. This chapter describes these spectral data sets and the spectral characteristics of the photovoltaic technologies on which this work focuses. In addition, the data processing methods used that allow comparing results are described. This implies the extrapolation of spectra to have spectra in the same wide spectral range (280 to 4000nm) for each site provided with experimental spectral data.

3.2. Experimental spectral datasets
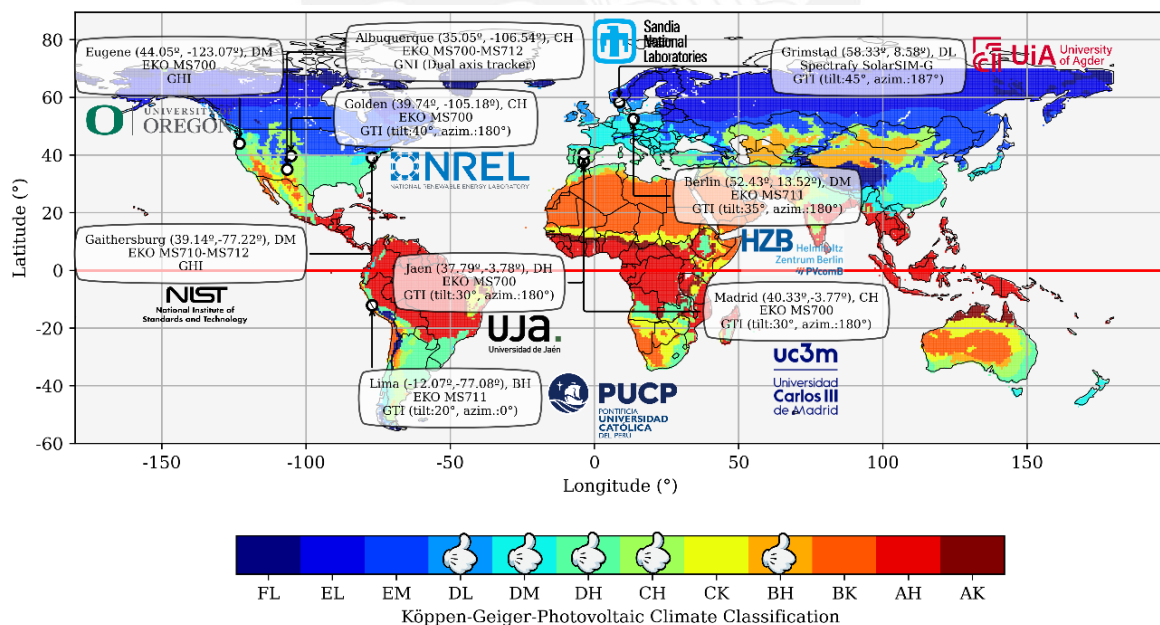
Figure 1. Köppen-Geiger-Photovoltaic (KGPV) [78] climate classification map with the nine selected sites worldwide, covering 5 of the 12 climate classifications. KGPV Zones are mainly classified according to their temperature-precipitation conditions (first letter) in Tropical (A), Desert (B), Steppe (C), Temperate (D), Cold (E), and Polar (F). In contrast, the second classification criterion is the irradiation (second letter): Very High (K), High (H), Medium (M), and Low (L) irradiation. The open dataset has a spatial resolution of 0.5° × 0.5° taken from [79].

These locations and the specific equipment characteristics and approximate climate type can be visualized with the help of the Köppen-Geiger-Photovoltaic climate classification map [78,79], as shown in Figure 1. Each box in Figure 1 presents the location's name, latitude, longitude, approximate KGPV climate classification, the spectroradiometer model, and the orientation plane. In this way, these nine locations describe a representative variety of five climates available concerning the potential PV performance worldwide. The selected data set cover exactly one year with a high spectral data availability at the site. At most sites, a full-data day has more than 90% data availability during the hours of sunlight.

Additionally, Table 1 summarizes additional characteristics of each spectral sensor, including collection period, original spectral range, and equipment.

Table 1. Summary of the characteristics of each installation. Spectral data correspond to Global Tilted Irradiance (GTI), Global Horizontal Irradiance (GHI), and Global Normal Irradiance (GNI). When necessary, the original spectral range was limited to 1050 nm to ensure the same pre-processing procedure in all sites. After that, the resulting spectra were extrapolated to a range of 280 to 4000 nm.

Location and approximate KGPV climate Latitude [source]	Type and tilt angle	Spectral sensor	Original spectral range (nm)	Data collection period	Filter by the angle of incidence <
Grimstad 58.33° DL [80,81]	GTI 45°	Spectrafy SolarSIM-G	280 – 4000	Jun-2020 – May-2021	60°
Berlin 52.43° DM [b]	GTI 35°	EKO MS711	300 – 1100	Jun-2019 – May-2020	60°
Albuquerque 35.05° CH [82]	GNI	EKO MS700-MS712	350 – 1700	Jan-2014– Dec-2014	90°
Gaithersburg 39.14° DM [83]	GHI	EKO MS710-MS712	350 – 1100	Jun-2015 – May-2016	90°

Madrid 40.33° CH [ᶜ]	GTI 30°	EKO MS700	350 – 1050	Jun-2015 – May-2016	60°
Eugene 44.05° DM [84]	GHI	EKO MS700	335.4 – 1059	Jun-2018 – May-2019	90°
Jaen DH 37.79° [ᶜ]	GTI 30°	EKO MS700	350 – 1050	Jun-2016 – May-2017	60°
Golden 39.74° CH [85]	GTI 40°	EKO MS700	343 – 1062.8	Jun-2020 – May-2021	60°
Lima -12.07 BH [ᵃ]	GTI 20°	EKO MS711	300 – 1100	Jun-2020 – May-2021	60°

Global spectral irradiance is generally measured by spectroradiometer sensors in continuous outdoor exposure across the sky hemisphere. These can be, to name a few, grating spectroradiometers such as the EKO MS-7XX (10, 11, 12) and filter-type such as the SolarSIM-G. This last spectroradiometer measures the spectrum at nine different wavelengths and then reconstructs a spectrum from 280 to 4000 nm from atmospheric models [81,86]. The spectral data sets considered three different configurations of global spectral irradiance measurements: measurements in a horizontal plane corresponding to Global Irradiance (GHI, in W/m^2), in a tilted plane coinciding with a fixed plane-of-array, represented here as Global Tilted Irradiance (GTI, in W/m^2), and an experimental campaign in two-axis tracking plane, corresponding to the Global Normal Irradiance (GNI, in W/m^2).

3.3. Synthetic spectral datasets
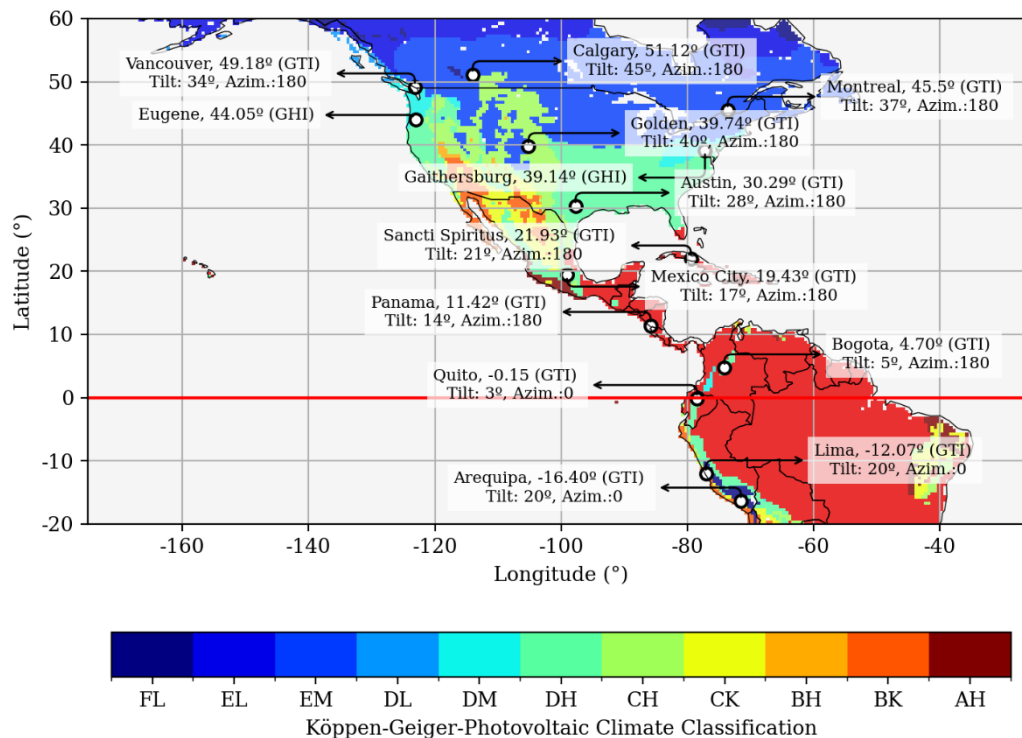
Figure 2. The 14 selected sites for synthetic spectral data from the NSRDB in the available region of spectra on demand. Latitude and the spectroradiometer installation tilt and azimuth angles are indicated at each location.

The National Solar Radiation Database (NSRDB) [47] provided synthetic spectral data on demand for the sites in Figure 2. These synthetic spectra are based on the Fast All-sky Radiation Model for Solar applications with Narrowband Irradiances on Tilted surfaces (FARMS-NIT) [46,87]. FARMS-NIT efficiently computes the Radiative Transfer Equation producing a spectral irradiance in all-sky conditions transposed to a tilted surface in an hourly resolution in wavelength steps from 0.5 to 5 nm and in the wavelength range from 280 to 4000 nm. The synthetic data for 2019 and the previous decade (2009 - 2018) in Lima (location in Figure 2) served for validating synthetic spectra with experimental spectral data from March 2019 to February 2020, as shown later. Additionally, the 2019 spectral data for the sites in Figure 2 was selected as representative synthetic spectral distributions worldwide covering a wide range of latitudes and climates. The titlt angles (optimum) and orientation in most of cases were taken from Jacobson et al. (2018) [88]. Synthetic spectral data from Eugene, Golden, Gaithersburg, and Lima preserve the same tilt angle and orientation as the experimental data.

3.4. Spectral data pre-processing

3.4.1. Spectra data filtering

Additionally, the following filters were applied to maximize the data quality. Experimental spectra with an integrated extrapolated irradiance of fewer than 5 W/m^2 and higher than 1500 W/m^2 were discarded, thus ruling out extreme over-irradiance events and spurious measurements. In addition, The experimental and synthetic GTI data sets were filtered by the angle of incidence (AoI) using pvlib python [89], discarding data for AoI > 60° as recommended by Dirnberger et al. (2015) [11]. The latter additionally allowed skipping data with a significant influence of larger Air Mass (AM) with predominant diffuse irradiation on the global spectral irradiance.

This filter was unnecessary for experimental GNI, while data for AoI > 90° for experimental GHI were discarded to preserve periods of the year in which the AoI is larger than 60°. Finally, when considering the AoI > 90° filter for experimental GTI, though not shown here, the results did not present significant changes.

3.4.2. Spectra extrapolation for the experimental spectral data

Cutting all measured spectra to the range between 300 nm and 1050 nm for all sites allowed for maintaining equal conditions and applying the same analysis procedure for the different locations, spectroradiometers, and measurement configurations. The extrapolation proposed by Neves et al. (2021) [30] was adapted and applied to enhance the spectral range in the ultraviolet region from 280 to 300 or, in a few cases, up to 350 nm, depending on the spectral range of the experimental data considered in Table 1. Applying the Martin and Ruiz extrapolation method extended the spectral range from 1050 to 4000 nm. The analysis to validate this last extrapolation in the spectral range from 1050 to 1700 nm for GHI, GTI, and GNI spectra resulted in a small statistical error, as shown in Figure 3.
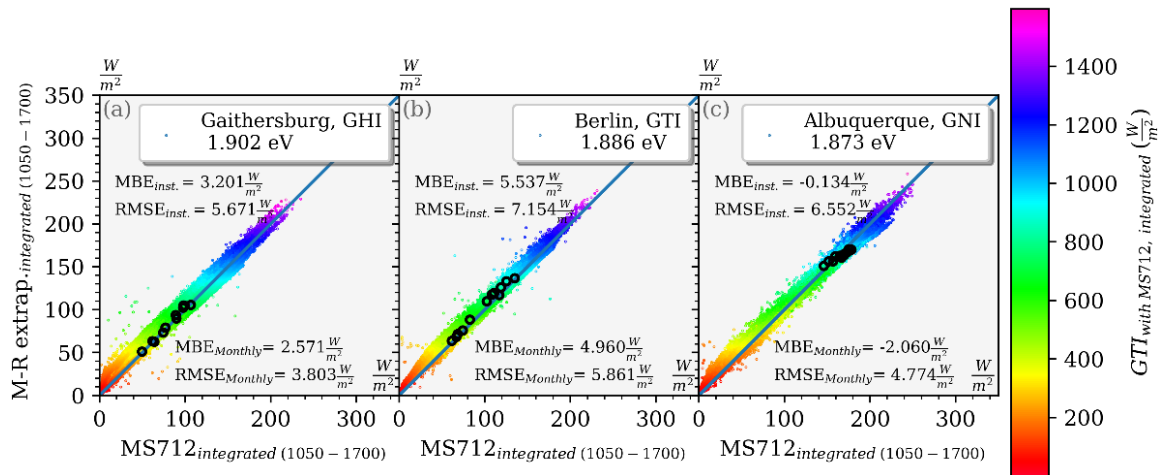
Figure 3. Assessment of Martin and Ruiz procedure for solar spectrum extrapolation in the range of 1050-1700 nm. The graphs show integrated irradiance in this spectral range from the extrapolated spectrum versus that in the experimentally measured spectrum (using MS712 spectrometer). The black circles show the $GTI_{with\ MS712,integrated}$ irradiance-weighted average monthly values. The line indicates linear regression of the instantaneous points.

3.5. PV technologies' spectral information

3.5.1. Experimental SRs
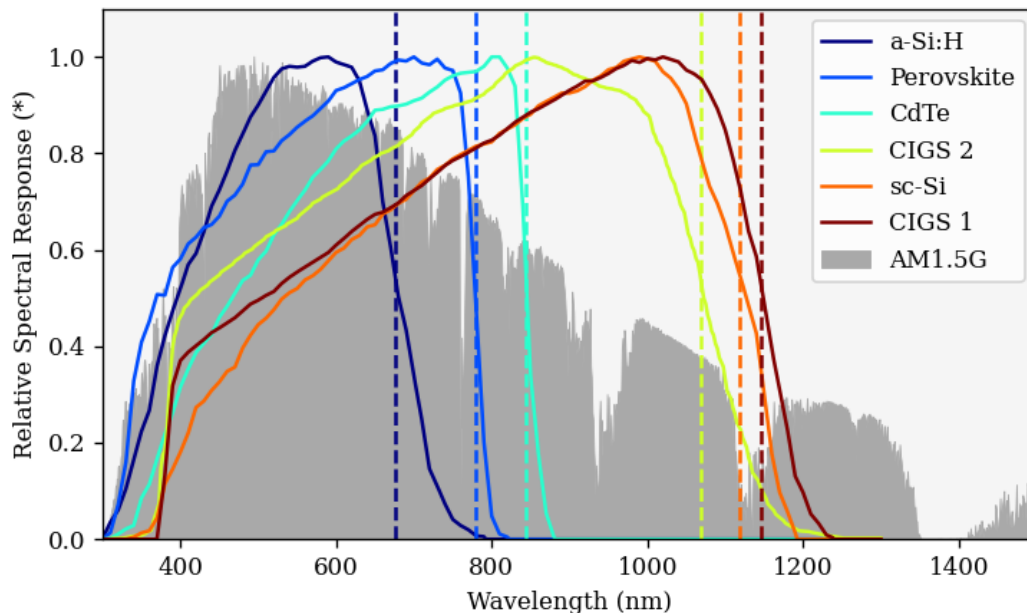
Figure 4. Relative Spectral response (relative SR) and the normalized spectral irradiance AM1.5G at the background.

Figure 4 shows this study's six representative relative SRs of different PV technologies, taken from Conde et al. (2021) [90]. It is also essential to keep in mind that the additional uncertainties due to the

varying SR between PV modules of one type, such as a-Si, CdTe, and c-Si, do not significantly impact the variability of the spectral impact [11]. Temperature-related uncertainties on the spectral effects on PV performance are also negligible [91]. Some technologies with tunable bandgaps, such as CIGS, can present significant differences in SR. This work used two different SRs for CIGS, besides an SR for a-Si:H, Perovskite, CdTe, and sc-Si, as depicted in Figure 4.

3.5.2. Derived EQE and SQ-Bandgaps derivation for six PV technologies
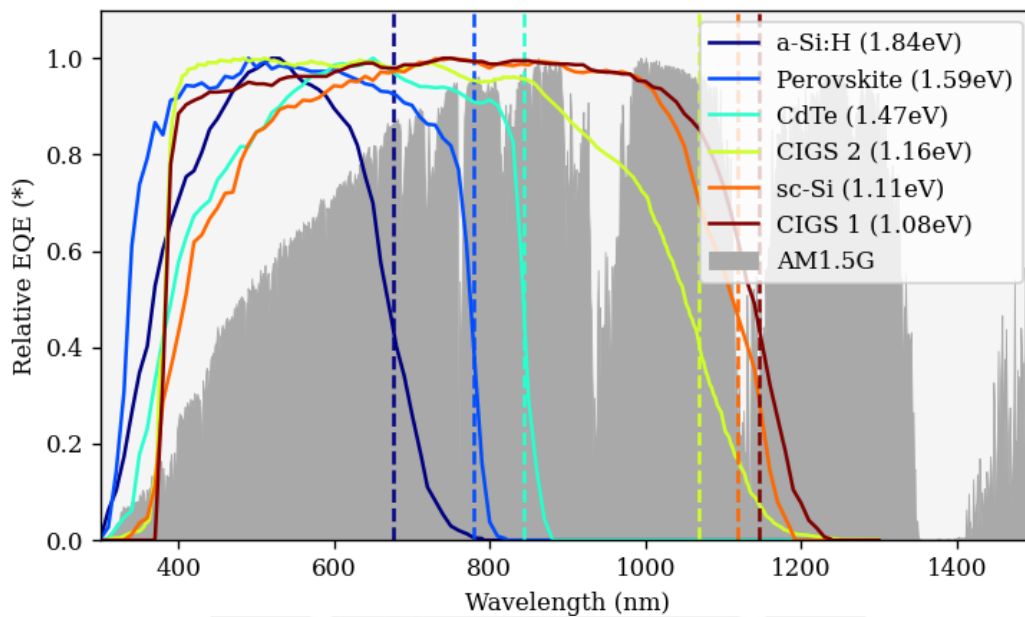
Figure 5. Relative External Quantum Efficiency (relative EQE) and the normalized photon flux AM1.5G. Dashed lines represent the SQ-Type bandgaps for each PV material calculated according to Rau et al. (2017) [91]

This work defines the relative EQE as the normalized EQE spectra calculated from relative SR data as shown in Figure 5. The associated EQE was calculated using the relation $EQE(\lambda) = (hc/q\lambda) \times SR(\lambda)$, with h being Planck's constant ($6.62607015 \times 10^{-34}$ m²kg/s), c the light speed in vacuum (2.9979×10^{8} m/s), λ (nm) the wavelength, and q (1.602×10^{-19} C) the elementary electric charge. The bandgaps were obtained through the methodology of Rau et al. (2017) [92], which provides a simplified and specific definition of the bandgap which results from calculating a bandgap that meets the assumptions of the Shockley-Queisser theory [93]. This calculated bandgap is called the Shockley-Queisser bandgap (SQ-Type bandgap); from here on, for simplicity, this work refers to it as bandgap.

Finally, the comparison between two variables that expect to have precisely the same results, a sample X_i and its predicted value Y_i, is carried out through two statistical indicators. The Root Mean Square Error ($RMSE$) shows the average deviation between N tuples of these two variables defined in Equation 15,

$$RMSE = \sqrt{\sum_{i=0}^{N} (X_i - Y_i)^2 / N} \tag{15}$$

and the Mean Bias Error (MBE) expressed by Equation 16, whose calculation represents the direction of the error bias.

$$MBE = \sum_{i=0}^{N} (X_i - Y_i) / N \tag{16}$$

3.6. Summary

This chapter presented the data sets and methods used to calculate and analyze the results of this thesis. The experimental spectral data correspond to nine locations worldwide, including Grimstad, Berlin, Eugene, Madrid, Golden, Gaithersburg, Jaen, Albuquerque, and Lima, covering various latitudes and climates. The synthetic spectral data presented here was provided by the NSRDB for 14 sites in the 280 to 4000nm range. Like experimental data, synthetic spectral data covers many latitudes and climates worldwide. Discarding spectral data with AoI greater than 60° for both sets allowed suppressing influences of high AM values on the results. Only the experimental spectral data required extrapolation due to its limited spectral range. The Neves et al. (2021) [30] extrapolation method was needed for the range of 280 to 300 or 350 in some cases, while the Martin and Ruiz (1998) [31] method for the range of 1050 to 4000nm. The synthetic spectral data presented a homogeneous range in all locations, so they did not require extrapolation. This chapter also showed six different spectral responses (a-Si: H, Perovskite, CdTe, CIGS 2, sc-Si, CIGS 1) on which this work focuses. The method proposed by Rau et al. (2017) [92] yielded the bandgap associated with each spectral response. In the next chapter, use will be made of the spectral indicators described in this chapter, following the proposal of Rodrigo et al. (2017) [52], which classifies them into two groups: independent and dependent on the PV device. Those

of the first group mainly aim to characterize the spectral distribution: BF and APE. On the other hand, those of the second group try to quantify the spectral impact depending on the degree of information available about the PV device: IUF/IUF^*, MM. In addition, this chapter presented two additional spectral indicators, SEF and $SAUF$, equivalent to irradiance weighted MM and IUF/IUF^*, respectively. Finally, it showed the most common spectral indicators in their photon energy-dependent form. This formulation will help analyze the interrelations between PV device-independent and -dependent spectral indicators in Chapter 5.

4. Annual behavior of PV-independent and -dependent spectral indicators worldwide based on measured spectra

4.1. Introduction

Commonly, the planning phase in a PV project requires prior knowledge and quantification of the energy generated annually, called yield-performance analysis. Such an analysis includes modeling the energy produced by a PV plant in the field for a year [6,94,95]. That energy analysis motivates to study the different influences that give rise to energy gains or losses, also called Performance loss rate [3,95,96]. The spectral indicators that characterize the spectral influences and the solar spectrum have an energetic character when weighted to the irradiance, as shown by Equation 9. Therefore these energetic spectral indicators throughout a year aim to quantitatively or qualitatively represent the spectral influences on the energy yield performance [11,30,70,90,97]. Generally, this analysis in different time scales is not widely disseminated. The monthly and annual parameters reported, such as MM and APE, are not carried out using a standardized methodology [11,29], making their comparison difficult. This chapter presents an analysis of the different spectral indicators, following the methodology of Rodrigo et al. (2017) [52]. These indicators are divided into device-independent (APE, BF) and device-dependent (MM, UF/UF^*) indicators. This chapter predominantly focuses on device-independent indicators because they only depend on local spectral characteristics. Their analysis on different time bases (instantaneous, daily, weekly, monthly, and yearly) presumes a relationship with the latitude of the study sites. This document will show the MM_{annual} and UF/UF^*_{annual} calculations for the selected sites to summarize the spectral impact on the six relatives EQEs presented in Chapter 3. This analysis is intended to show general characteristics and trends over time of the mentioned above spectral indicators.

4.1. PV device-independent KPIs

Device-independent spectral indicators are often used to represent the spectral distribution in a scalar manner. The *APE* and the *BF* are the most used indicators for this end. However, this property has been tested under some conditions and for some sites, such as those reported in [73,98]. In particular, the *APE* has shown a direct correlation with the AM [38,99].
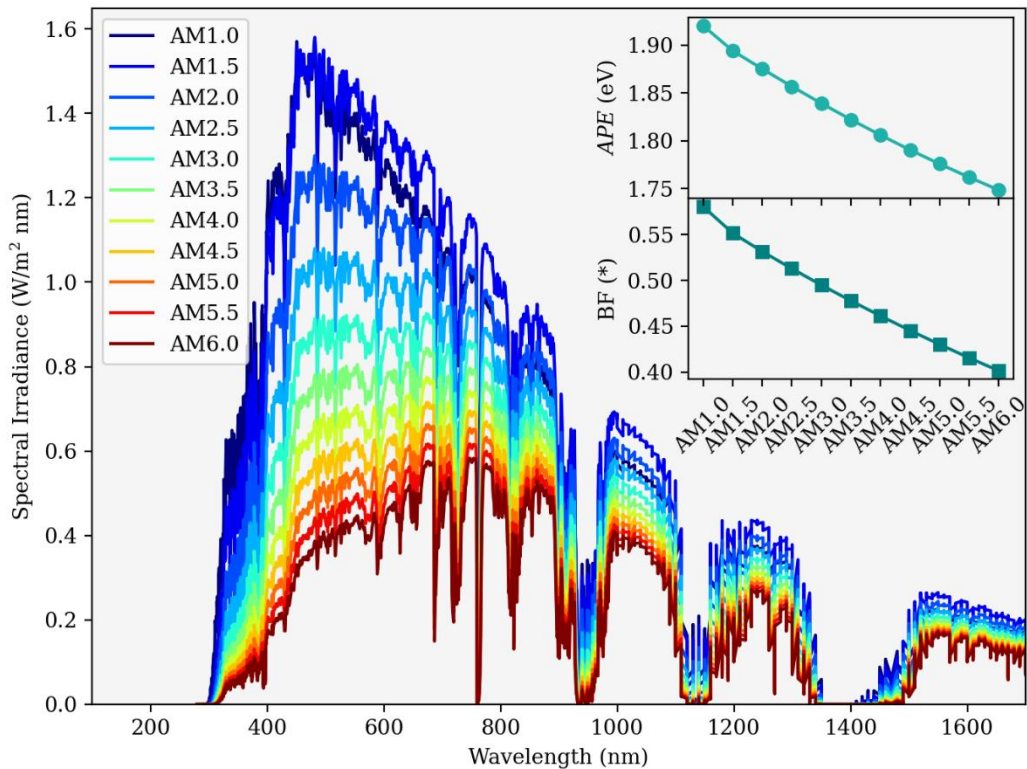
Figure 6. Simulated global spectra using the Simple Model of the Atmospheric Radiative Transfer of Sunshine (SMARTS) for varying AM in central Europe, setting the following parameters: Tilt angle=35°, South-oriented, AOD=0.084, CO_2=370.0ppm, PW (from AM1.5G), O_3 (from AM1.5G). The inset figures show the variation of *APE* and *BF* with AM.

Figure 6 shows a set of spectra simulated using the Simple Model of the Atmospheric Radiative Transfer of Sunshine (SMARTS) [34], varying only the AM and keeping the other inputs constant. SMARTS simulates spectra under clear sky conditions, meaning it only considers atmospheric parameters but not the effects caused by clouds. The inset figures in Figure 6 show the *APE* and the *BF* vs. the AM. Both indicators show a decreasing relationship with the AM.
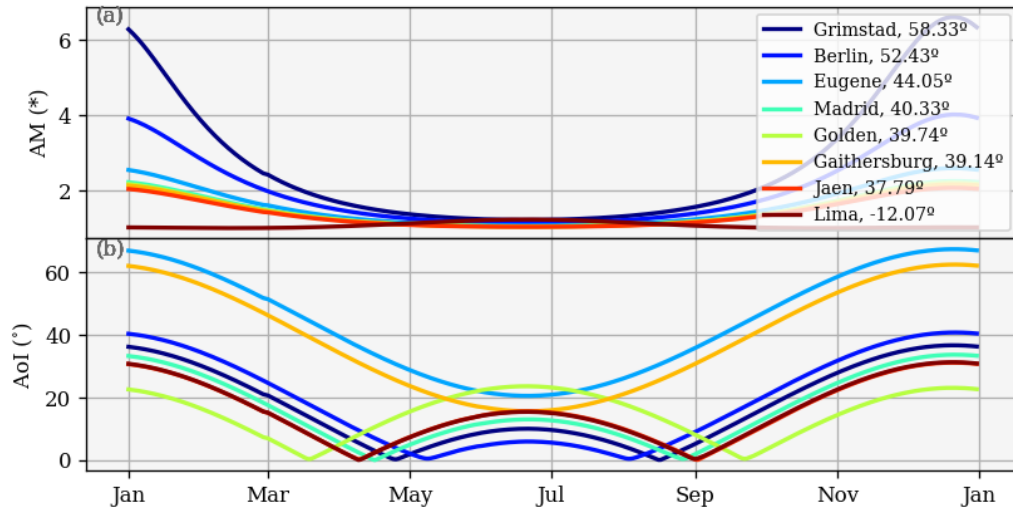
Figure 7. Variation of daily minimum (a) AM and (b) AoI throughout the year, considering the installation conditions of eight locations out of the nine studied (GNI from Albuquerque theoretically points the sun anytime). This graph does not include Albuquerque since it has a theoretically constant 0° AoI.

Additional factors such as clouds, diffuse fraction, and atmospheric constituents influence this general relationship in actual conditions; however, commonly, the AM has a predominant influence on spectral distribution [99,100]. The expression of the AM depends explicitly on the site's latitude, where the spectral distribution is evaluated [89,101]. Figure 7(a) shows the variations of the minimum daily AM throughout the year for the sites for which there are experimental data, except for Albuquerque. Figure 7(b) shows the daily variation of the minimum AoI throughout the year according to the spectroradiometer tilt angle at the selected sites, except for Albuquerque, because DNI ideally holds a zero angle of incidence. The tilt angle influences the global spectrum. In a horizontal position, it usually captures a higher amount of diffuse radiation that tends to shift to short wavelengths. Figure 7(b) shows that Eugene and Gaithersburg have the highest AoI yearly because the spectroradiometer is placed horizontally in these sites. This work, therefore, assumes that their annual spectral distribution would have a blueshift compared to the spectral distribution of the spectroradiometer if it were located at the optimum tilt angle.

4.1.1. Blue Fraction analysis

The BF, as mentioned above, is a PV device-independent spectral indicator, so it aims to quantify red-shift or blue shift of the solar spectrum concerning the reference spectrum, for which BF takes the value of 0.519 (in the range from 350 to 1050 nm, and considering blue radiation below 650nm). Although the APE is the most widespread spectral indicator, recently, Paudyal and Imenes (2021) [73] studied the uniqueness of the BF in Grimstad in Norway to determine the spectral distribution and determined a possible bijectivity with the APE for this site. Given this ability to represent the spectral distribution, some of its behavior is studied throughout the year for different sites worldwide.

Figure 8 shows the behavior of the BF over 12 months on a different time basis (instantaneous, daily-, weekly-, monthly-, and annual-irradiance weighted average) for the sites with GTI. Sites with GHI (Gaithersburg, Eugene) and GNI (Albuquerque) were not considered because it is expected that in these other locations, the diffuse radiation components would be higher or lower, respectively, than what is recorded on a tilted plane at an optimal angle. The $BF_{monthly}$ helps to visualize the seasonal spectral behavior as a function of latitude. Interestingly, it is noted that for the selected sites, such seasonality decreases until it disappears in Lima, for a site close to the equator. Thus, Grimstad presents the greatest spectral seasonality, being blueshifted in the summer months and red-shifted in the winter months, while, on the other hand, in Lima, a spectral blueshift is observed throughout the year. This decreasing seasonality with latitude would exhibit the implicit dependence of AM on latitude. To the right of each time series, its percentage irradiation distribution function throughout the 12 months is presented using the Kernel Density Estimation (KDE). Spectral variability (including seasonality) is reflected in the width of the distribution. From this, it is seen that Lima shows the lowest spectral variability, which would make its monthly variations small. Therefore, the net annual spectral impact on the annual PV performance would be more relevant than the monthly variations.

Figure 8. BF 12-month time series in the instantaneous, daily, weekly, monthly, and annual regime for spectral GTI sorted descendingly by latitude. The associated Irradiation percentage distribution is on the right side according to the BF obtained by the Kernel Density Estimation (KDE) method.

Figure 9 summarizes the percentage irradiation distribution as a function of the BF for the 12 months considered. In this case, this Figure does not consider Albuquerque because its distribution considers spectra close to sunrise and sunset, which are influenced by high AM values. It is noted that the BF_{annual} indicates that in most cases, the spectral distribution throughout the year has a higher fraction

of blue radiation compared to the AM1.5G, except for Grimstad and Golden. Lima is, above all, even the sites with GHI, and has the most acute distribution.

Figure 9. Irradiation percentage distribution in function of the BF (350-1050nm) over 12 months at the nine locations obtained by the Kernel Density Estimation (KDE) method

4.1.2. Average Photon Energy analysis

The APE, on the other hand, is the most widespread PV-device-independent spectral indicator in the literature. Like the BF, the APE seeks to characterize the spectral distribution with a scalar value, qualifying it as red-shift or blueshift depending on its value compared to the value for the AM1.5G spectrum (1.876 eV in the range from 350 to 1050nm).

Figure 10 shows the APE variations over 12 months on different time bases (instantaneous, daily, weekly, monthly, and yearly) and the percentage irradiation distribution for the instantaneous APEs at the right for the sites with GTI. Similar to the BF time series, APE exhibits a decreasing seasonality with latitude, which would manifest the AM variation as shown in Figure 7(a); this means that the AM becomes smaller for the months around July except in Lima, which is in the southern hemisphere. And vice versa for the months around January. A higher AM would correspond to a bluer spectrum due to the longer path length and, thus, more light scattering. While it becomes red-shift for circumstances in which the AM is smaller due to the reduction of the diffuse component and the preponderance of the

direct irradiance component over the global irradiance. It is noted that the APE, as the BF, represents both seasonality and annual nominal values at each selected site.
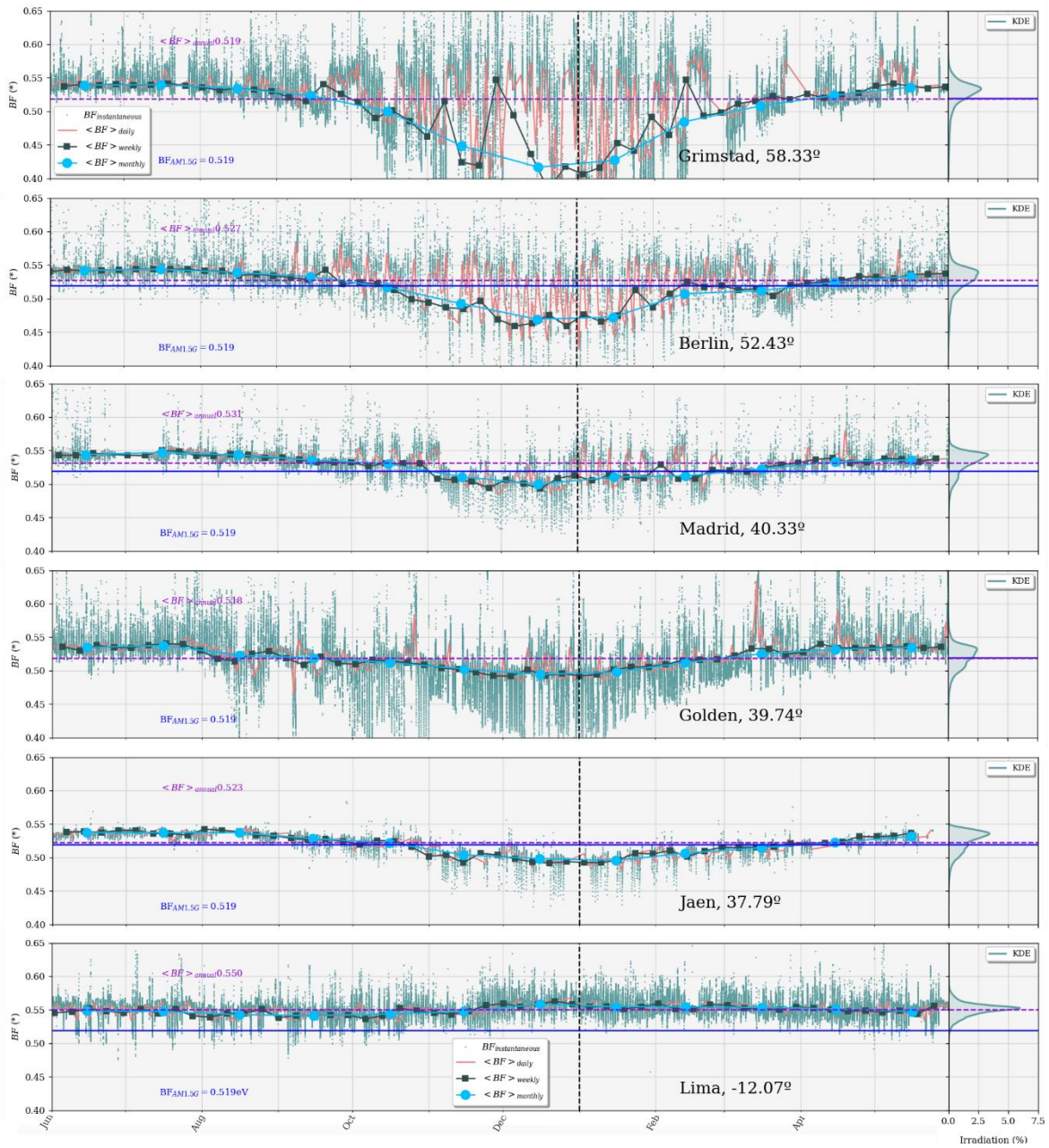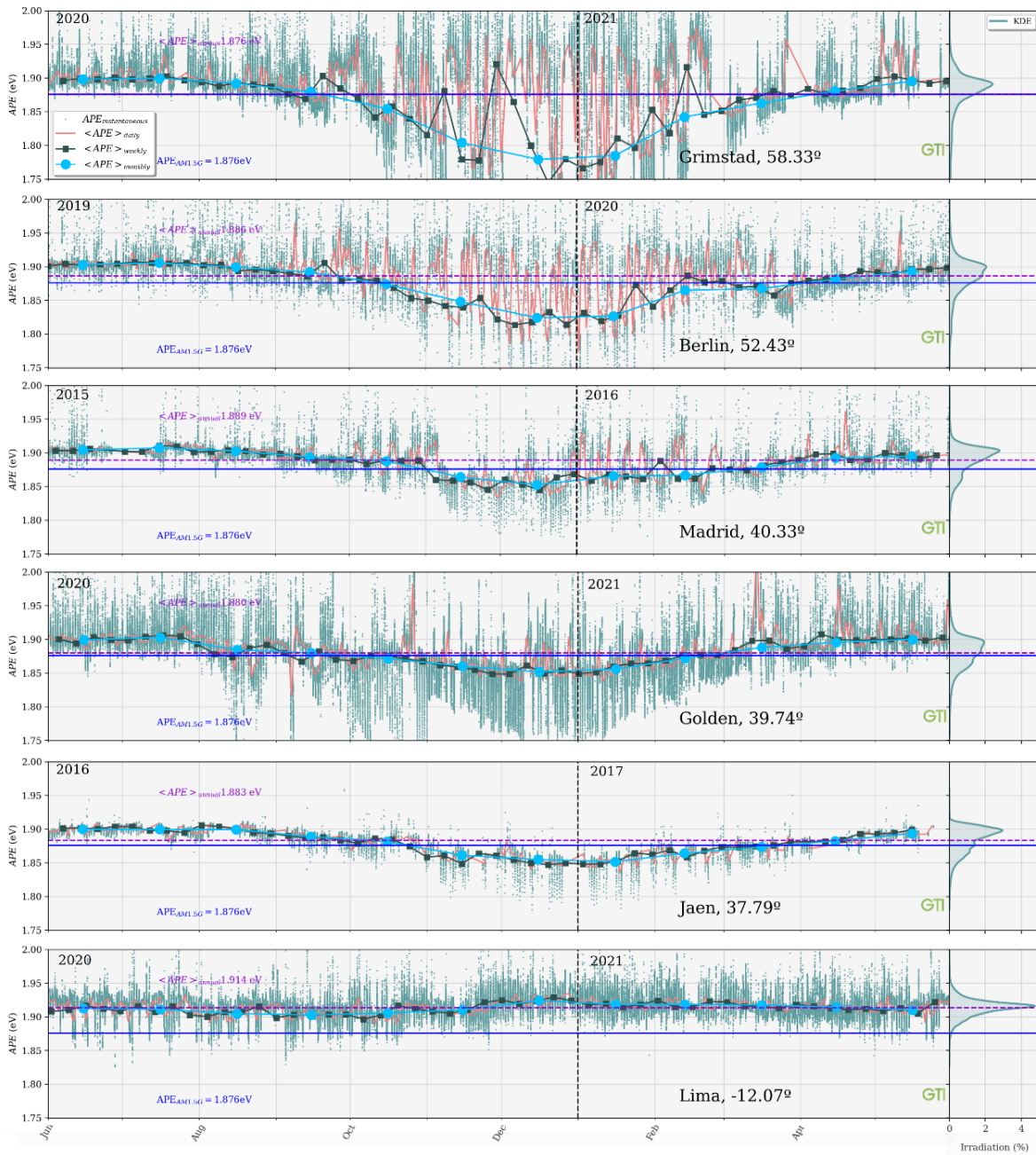

Figure 10. APE 12-month time series in the instantaneous, daily, weekly, monthly, and annual regime for spectral GTI sorted descendingly by latitude. The associated Irradiation percentage distribution is on the right side according to the APE obtained by the Kernel Density Estimation (KDE) method.
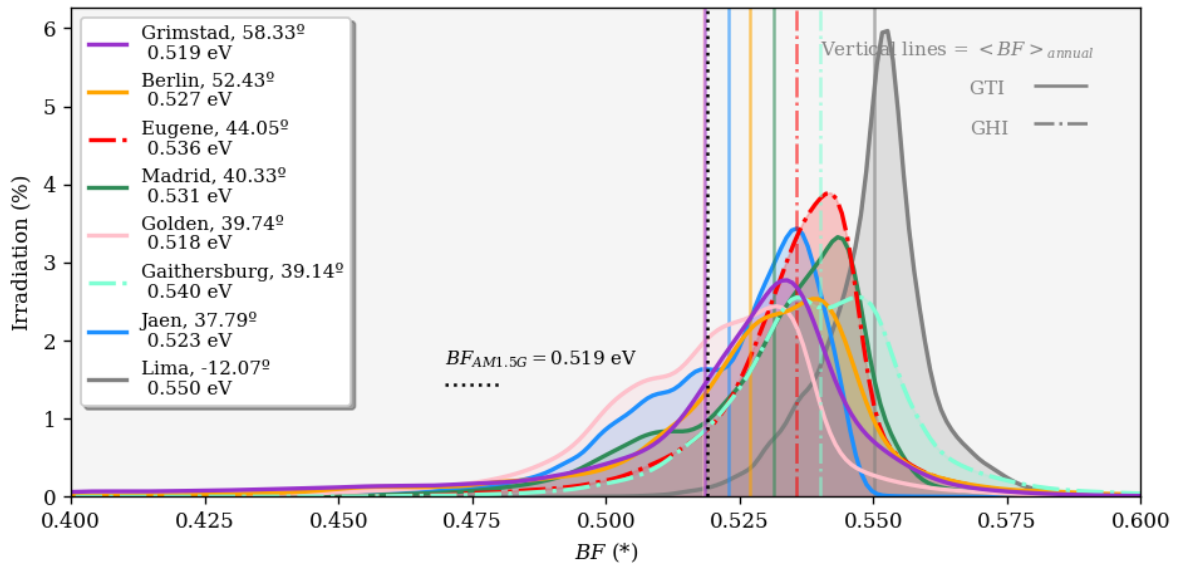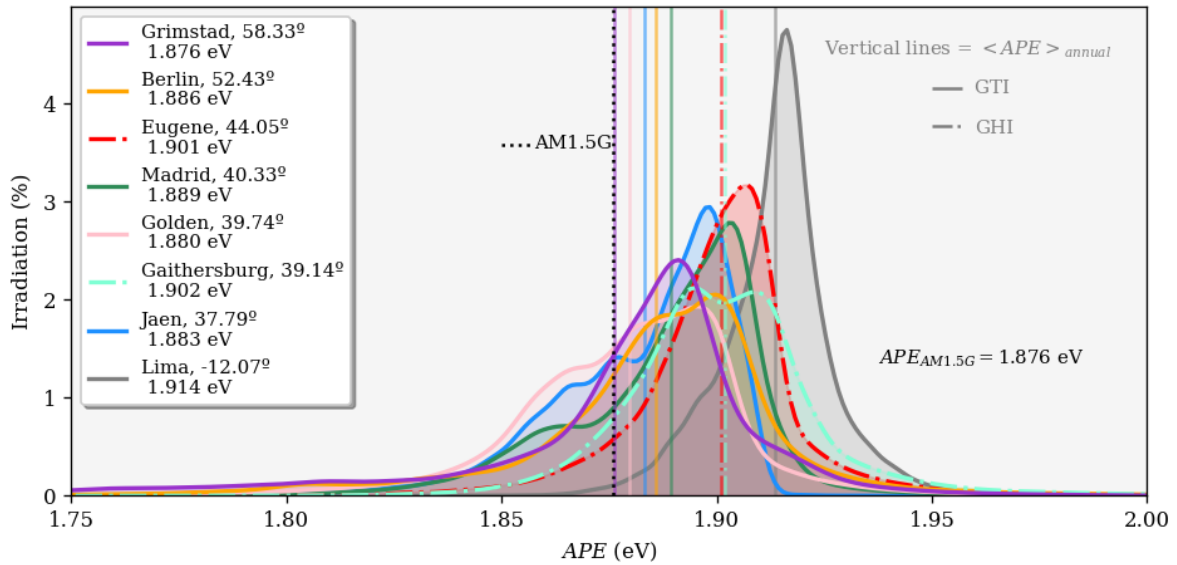
Figure 11. Irradiation percentage distribution in function of the APE (350-1050nm) over 12 months at the nine locations obtained by the Kernel Density Estimation (KDE) method.

The distribution of the annual percentage irradiation distribution as a function of APE is shown in Figure 11. These findings have statistical significance because all spectra cover a broad range of APEs. By Chapter 3, GTI was filtered by the AoI to remove spectra with AoI more than 60°, eliminating the nighttime and early morning hours with red-rich spectra from consideration in this research. Figure 11's distributions exhibit an asymmetry that causes APE distribution skewness deviated from their APE_{annual}. In Gaithersburg, there are two peaks, one below and another above the APE_{annual}, related to the two remarked APE seasonal trends. The seasonal changes of APE at each location account for the varying degrees of skewness in the distributions, as discussed in Figure 10.

It should be noted that when comparing Figure 11 with Figure 9, the mean annual values do not have the same relative difference between the selected sites. For instance, APE_{annual} in Golden exhibits a spectral distribution above $APE_{AM1.5G}$, while its corresponding BF_{annual} is below $BF_{AM1.5G}$. This is very interesting as it shows a clear difference when representing the spectral distribution at a site. Therefore, these results suggest that these indicators are not interchangeable, and a comparison of the spectral distribution should be made without mixing these indicators, as they physically have different meanings. An interrelation between these indicators would allow an exchange between them only under a bounded uncertainty.

4.1.3 Annual *APE* for different latitudes

Figure 12 shows the relationship between the APE_{annual} and the latitude of the site where it was measured. The dashed linear regression line in Figure 12 shows a general trend for APE_{annual}, with decreasing values as the distance from the equator rises. APE_{annual} values from [28] and [31], for three additional sites in Japan and two in Brazil, respectively, are included to widen the range of sites further. Gaithersburg and Eugene, two mid-latitude sites with recorded spectral GHI, may have slightly higher values of APE_{annual} or spectra that have been shifted to shorter wavelengths. In fact, spectroradiometers outside the tropics in a horizontal orientation measure more blue light during the main daytime hours than if tilted to collect the most annual irradiation. The Albuquerque sun-tracked spectroradiometer, on the other hand, observes less blue sky because GNI has a higher red-light component than GTI. The spectral distribution variability changes depending on the location due to other particular climatic factors not being studied here, such as cloud cover, aerosols, humidity, CO_2, ozone, and the surrounding albedo [34]. For instance, Kusatsu has the highest, GTI-related APE_{annual}, surpassing the APE_{annual} of the GHI spectra at the other Japanese sites. Kusatsu is cited in numerous studies as having a notably blue-rich spectral distribution [102–104]. This may result from the weather being mainly cloudy [102]. In this location, it appears that this factor surpasses the impact of AM (and hence, the latitude).
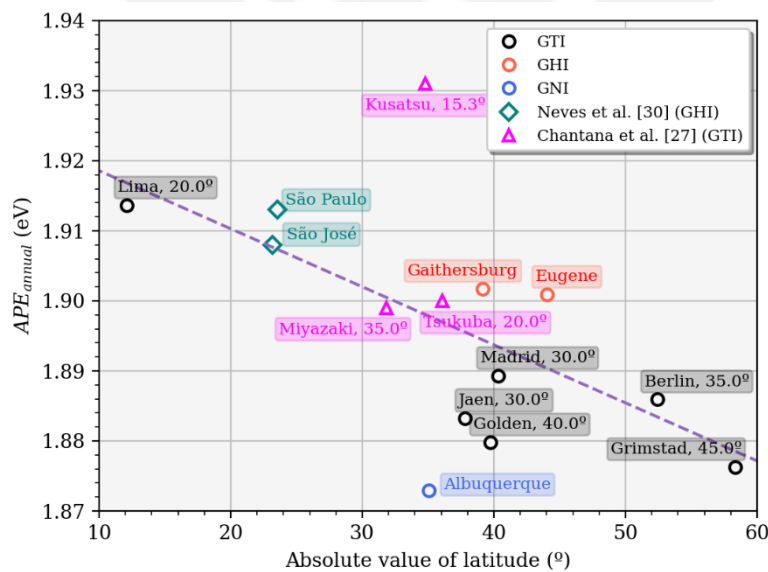
Figure 12. APE_{annual} as a function of the absolute value of location latitude. I added additional points for São Paulo and São José from Neves et al. (2021) [30] and Miyazaki, Kusatsu, and Tsukuba from Chantana et al. (2020) [27]. For GTI data, the spectrometer tilt angle is indicated at each location.

4.2. PV device-dependent KPIs

4.2.1. Annual Integrated Useful Fraction Ratio

The UF/UF^* is based on the UF indicator, as described in Chapter 3, which has been used in the literature to indicate the spectral gains or losses with only the bandgap information, avoiding the need to know the spectral response of the PV device [77]. However, its ability to represent the spectral impact on PV performance has limitations depending on the PV technology. A further physical interpretation states that the UF may represent the influence of the solar irradiance spectrum useful fraction on the ability to generate an electric current of a PV module [105].
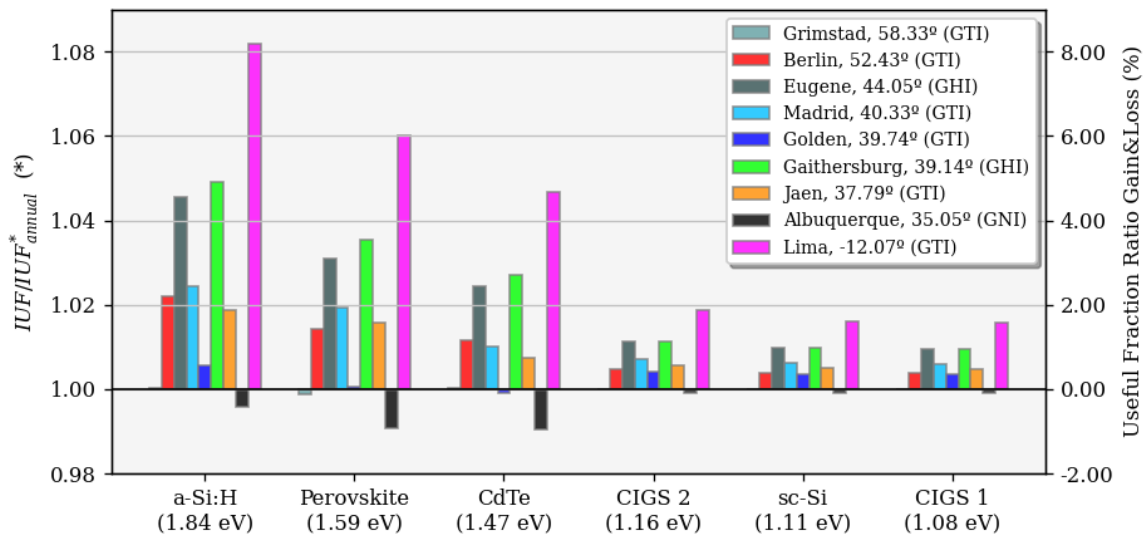
Figure 13. IUF/IUF^*_{annual}'s bar chart of our nine locations for each PV technology. The bars also indicate the Useful Fraction Ratio gains&losses.

Figure 13 shows the IUF/IUF^*_{annual} and the Useful Fraction Ratio Gains&Loss 100%(1-IUF/IUF^*_{annual}). The latter can be interpreted as the annual gains or losses of the useful irradiance to the useful AM1.5G irradiance according to the bandgap of each PV technology. The results indicate that useful irradiance losses occur in all cases for Albuquerque. At the same time, Grimstad exhibits tiny variations around 0%, which suggests that its annual behavior in terms of UF is very similar to AM1.5G for all PV technologies. In contrast, Lima exhibits the highest gains for a-Si, above 8%.

4.2.2. Annual Spectral Mismatch Factor
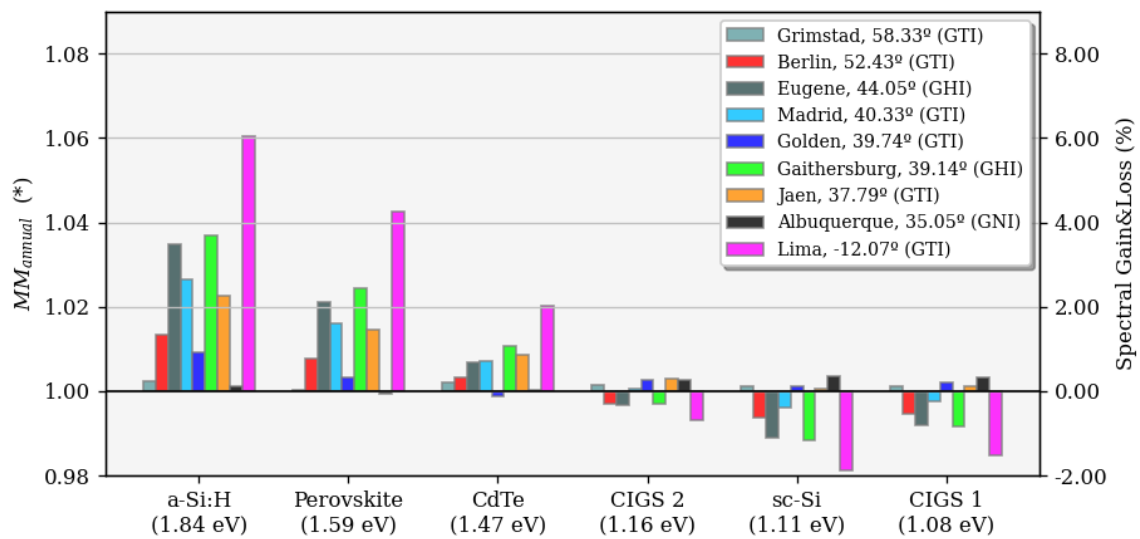
Figure 14. MM_{annual}'s bar chart of our nine locations for each PV technology. The bars also indicate spectral gains or losses.

Figure 14 shows the nominal gains and losses ($spectral\ Gain\&Loss$ defined as $100\% * (MM - 1)$) along with the annual MM for the six chosen PV technologies. In four locations—Lima, Gaithersburg, Eugene, and Madrid—some observed spectral gain and loss trends for the aforementioned devices are significantly confirmed. In Lima, the most significant spectral gains and losses for all PV technologies were observed. The maximum APE_{annual} is also found here, and there is hardly any spectral seasonality. The solar spectrum is also highly blue throughout the year. However, further examination of the result in Figure 14 reveals that the site's latitude alone is insufficient to predict spectral effects and can only provide a rough path.

4.3. Conclusions

Spectral indicators were separated into two groups following the Rodrigo et al (2017) methodology [52]. Those that depend on the PV device information, such as EQE or SR (e.g., MM and UF/UF^*) and independent (e.g., APE, BF). The former aims to characterize the spectral impact on PV performance, while the latter describes the spectral distribution in a scalar manner. This chapter emphasized describing the behavior of APE and BF during 12 months worldwide. Both indicators represented the

seasonal behavior of the spectral distribution in the sites with GTI (Grimstad, Berlin, Madrid, Golden, Jaen, and Lima) by weighting them by irradiance. For example, it was verified using spectra simulated by SMARTS that AM influences the spectral distribution as expected from previous studies. The implicit dependence of the AM on latitude would explain the spectral seasonality observed in the localities with GTI. This work also shows that the BF_{annual} and APE_{annual} exhibit different trends. Golden, for instance, presents an BF_{annual} below $BF_{AM1.5G}$ and an APE_{annual} above $APE_{AM1.5G}$, indicating that these indicators, although they identify the spectral distribution, they do so in a different way due to their different definition and physical meaning. Although the APE_{annual} shows a decreasing trend with the distance of a site from the equator (absolute value of latitude), such a rule of thumb ceases to be true when other site climatic conditions, such as a high diffuse fraction, are significant and superimpose the effects of AM. Finally, this chapter showed the MM_{annual} and IUF/IUF^{*}_{annual} for the nine sites. These results show that the IUF/IUF^{*}_{annual} differs in how much it predicts the spectral gains and losses compared to the MM_{annual}. However, Lima showed the strongest annual spectral gains and losses in PV performance. Grimstad behaved oppositely, having the minimum annual spectral gains and losses.

Part of these results have been published in [106].

5. Interrelationships between energetic PV spectral indicators

5.1. Introduction

Various methods that estimate the spectral impact on PV performance, such as CREST, First Solar, and Sandia, are commonly based on atmospheric parameters such as AM, Precipitable Water, and Clearness index. These methods also typically use empirical formulas directly relating them to the spectral impact [35,36,40,107–111]. However, the spectral distribution, independent of the PV device, is already complexly dependent on the parameters above, as demonstrated by physical models based on the Radiative Transfer Theory [34,51,112].

The previous chapter studied the behavior of the spectral indicators (PV-device-dependent and -independent) throughout 12 months for the selected sites. In addition, that chapter emphasized the PV-device-independent spectral indicators, primarily the APE. The APE showed a site-dependent seasonal trend due to being influenced by the AM, which implicity depends on latitude. However, the particular atmospheric conditions of the site may cause such a trend to no longer be preserved. In this way, the solar spectrum has a complex dependence on such parameters, and predicting the APE from only atmospheric parameters is a strenuous task. For this reason, this chapter references the PV-device-independent indicators and seeks to find correlations with their corresponding PV-device-dependent indicators for different climates and latitudes. Previously linear correlations, such as $APE_{monthly}$ vs. $MM_{monthly}$ have been reported locally [11,30]. Other studies, as mentioned above, tried to correlate these indicators on an instantaneous basis, which reported a polynomial relationship [54] in Kusatsu, while Dirrnberger et al. (2015) [11] showed that on an instantaneous basis, these two indicators in Freiburg exhibited a non-bijective relationship.

In this way, this chapter first tries to find global correlations between these indicators using experimental spectral data from nine sites worldwide. Thus, this chapter shows the interrelations UF/UF^* vs. BF, UF/UF^* vs. APE, MM vs. BF, and MM vs. APE, in different time basis (instantaneous, daily, and monthly) and globally.

5.2. Detection of interrelationships between different spectral indicators
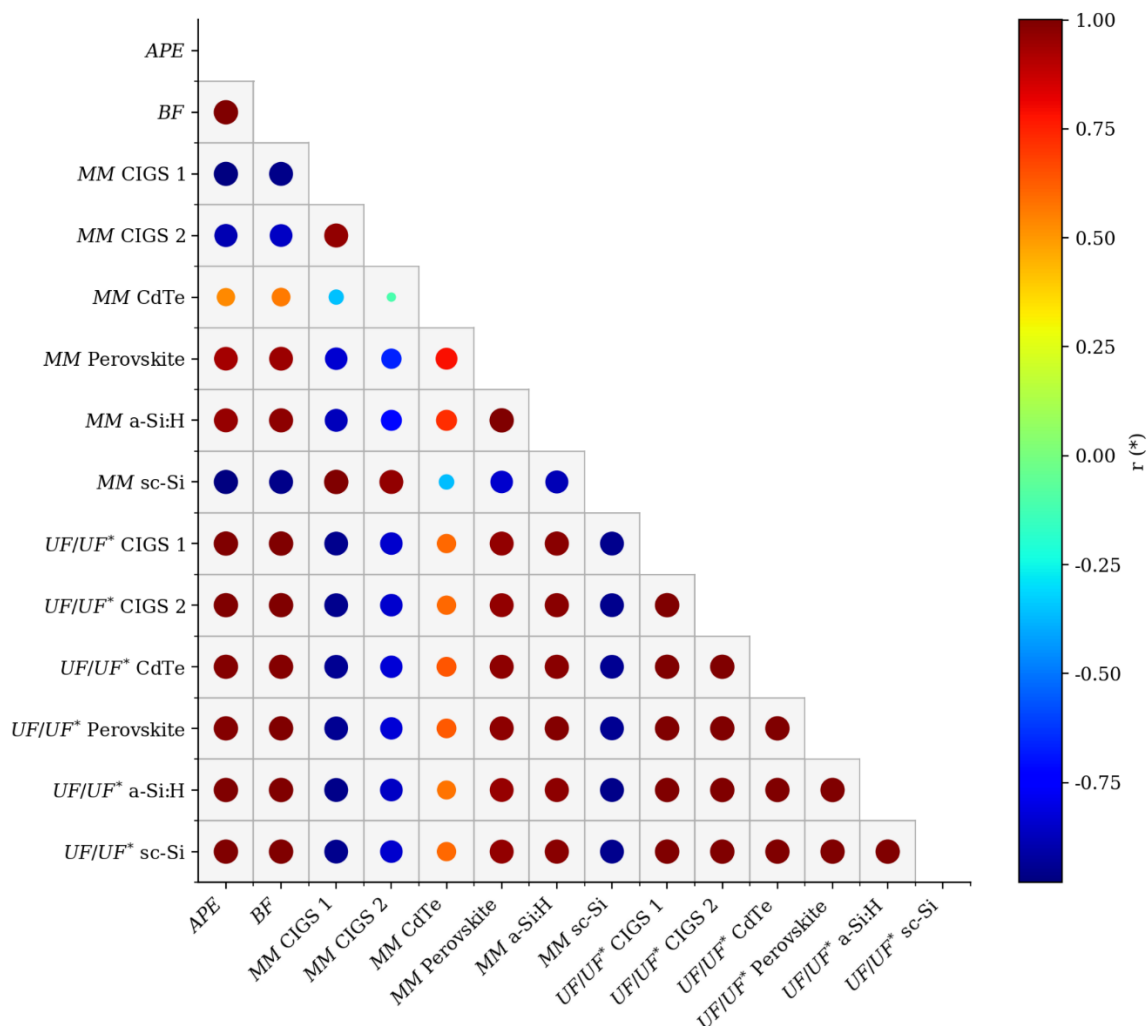
Figure 15. Correlation matrix between different PV device-independent (APE, BF) and -dependent (MM and UF/UF^*) spectral indicators for six PV technologies: CIGS 1, CIGS 2, CdTe, Perovskite, a-Si:H and sc-Si using spectral dataset from Berlin.

To determine the interrelationships between the different spectral indicators, it is essential to visualize their relationship. For example, Figure 15 shows the correlation matrix between the various instantaneous spectral indicators studied in this work for Berlin. As expected, it is noted that the APE and BF present a high positive correlation. The correlation remains high for other indicators, such as MM (although it depends on the PV technology, with CdTe showing the lowest correlation) and UF/UF^*. In addition, the BF presents a similar correlation with the other PV-dependent spectral indicators, making it very attractive to represent the spectral distribution and find an empirical dependence with another PV-dependent spectral indicator.

5.3. Identification of the "Lobster claws" in instantaneous APE vs. MM in Berlin

The relationship between *APE* and *MM* has previously been reported locally. Such a relationship is essential to identify the *MM*, i.e., the Spectral Impact, based on which is a PV-Independent Spectral indicator and only requires as input the measured solar spectrum.

Figure 16 shows the relationship between instantaneous values of *MM* and *APE* in Berlin, where the solid line indicates the total linear regression. The results show two *MM* branches for high *APE*s for most PV Technologies like a "Lobster Claws" shape. This keeps concordance with what was evidenced by Dirnberger et al. (2015) [11]; in their work, they presented the relationship between the instantaneous *MM* and *APE* in Freiburg (Germany) for spectra measured between 300 and 1700 nm and concluded that in a instantaneous time basis, *MM* and *APE* scatter plot exhibited two branches, as this work reports for Berlin for the *APE* in the range between 350 and 1050 nm and *MM* between 280 and 4000 nm.
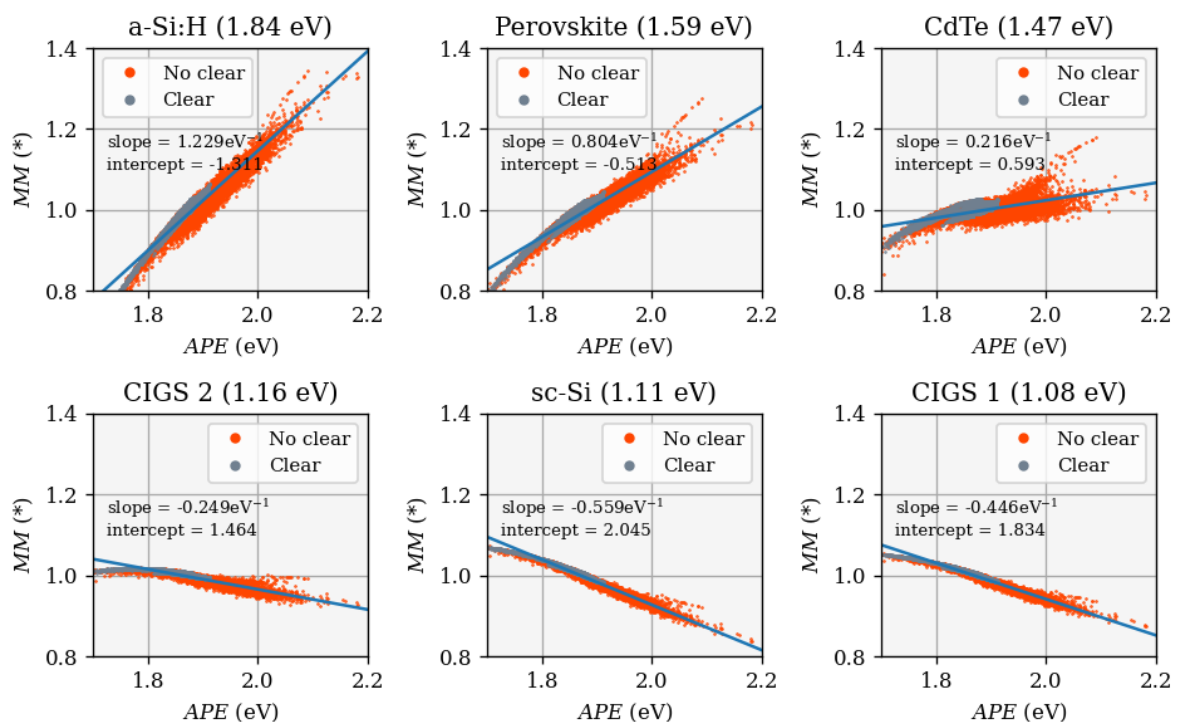
Figure 16. *MM* vs. *APE* scatter plot showing the lobster claws belonging to cloudy sky conditions. The line represents the total linear regression. Bandgaps are indicated in parentheses, along with their respective technology.

Figure 16 shows the instantaneous *MM* vs. *APE* relationship under two sky conditions: 1. under clear sky, identified according to the Reno and Hansen algorithm (2016) and not-clear skies, those not identified with the algorithm above. Under clear skies, the relationship *APE* vs. *MM* tends to be injective, i.e., specific *MM* could correspond to a unique *APE* value in a good approximation. However, the "Lobster Claws" are evident under not clear skies.
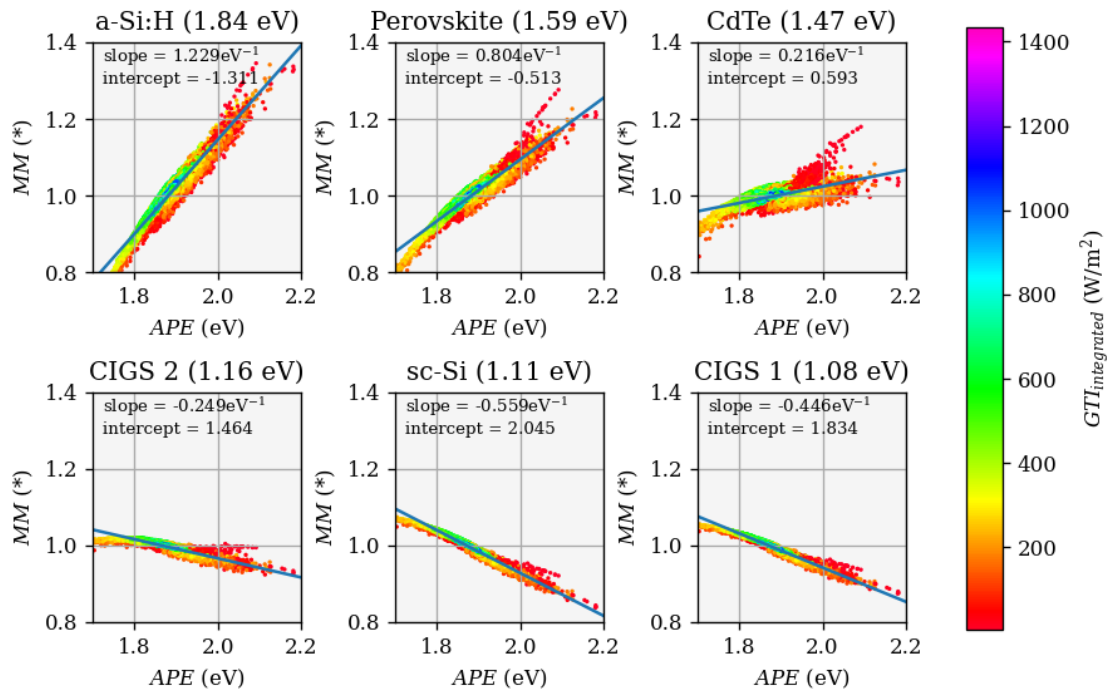
Figure 17. Instantaneous *MM* vs. *APE* scatter plot in Berlin. The integrated irradiances of these extrapolated spectra are shown in color.

Figure 17 shows the same relationship as in Figure 16, the scatter plot between *MM* and *APE* for Berlin, but in color, indicating the extrapolated spectrum's integrated irradiance. It is evident that the "Lobster Claws" appear for high *APE*s and low irradiances, most noticeable below 200 W/m^2. Since spectral measurements with an AOI above 60 ° were discarded, this spectral data set does not consider spectral data from the early mornings or late afternoons. Therefore, the spectral measurements at low irradiances and high *APE* could correspond to cloudy sky conditions. Because under an overcast sky, direct irradiance is practically annulled, and the spectroradiometer mainly captures the diffuse spectral distribution that is generally blueshifted.
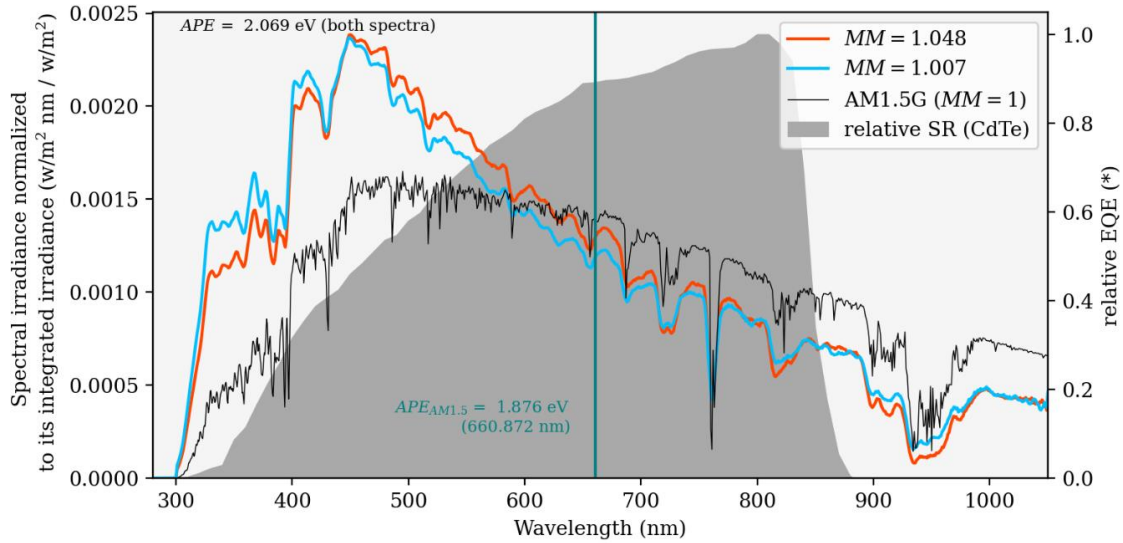
Figure 18. Two exemplary spectra from Berlin with similar *APE* normalized to their integrated irradiance and the AM1.5G spectrum. Shading represents the relative SR for CdTe described in Figure 4. The solid green line represents the $APE_{AM1.5G}$ in terms of wavelength (nm).

Figure 18 shows two normalized exemplary spectra of similar *APE* corresponding to *MM* in different "claws" for CdTe. These measured spectra present a high *APE* (blue-shifted). This correlates with the measured spectra significantly exceeding the AM1.5G spectrum in intensities below the referential green line. However, despite having the same *APE*, both spectra differ in *MM*. It is observed that the spectrum of higher *MM* has higher intensities along the wavelengths in the regions where the SR of CdTe is higher (visible range), which would corroborate such a discrepancy in *MM*. This is evidenced despite the high short wavelength intensities for the spectrum with smaller *MM*. In these two particular situations, the spectra variations in the ultraviolet and visible region could be explained by the variations of incoming scattered irradiance in the global measured spectrum due to the presence of clouds, keeping in line with the abovementioned hypothesis.
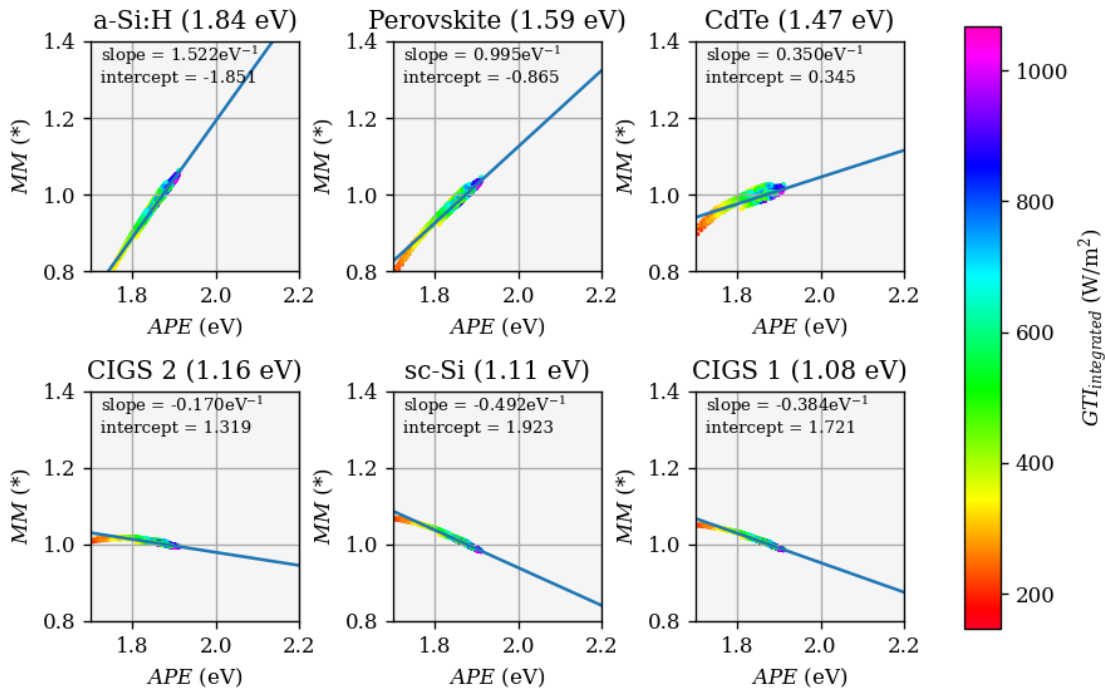
Figure 19. Instantaneous *MM* and *APE* scatter plot in Berlin for clear sky conditions. The integrated irradiances of these extrapolated spectra are shown in color.

Figure 19 shows the relationship above (Figure 17) under clear skies. Thus, the linear regression corresponds to these values under clear skies. It can be noted that the *APE*s are markedly separated by increasing irradiance levels. For example, the lowest *APE*s are remarkably related to low irradiances and vice versa. This would reflect the seasonal behavior described in Figure 10. The spectral distribution in Berlin tends to be bluer for the summer months, in which the irradiance levels are higher because the AM is lower. Otherwise, the spectral irradiance exhibits low integrated irradiances for winter months and less blue spectra.
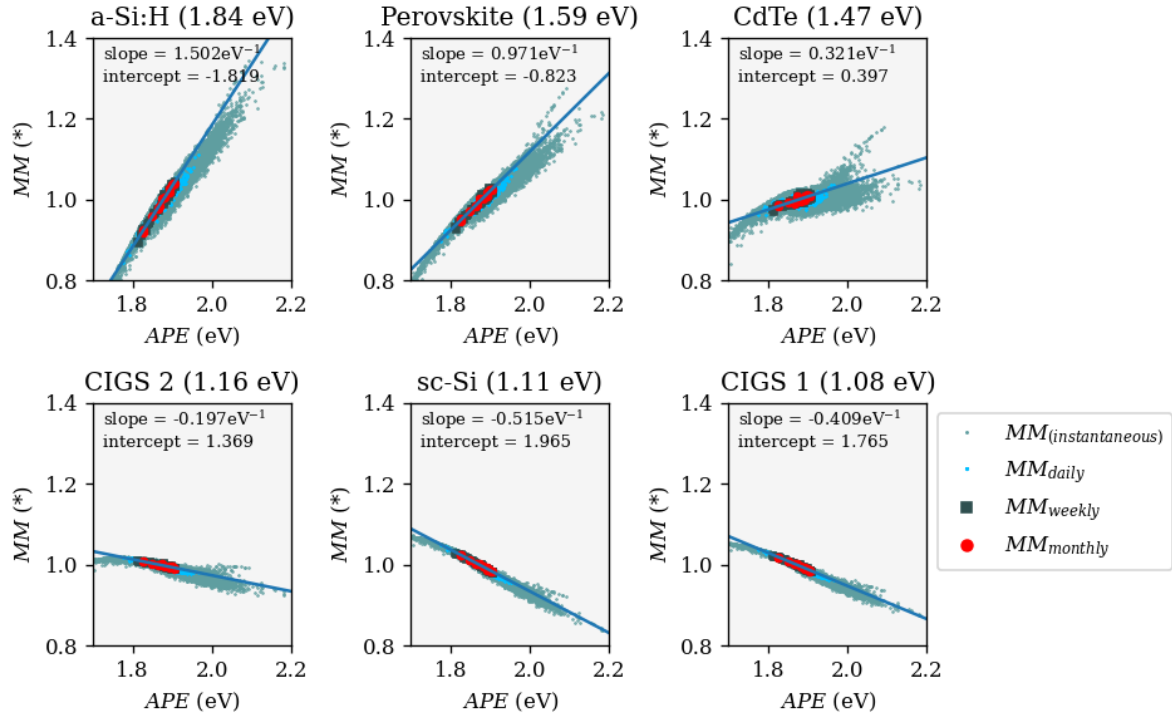
Figure 20. *MM* vs. *APE* scatter plot on different time scales: instantaneous, weighted daily, weighted weekly, and weighted monthly in Berlin. The blue line represents the linear regression of the monthly weighted values.

Figure 20 summarizes the *APE* vs. *MM* relationship for different time scales (instantaneous, daily, weekly, and monthly) in Berlin. The straight line, in this case, represents the linear regression for $APE_{monthly}$ vs. $MM_{monthly}$. It is noted that as the time scale increases, the linearity of the regressions increases. Furthermore, it can be seen that the slopes obtained in this case are similar to the slopes obtained in Figure 19 (based on instantaneous indicators and under clear skies). These results suggest that weighting the spectral indicators by irradiance would increase the significance of conditions under clear skies since these are usually endowed with higher irradiances. This makes it convenient to study the interrelationships between the PV-device-dependent and -independent indicators monthly since weighting by irradiance would be expected to help linearity.

5.4. Global interrelationships for the IUF/IUF^*

Figure 21. Linear relationship between $IUF/IUF^*_{monthly}$ and $BF_{monthly}$ at nine world-wide locations for six different PV technologies: (a) a-Si: H, (B) Perovskite, (c) CdTe, (d) CIGS 2, (e) sc-Si and (f) CIGS 1. RSE and r are the residual standard error and the correlation coefficient, respectively

Figure 21 depicts the correlation between the $IUF/IUF^*_{monthly}$ and $BF_{monthly}$ values for the nine sites and various PV technologies. The 95% prediction interval is also shown graphically as dashed lines. They anticipate a new observation will fall between the lines with a 95% probability. The residual standard error (RSE) is indicated. The linear regressions for all technologies show an excellent correlation ($r \geq 0.99$) between the two indicators.

The following three hypotheses may back up such a linear relationship:

1. The mathematical equations for UF/UF^* and BF, as stated in Chapter 3, are proportionate as indefinite integrals.

2. The Martin and Ruiz (1999) [31] extrapolation approach assumes that the irradiance in the band above 1100 nm is proportional to the irradiance between 700 and 1100 nm. As the integrated

irradiance from 1050 to 1700 nm of the extrapolated spectrum by the Martin and Ruiz approach is comparable to the observed irradiance in the same range, Figure 3 demonstrates that the latter assumption is valid in the region from 700 to 1050 nm. As a result, the spectral irradiance in various spectral bands may be proportionate. Given their integration limits, the UF/UF^* with the BF may exhibit such a proportionality, particularly for spectra taken under clear sky conditions. As a result, selecting integration limits would not alter the two spectral indicators' linear relationship.

3. The spectra recorded at higher irradiance are given more weight when calculating the weighted average spectral indicators. As a result, indicators such as UF/UF^* and BF receive more significant contributions from spectral measurements made under clear sky conditions. This prevents the linear trend from branching, which can occasionally be seen for instantaneous values across similar indicators, such as MM with APE, as shown in [11].

While spectra changes are anticipated in the high energy region, the RSE of the linear regressions for narrow bandgap technology is 3–4 times lower than that of solar cells with wide bandgap.
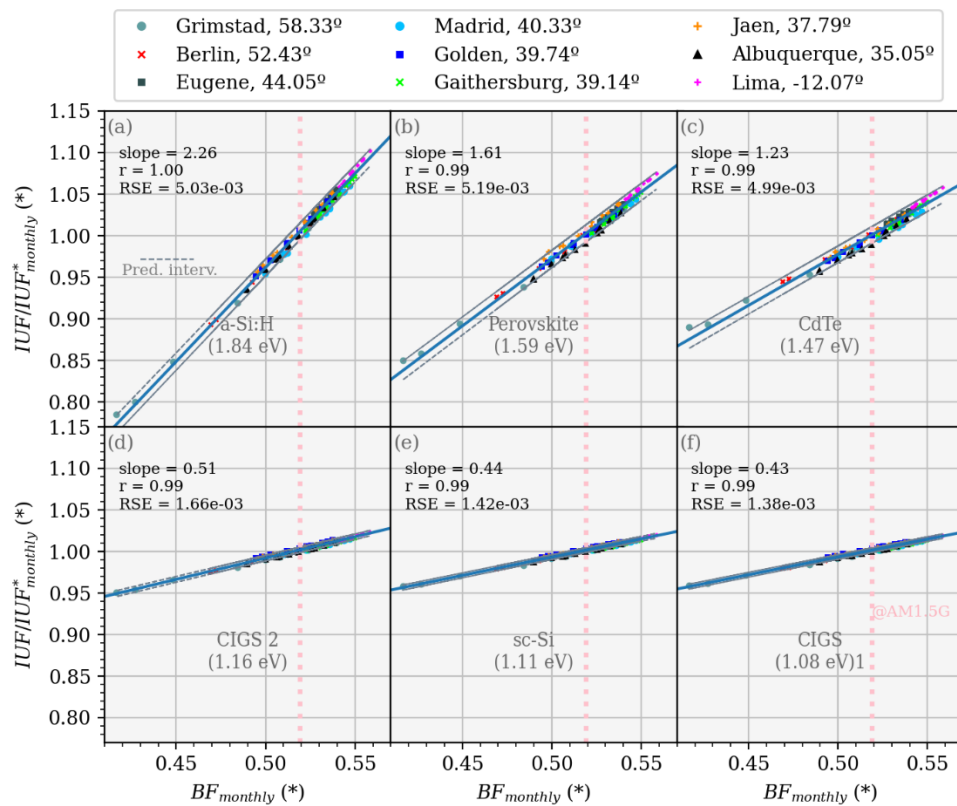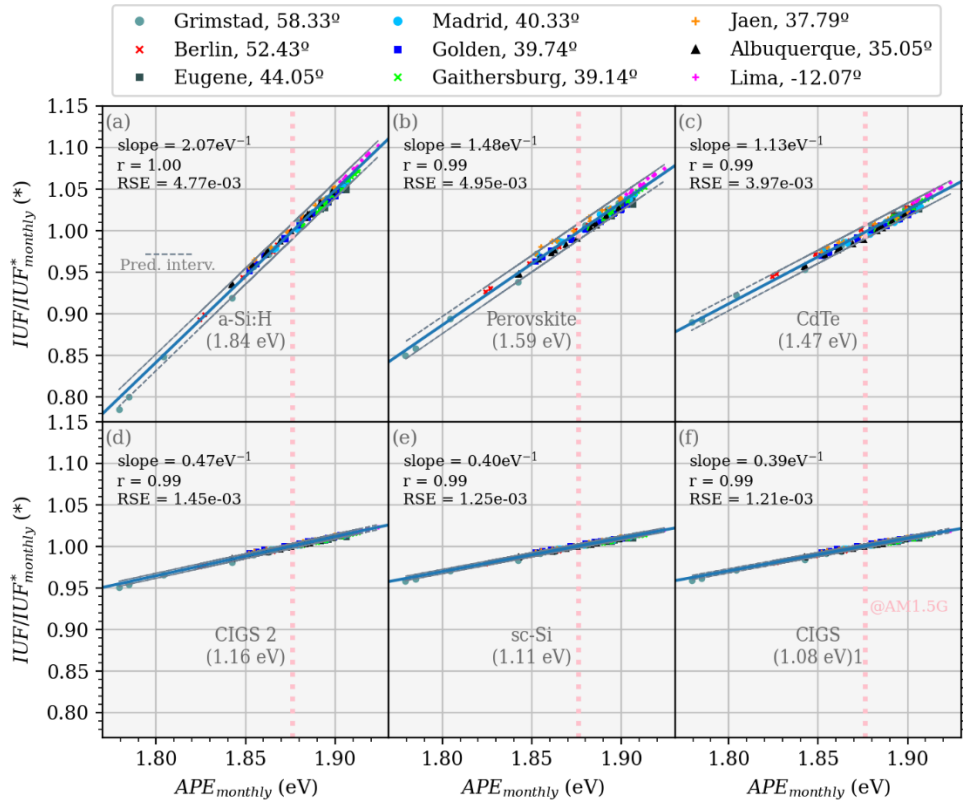
Figure 22. Linear relationship between $IUF/IUF^*_{monthly}$ and $APE_{monthly}$ at nine world-wide locations for six different PV technologies: (a) a-Si: H, (B) Perovskite, (c) CdTe, (d) CIGS 2, (e) sc-Si, (f) CIGS 1. RSE and r are the residual standard error and the correlation coefficient, respectively

Figure 22 illustrates the global linear interrelationship between the $IUF/IUF^*_{monthly}$ and the $APE_{monthly}$. It is interesting to note that the linear regression between these two energetic spectral indicators has RSEs that are even lower than those found when comparing $IUF/IUF^*_{monthly}$ vs. $BF_{monthly}$. Since that $APE_{monthly}$ is one of the indicators that is given more frequently to characterize spectral distributions, this linearity may make it convenient to predict $IUF/IUF^*_{monthly}$. However, the linear relationship is still well supported (r ≥ 0.98), even when daily integration is used instead of monthly integration, as shown in Figure 23.
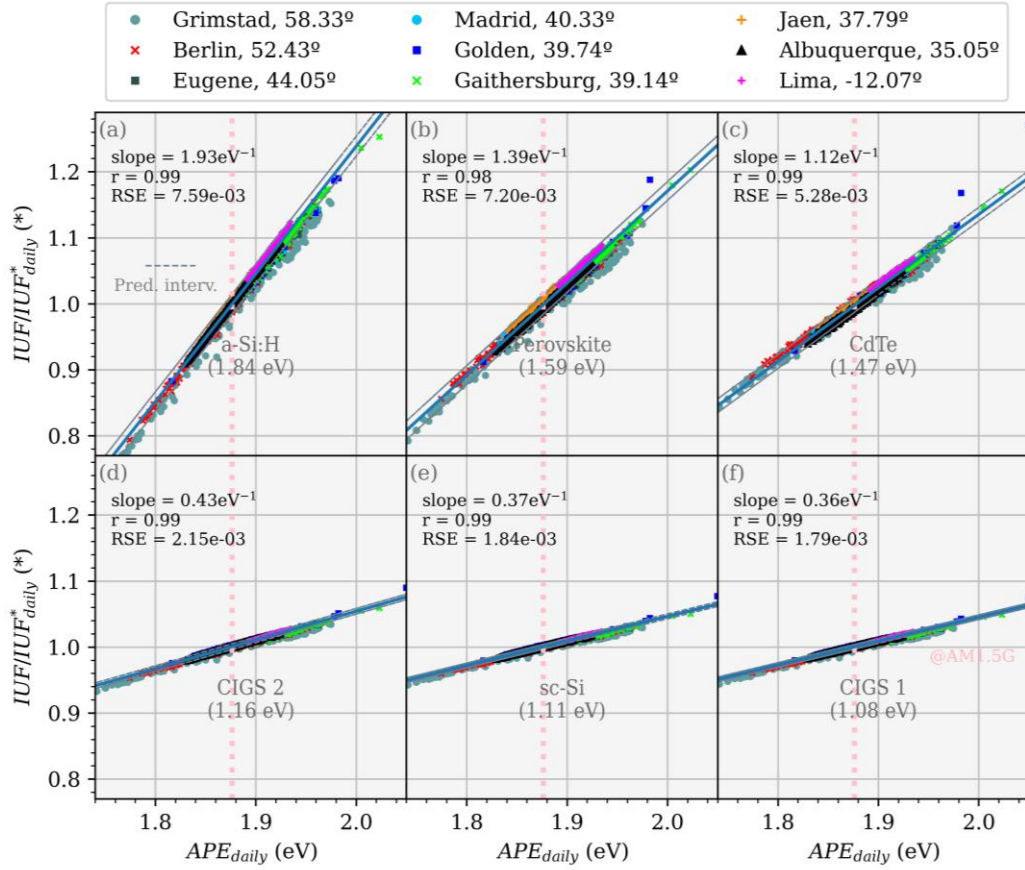
Figure 23. Linear relationship between IUF/IUF^*_{daily} and APE_{daily} at nine world-wide locations for six different PV technologies: (a) a-Si: H, (b) Perovskite, (c) CdTe, (d) CIGS 2, (e) sc-Si and (f) CIGS 1. The gray dashed lines indicate the prediction interval. The vertical dotted line APE for the AM1.5G spectrum indicates. RSE and r are the residual standard error and the correlation coefficient, respectively.

5.5. Global interrelationships for the MM

5.5.1. Theoretical examination of the relationship MM vs. APE

Due to its intuitive interpretation, the *MM* is one of the most often used spectral indicators to represent the spectral impact on PV performance. However, uncertainties may be introduced due to its sensitivity to many conditions. One critical point, for instance, is the limited spectral range. Thus, this work uses the spectral range between 280 to 4000 nm through the extrapolations methods described in Chapter 3.
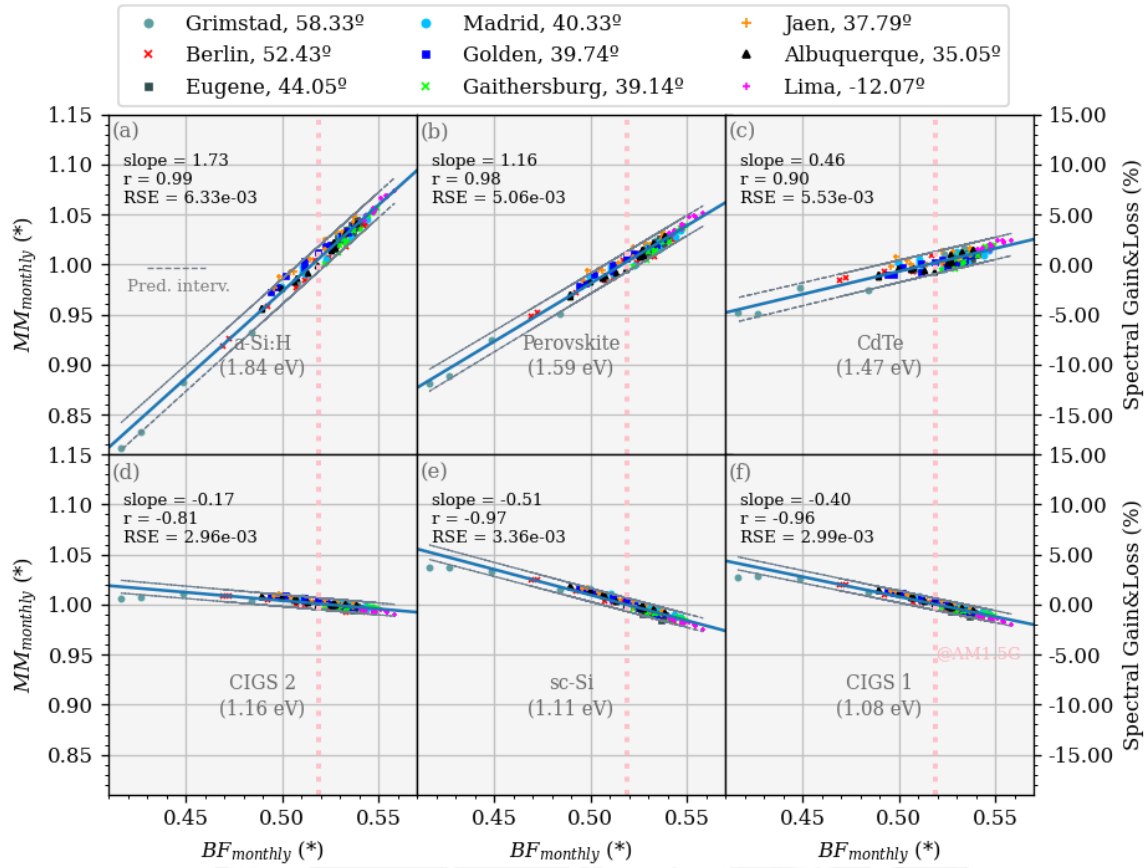
Figure 24. Linear relationship between $MM_{monthly}$ (and spectral gains/losses) and $BF_{monthly}$ for six different PV technologies: (a) a-Si: H, (B) Perovskite, (c) CdTe, (d) CIGS 2, (e) sc-Si and (f) CIGS 1.

As described in section 4.1, the BF can represent the spectral distribution in a scalar way. In addition, the previous chapter remarked that the BF and APE have different physical interpretations and that their values are not interchangeable. Thus, it is interesting to examine the correlation between the $BF_{monthly}$ and the $MM_{monthly}$, as shown in Figure 24. It should be noted that the $BF_{monthly}$ and the $MM_{monthly}$ exhibit a linear relationship despite also presenting the "Lobster claws" shapes (not shown here); this makes the $BF_{monthly}$ a suitable indicator for predicting the monthly spectral impact ($MM_{monthly}$).
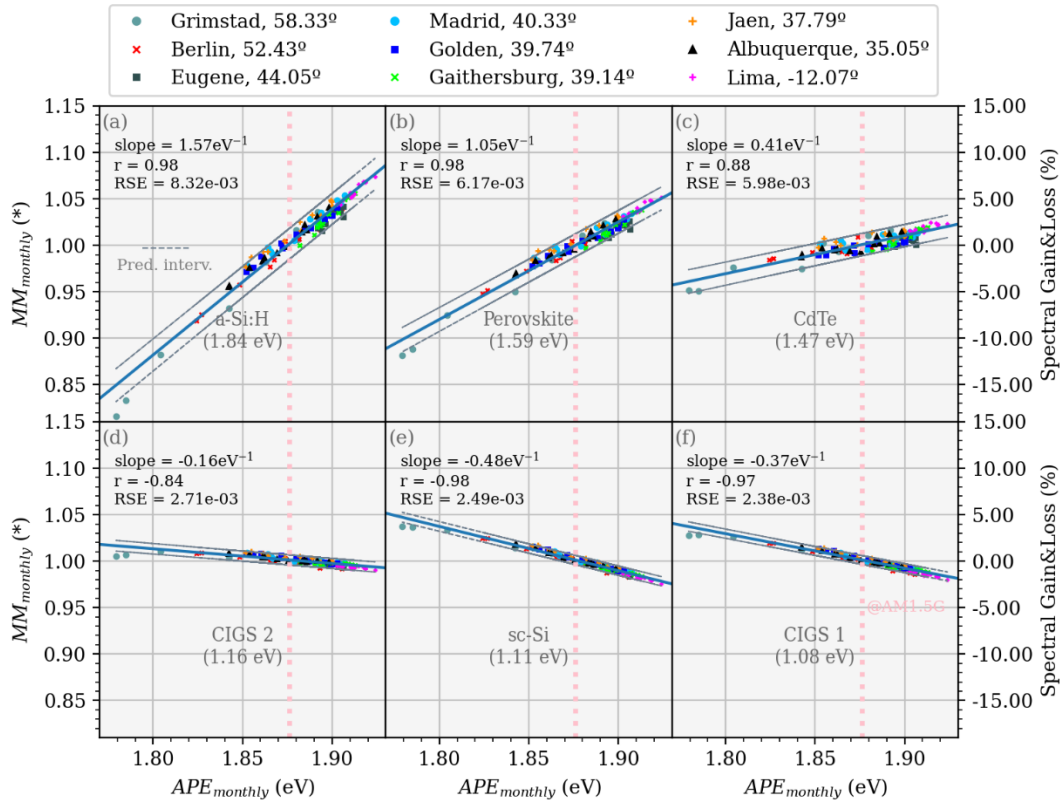
Figure 25. Linear relationship between $MM_{monthly}$ (and spectral gains/losses) and $APE_{monthly}$ for for six different PV technologies: (a) a-Si: H, (B) Perovskite, (c) CdTe, (d) CIGS 2, (e) sc-Si and (f) CIGS 1.

$MM_{monthly}$ vs. $APE_{monthly}$ showed a linear relationship in previous research when examined at a particular location, as was mentioned in the introductory section [11,30]. Figure 25 demonstrates that the linearity between the $MM_{monthly}$ and $APE_{monthly}$ is indeed global (see Figure 26 for the daily weighted values). Once more, for wider bandgap PV technologies, the RSE rises.
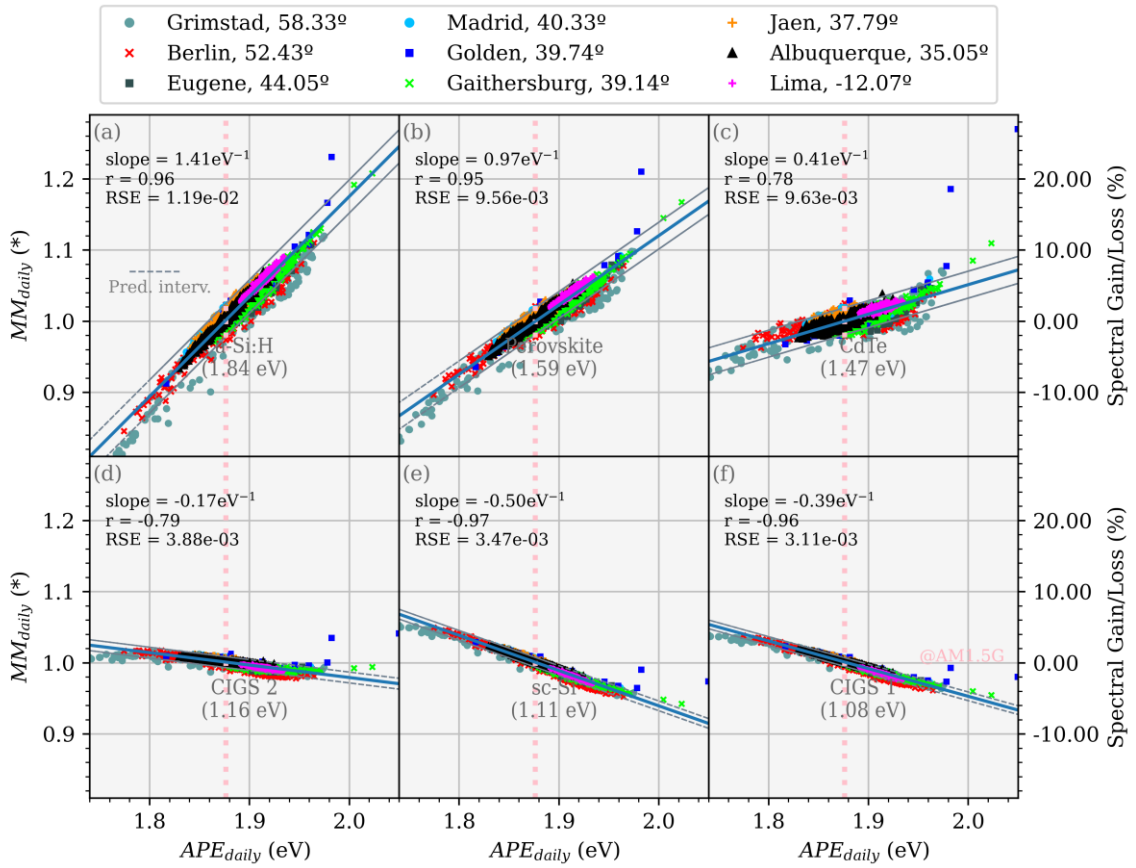
Figure 26. Linear relationship between MM_{daily} and APE_{daily} for six different PV technologies: (a) a-Si:H, (b) Perovskite, (c) CdTe, (d) CIGS 2, (e) sc-Si and (f) CIGS 1. The gray dashed lines indicate the prediction interval. The vertical dotted line indicates APE for the AM1.5G spectrum. RSE and r are the residual standard error and the correlation coefficient, respectively.

Table 2 incorporates the estimate of the half-interval of the prediction interval by fitting the prediction interval with parallel lines to the $MM_{monthly}$ and $APE_{monthly}$ linear regressions, this table also summarize the equations resulting from the global linear regressions. The half-interval in terms of energy gains and losses is indicated by this value, which is expressed as a percentage (100%).

Table 2. List of equations of the global linear regressions between $MM_{monthly}$ and $APE_{monthly}$. These equations can be used to calculate MM using APE on a monthly and annual basis, potentially, for any location in the world. In addition, it shows the approximate half-interval of the prediction interval calculated by assuming the prediction interval as a parallel line.

PV Technology (Bandgap in eV)	Linear Regression equation for $MM =$	Half-prediction interval (10^{-2})	RSE (10^{-3})	r
a-Si (1.84)	$1.57\,eV^{-1} \times APE - 1.95$	1.66	8.32	0.98
Perovskite (1.59)	$1.05\,eV^{-1} \times APE - 0.97$	1.23	6.17	0.98
CdTe (1.47)	$0.41\,eV^{-1} \times APE + 0.23$	1.20	5.98	0.88
CIGS 2 (1.16)	$-0.16\,eV^{-1} \times APE + 1.30$	0.54	2.71	-0.84
sc- Si (1.11)	$-0.48\,eV^{-1} \times APE + 1.89$	0.50	2.49	-0.98
CIGS 1 (1.08)	$-0.37\,eV^{-1} \times APE + 1.70$	0.48	2.38	-0.97

By contrasting Figures 22 and 25, it can be noted that UF/UF^* was ineffective in predicting the spectral impact over a range of climates and latitudes. Even the trend in the spectral gains and losses frequently reported for some PV technologies, such as CIGS and sc-Si, are distorted by this UF/UF^*. This indicator, by definition, employs a unitary SR, which results in a hyperbolically shaped EQE, much different from the EQE found in most PV devices [76], as mentioned in Chapter 2.
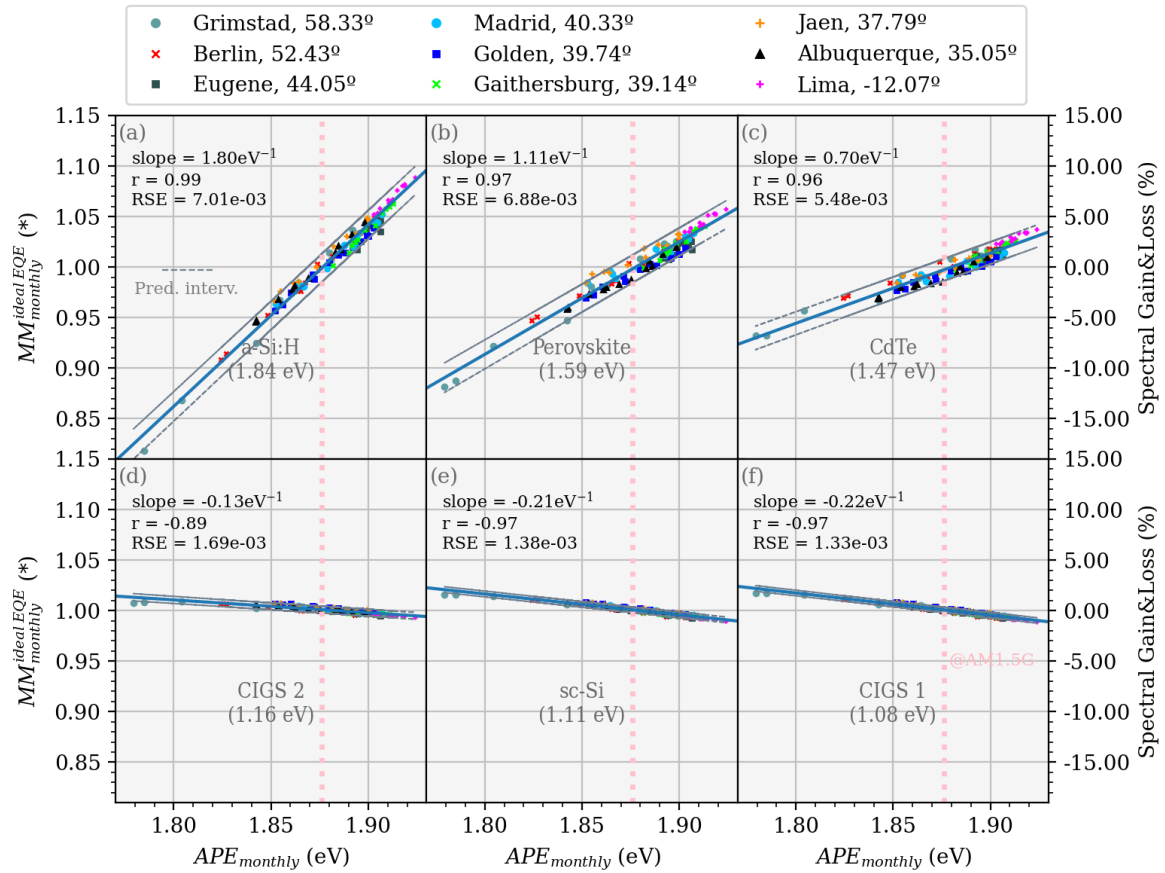
Figure 27. Linear relationship between $MM_{monthly}$ and $APE_{monthly}$ for six different absorbent materials: (a) a-Si: H, (b) Perovskite, (c) CdTe, (d) CIGS 2, (e) sc-Si, (f) CIGS 1. The gray dashed lines indicate the prediction interval. RSE and r are the residual standard error and the correlation coefficient, respectively.

However, by using only the bandgap of a particular PV technology, it is possible to define an ideal step-function EQE and calculate an ideal MM based on this ideal EQE. Figure 27 shows the relationship between the $MM_{monthly}$ for an ideal EQE ($MM_{monthly}^{ideal\,EQE}$) and the $APE_{monthly}$. Interestingly, the linearity between both indicators is preserved. The differences between $MM_{monthly}^{ideal\,EQE}$ and $MM_{monthly}$ will be discussed in the next section.

Notwithstanding the different integration limits between MM and APE, this work proposes three factors that affect the linearity between $MM_{monthly}$ and $MM_{monthly}$ in the ideal scenario (step-function EQE):

1. Being indefinite integrals, the MM ideal and the APE are proportional.

2. Similar to the observations for $IUF/IUF^*_{monthly}$ and $BF_{monthly}$, there is a linear relationship between the integration of various spectral bands. APEs for different integration ranges, such as the bands 450–500 nm with 800-850 nm, can maintain linearity with the APE in the 350–1050 nm range, as demonstrated by Kataoka et al. (2014) [56]. Those findings might support this hypothesis.

3. Irradiance-weighting the MM and APE, as did with $IUF/IUF^*_{monthly}$ and $BF_{monthly}$, supports the $MM_{monthly}$ vs. $APE_{monthly}$ linear relationship.

According to the losses of the experimental relative EQE compared to the ideal solar cell, a measured relative EQE in the calculation of $MM_{monthly}$, increases the linear relationship dispersion.

5.5.2. Comparing the theoretical and experimental $MM_{monthly}$ vs. $APE_{monthly}$ interrelationship
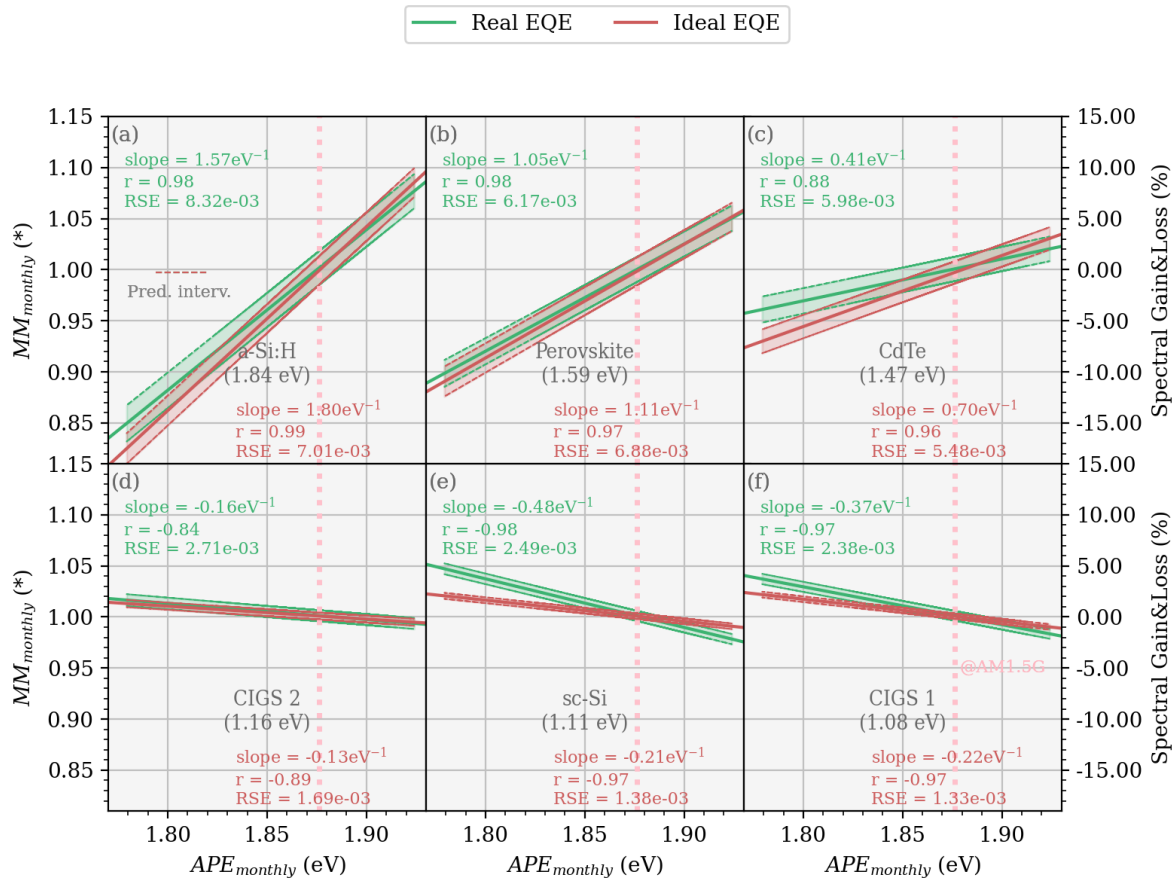
Figure 28. Comparison of $MM_{monthly}$ vs $APE_{monthly}$ linear regressions for real (Figure 5) and ideal EQEs (step-function EQEs).

Figure 28 contrasts ideal (red) and realistic (green) $MM_{monthly}$ vs. $APE_{monthly}$ linear regressions. Realistic devices have smaller slopes than ideal ones for high-bandgap absorbers (a-Si:H, perovskite, and CdTe), which results in decreased sensitivity of $MM_{monthly}$ to changes in $APE_{monthly}$. On the other hand, low-bandgap devices show negative slopes that are more significant for the realistic than for ideal devices. This suggests that the $MM_{monthly}$ is more sensitive to $APE_{monthly}$ changes for real devices. For all devices, it is noted that for $APE_{monthly}$ values below $APE_{AM1.5G}$, the $MM_{monthly}$ for realistic devices is more significant than for ideal ones. This could mean that realistic devices have relative EQE losses that are more pronounced at lower wavelengths than at higher wavelengths, increasing $MM_{monthly}$ for smaller $APE_{monthly}$ and decreasing it for greater $APE_{monthly}$.

In addition, the change in slopes from higher to lower bandgaps suggests that a device with a bandgap and EQE that produces a constant $MM_{monthly}$, independent of $APE_{monthly}$, may exist. The device that exhibits the lowest slope, the CIGS 2, comes close to being immune to spectral variations.
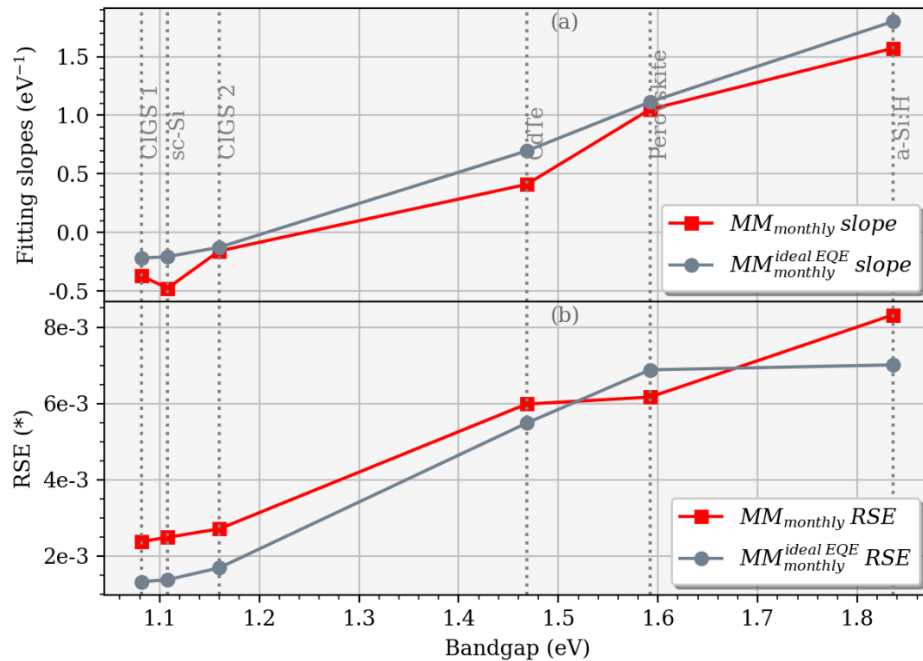
Figure 29. Comparison in (a) slopes and (b) Residual standard errors (RSE's) vs. PV materials bandgaps from the $MM_{monthly}^{ideal\ EQE}$ and $MM_{monthly}$ with $APE_{monthly}$ linear regressions

The slopes and RSE for the $MM_{monthly}$ and $APE_{monthly}$ linear regressions with an ideal EQE ($MM_{monthly}^{ideal\ EQE}$) and realistic EQE are compared in Figure 29 as functions of the bandgap energy. Figure 29 (a) shows a threshold value for an ideal EQE of about 1.2 eV, where slopes increase positively above 1.2 eV and slopes fall negatively below 1.2 eV as the bandgap widens. Moreover, real relative EQE slopes for c-Si and CdTe show a more noticeable deviation from the ideal slopes. The wide prediction interval for CdTe in Figure 28 decreases the discrepancy between the results based on ideal and measured relative EQE, though. On the other hand, the smaller prediction interval of the c-Si increases the discrepancy between the actual and ideal $MM_{monthly}$.

5.6. Conclusions

Chapter 4 showed the ability of the APE and BF to represent the spectral distribution in different sites of variable latitudes and climates in different time scales, in addition to the MM_{annual} and IUF/IUF^*_{annual}. This chapter aimed to study the interrelationships between the PV-device-dependent (MM and IUF/IUF^*) with the -independent (APE and BF). The different time scales (instantaneous, daily, monthly) used to weight spectral indicators by irradiance helped to visualize such interrelationships. On an instantaneous basis, for instance, MM exhibited having two well-differentiated branches given an APE value in Berlin, similar to "Lobster Claws." These "Lobster Claws" shapes seemed to have their origin in very cloudy conditions, that is, at very low irradiances (quite noticeable for irradiances <200 W/m^2) in situations of no clear skies. The monthly weighting of these indicators by irradiance improves the linearity of such an interrelationship because monthly weighting highlights spectra under clear skies, removing the "Lobster Claws" presented in the instantaneous data.

Interestingly, the slopes of the linear regressions, when considering under clear-sky situations, are similar to those of the regressions after monthly weighting the MM. The latter comes from the fact that generally, under clear skies, the irradiances are higher and therefore have a greater participation in the average weighted by irradiance. $IUF/IUF^*_{monthly}$ vs. BF_{annual} exhibited a linear relationship globally when considering the spectral data from the nine selected sites, and this work put forward three possible hypotheses for such an interrelationship. $MM_{monthly}$ and $APE_{monthly}$ had previously been reported to be locally linear. However, the $MM_{monthly}$ vs. $APE_{monthly}$ demonstrated a linear relationship globally in this work. The hypotheses raised for such an interrelationship are similar to those of $IUF/IUF^*_{monthly}$ vs. BF_{annual}.

Part of these results have been published in [106] in the framework of this thesis.

6. Empirical method for the monthly and annual spectral impact prediction

6.1. Introduction

Depending on the site and the PV technology under examination, the effects of the varying spectral distribution on PV performance can vary dramatically. The IEC 61853 standard series envisages methods for making spectral gains and losses on PV performance estimation [6,8,9,113]. The most popular PV energy yield modeling programs, such as PVSyst, Plantpredict, PVwatts, Helioscope, etc., provide simple approximations for calculating the spectral impact using empirical formulas based on factors like air mass and precipitable water. These tools do away with the need for time- and money-consuming procedures for generating an energy rating per the IEC standard 61853-3 based on on-site measurements [8,35,38,41,42]. Meanwhile, many of these empirical calculations do not account for all PV market technologies. Additionally, there is little knowledge about them for varied climates and latitudes [43].

The previous chapter showed that $APE_{monthly}$ and $MM_{monthly}$ exhibit a global linear relationship using experimental data from various latitudes and climates. The linear relationship was different for each PV technology. In addition, that chapter presented a table with the equations of each linear regression with its corresponding approximation of the prediction interval. This fact suggests estimating the $MM_{monthly}$ simply by knowing the $APE_{monthly}$, potentially for any site. This chapter makes use of such a linear relationship to predict the MM_{annual}. In addition, $APE_{monthly}$ and $MM_{monthly}$ will be used from two sites in Brazil (Sao Paulo and Sao José dos Campos) [30] to verify the effectiveness of the proposed method. Finally, this chapter presents two additional spectral indicators, $SAUF$ and SEF, adapted from Rodrigo et al. (2019) [77], to require only irradiance-weighted spectra. Thus, $SEF_{monthly}$ and $SAUF_{monthly}$ aim to predict $MM_{monthly}$ and $IUF/IUF^*{}_{monthly}$, respectively.

6.2. Method verification through experimental data
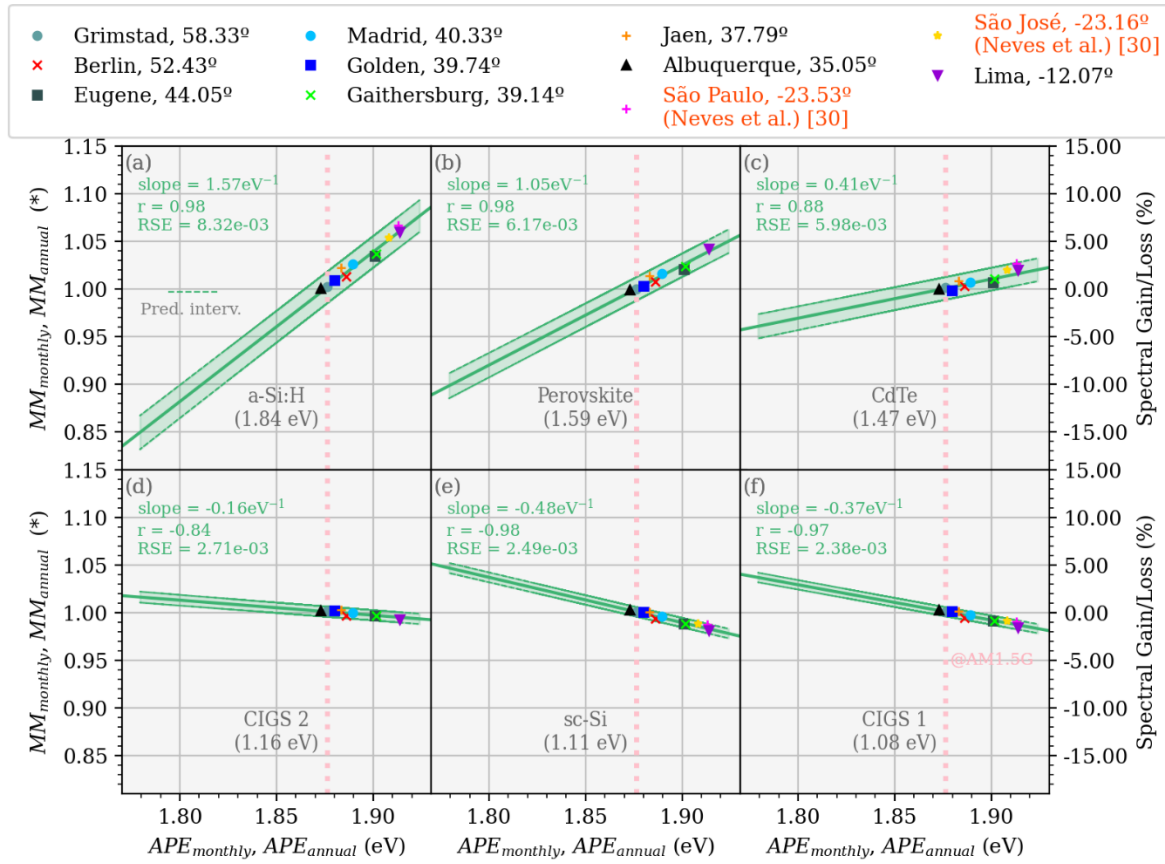
Figure 30. MM_{annual} vs APE_{annual} scatter plot on the $MM_{monthly}$ vs $APE_{monthly}$ linear regression. The annual values are within the monthly linear regression prediction interval.

The estimated prediction intervals of the monthly linear regression are overlaid with a scatter plot of the MM_{annual} against APE_{annual} in Figure 30. The method's ability to anticipate the spectral effects using solely the APE_{annual} and the equations in Table 2 is confirmed by the good agreement with the linear regression and the fact that the MM_{annual} are all within the prediction interval. In addition, data from of APE_{annual} and MM_{annual} from Neves et al. (2021) [30] prove the high accuracy of predicting the MM_{annual} for Sao Paulo and Sao Jose dos Campos.

Table 3 summarizes the prediction sensitivity through the RMSE (Equation 15) ranging from 1.70 to 4.79×10^{-3} for sc-Si, and a-Si:H, respectively. The MBE is also presented following Equation 16. According to the MBE, the predicted MM_{annual} using the APE_{annual} are slightly lower than the calculated based on experimental spectral data.

Table 3. Spectral impact prediction sensitivity from Figure 30 using the empirical linear relationship from Table 2.

	a-Si:H	Perovskite	CdTe	CIGS 2	sc-Si	CIGS 1
RMSE (10^{-3})	4.79	3.46	2.92	1.77	1.70	1.77
MBE (10^{-4})	6.76	3.96	2.69	1.63	1.54	1.35

6.3. Spectral indicators based on average spectra

The suitability of two additional energetic spectral indicators, $SAUF$ and SEF, for forecasting IUF/IUF^* and the irradiance weighted MM, respectively, is assessed. Both additional indicators save computing time by requiring the calculation of an average solar spectrum rather than the instantaneous spectra, as shown in Equation 10. Figure 31 shows the average monthly spectra in the nine locations. Although it is outside the scope of the present work, it is necessary to be particularly attentive to the associated uncertainties that arise when computing these two extra indicators in order to make $SAUF_{monthly}$ and $SEF_{monthly}$ equivalent with $IUF/IUF^*_{monthly}$ and $MM_{monthly}$, respectively. Rodrigo et al. (2019) [77] examined the accuracy of these two additional indicators with respect to MM using synthetic spectra in Granada, Spain depending on the PV technology and seasons. Nevertheless, this thesis demonstrates their direct comparison with their associated indicators based on one-year measured spectral data for different latitudes and climates.
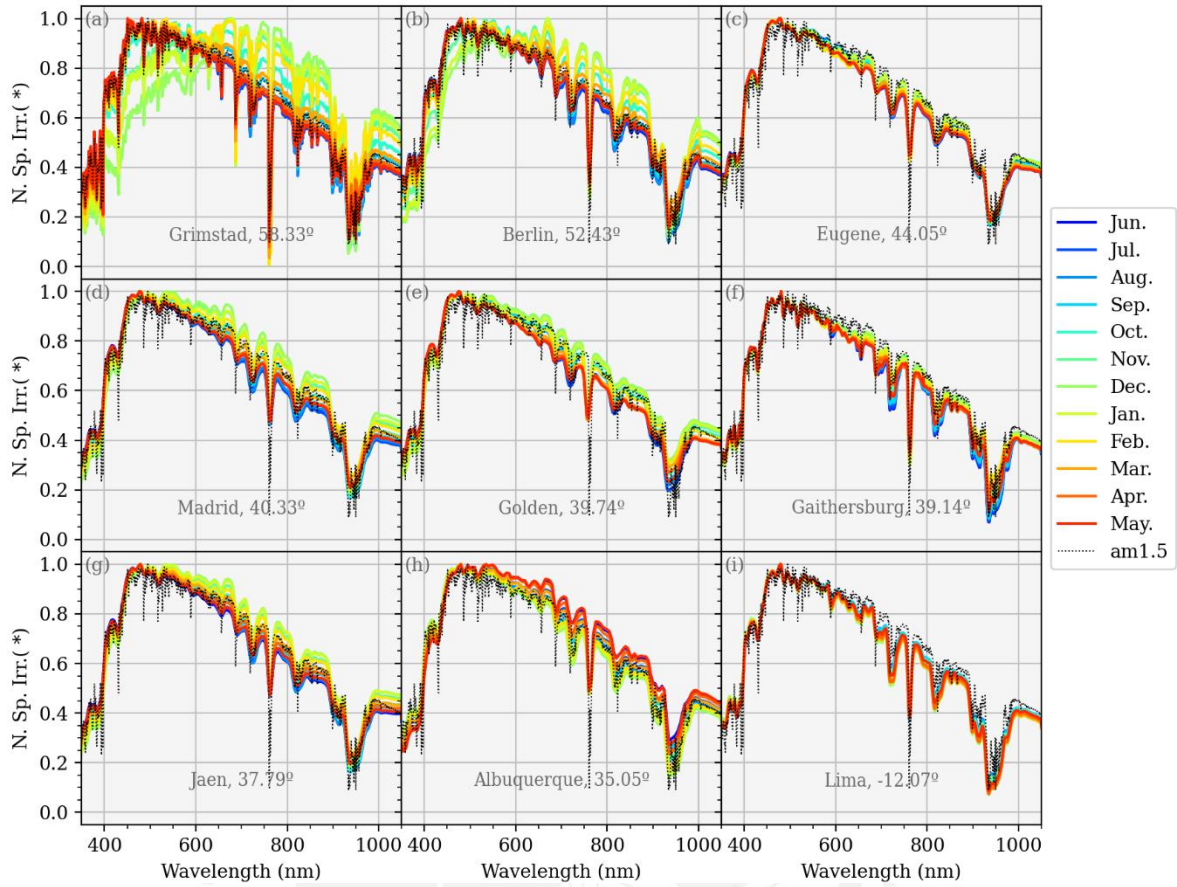
Figure 31. Normalized irradiance-weighted average monthly solar spectral irradiance (N. Sp. Irr.) vs. wavelength for the nine locations. These spectra allowed to calculate $SAUF_{monthly}$ and $SEF_{monthly}$ with Equations 13 and 14, respectively.

6.3.1. Adapted Spectral Average Useful Fraction
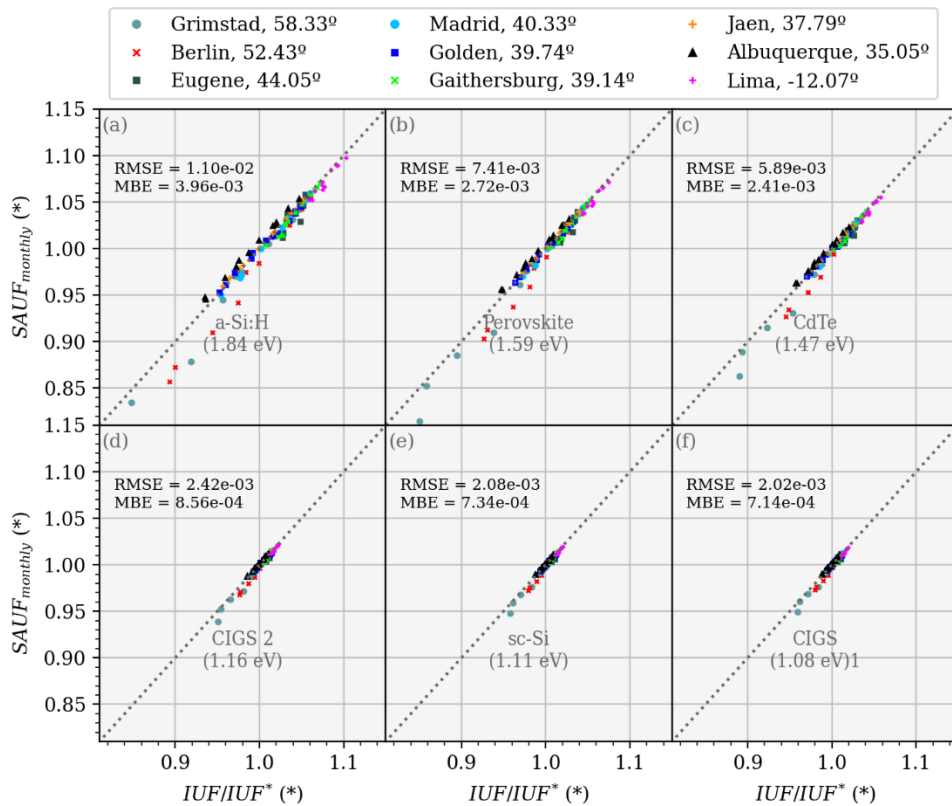
Figure 32. Comparison between the two bandgap-dependent indicators: $SAUF_{monthly}$ and $IUF/IUF^*_{monthly}$

The relationship between the $SAUF_{monthly}$ and the $IUF/IUF^*{}_{monthly}$ is depicted in Figure 32. The RMSE represents the difference in average between the predicted and actual values, in this case, between the $SAUF_{monthly}$ and the $IUF/IUF^*{}_{monthly}$. This statistical indicator is, in terms of its linear relationship with the $BF_{monthly}$ in Figure 21, smaller than the prediction interval and even has an order of magnitude similar to the RSE. This comparison could indicate that $IUF/IUF^*{}_{monthly}$ is well represented by the $SAUF_{monthly}$ because of the small RMSE.

6.3.2. Adapted Spectral Enhancement Factor
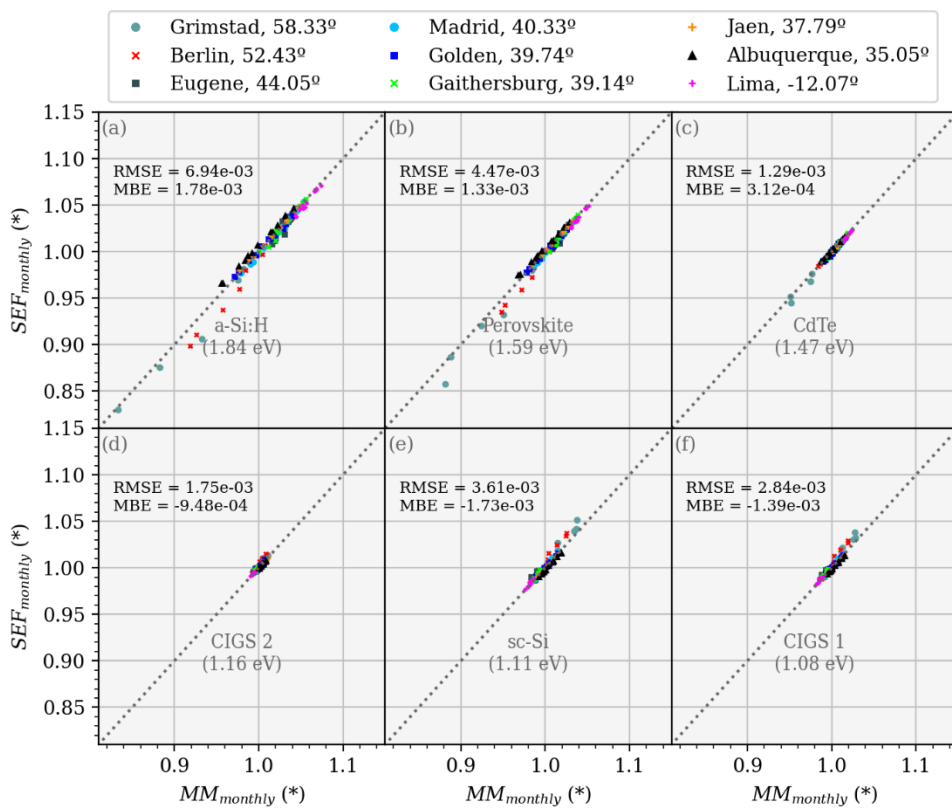
Figure 33. Comparison between the two EQE-dependent KPIs: $SEF_{monthly}$ and $MM_{monthly}$

Similar to Figure 32, Figure 33 depicts the relationship between $SEF_{monthly}$ and $MM_{monthly}$. The RMSE is also small in this case, following the same reasoning as Figure 32. This finding demonstrate that the $SEF_{monthly}$ offers a reliable estimate of the $MM_{monthly}$.

6.4. Conclusions

Chapter 5 analyzed global interrelationships between PV-device-independent and -dependent spectral indicators. $MM_{monthly}$ vs. $APE_{monthly}$ stands out for being the most used spectral indicators in the PV community. Such interrelationships proved to be linear for six different PV technologies. This chapter focused mainly on using the predictive character of such an interrelationship to determine the MM_{annual} uniquely requiring the APE_{annual} for the nine selected sites. Furthermore, as a form of validation, this method was shown to predict the MM_{annual} reported for two sites in Brazil (Sao Paulo and Sao Jose

dos Campos) by knowing only the reported APE_{annual}. This method presented an RMSE between 1.70 and 4.79%, with the most significant discrepancy being for a-Si:H, considering it also has a broader prediction interval than the other PV technologies. However, all the results were within the limits of the prediction interval of such a linear regression. To further reduce the calculation, use was made of two spectral indicators adapted to require only weighted irradiance spectra, $SEF_{monthly}$ and $SAUF_{monthly}$, to predict the $MM_{monthly}$ and $IUF/IUF^*{}_{monthly}$, respectively. The results showed that the RMSE found are smaller than the prediction intervals of their respective linear regressions with the PV-device independent spectral indicators $APE_{monthly}$ and $BF_{monthly}$. This indicates that they can make an accurate estimate of both the $MM_{monthly}$ and the $IUF/IUF^*{}_{monthly}$.

These results are already reported in [106].
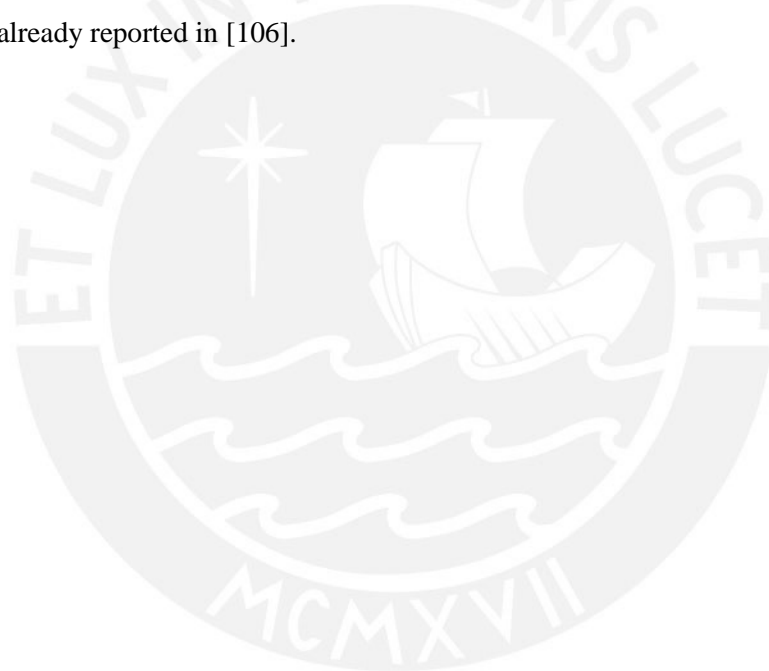
7. Annual spectral impact determination through synthetic spectral data

7.1. Introduction

Simulation of spectral irradiance is useful when field measurements are unavailable. Many tools to simulate spectra are available depending on the spectral region resolved, computation algorithm, geometrical schematization, license type, etc. [45]. Physical models generally use the Radiative Transfer Theory to estimate ground radiation directly based on cloud properties, aerosol optical depth, water vapor, and ozone as inputs through calculations in different wavelength bands [34]. These calculations are commonly used in atmospheric sciences, such as MODTRAN [114], libRadtran [115], and SBDART [116]. However, these models usually require a long execution time, which makes them unsuitable for engineering applications [34]. In solar PV energy applications, some models with less computational cost are helpful. For example, SPECTRAL2 allows us to calculate spectra under clear skies. SMARTS presented notable improvements in spectral resolution and precision to model solar spectra under clear skies, having wide approval in the PV community [34,105].

On the other hand, SEDES2 and SolarSpectrum [117] are highlighted among the most common all sky conditions models. The National Solar Radiation Database (NSRDB) Data viewer now includes on-demand spectral data recently released by the National Renewable Energy Laboratory (NREL) [47]. Currently, longitudes from 25 °E to 175 °W and latitudes from 20 °S to 60 °N are covered by the spectral on-demand data. The Fast All-sky Radiation Model for Solar applications with Narrowband Irradiances on Tilted surfaces (FARMS-NIT), a novel radiative transfer model, is used to calculate the spectral data provided by the NSRDB [49]. Using SMARTS to acquire the optical characteristics of the atmosphere, FARMS-NIT then solves the radiative transfer equation using a pre-calculated look-up table to produce a theoretical solar spectrum under all-sky conditions [46,48,51]. This model incorporates the advantages of existing meteorological and solar energy spectral models.

The synthetic spectra generated by FARMS-NIT demonstrated high precision when predicting spectra in clear skies. However, such effectiveness decreases for spectra in cloudy sky conditions for some sites

[50,51]. Studies for these synthetic spectra at low latitudes and the limit of the scope of available FARMS-NIT spectra are scarce [50]. Since this work focuses on analyzing the spectral influences on PV performance at different latitudes and climates, the validation of synthetic data with experimental spectral data for Lima is presented. This validation aims to give notions about the uncertainties of the synthetic data that is finally propagated on the global relationship between $APE_{monthly}$ and $MM_{monthly}$ presented in chapter 5.

7.2. Synthetic spectral data validation for a low latitude site

Comparing the experimental and synthetic spectral data sets through comparing intensities between the different spectral channels and time is impractical for the objectives initially set in the introduction section. Since this work focuses on spectral indicators, here it proposes validating the synthetic spectral data using the APE on a monthly and annual scale, i.e., this chapter validates the goodness of the synthetic spectral data to predict the monthly and annual behavior of the experimental spectral distribution in Lima, Peru. For this purpose, this work uses experimental spectral data from March 2019 to February 2020 in Lima in the same tilted plane (20° tilt angle, facing due North).
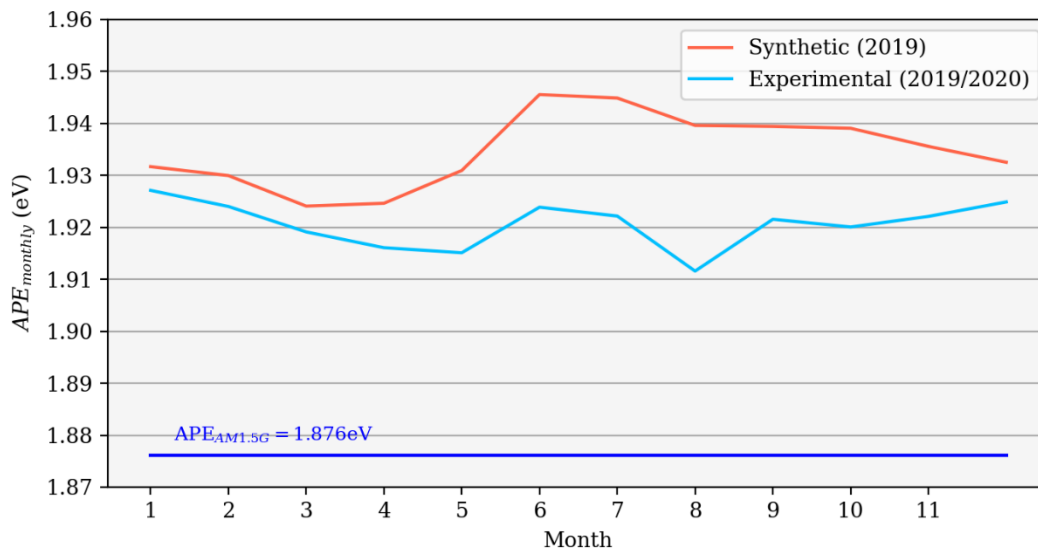
Figure 34. Synthetic (NSRDB) and experimental average monthly irradiance-weighted APE.

Figure 34 compares the 12 months of experimental spectral data (2019-2020) and the synthetic spectral data (2019). This means that January and February correspond to 2020, and the following months correspond to 2019 for the experimental data. The seasonal trends are similar in the winter months (June to September) for both data sets. However, the $APE_{monthly}$ during the 12 months of the synthetic spectral data overestimates the corresponding ones from the experimental data. As discussed above, the $APE_{monthly}$ for both data sets does not exhibit evident seasonality, as is expected for the low latitude.
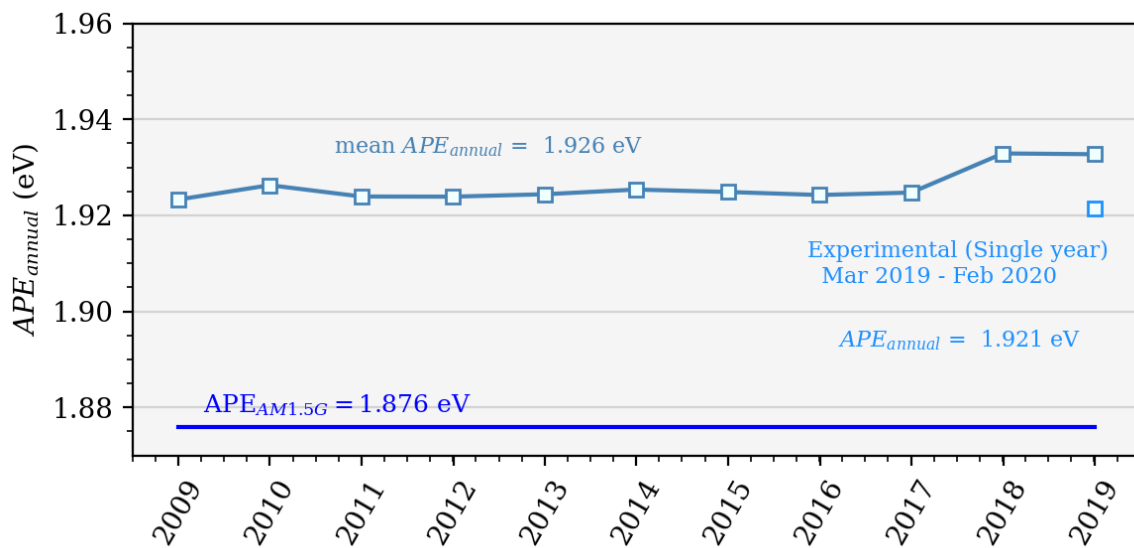
Figure 35. Synthetic (from 2009 to 2019) and the experimental (12 months) annual average irradiance-weighted APE's (APE_{annual})

Additionally, Figure 35 describes the spectral distribution in Lima using the APE_{annual}. The experimental data period (03.2019 to 02.2020) follows the theoretical data period (2009 - 2019). The mean of the synthetic APE_{annual} marginally differs from the experimental one at around 0.005 eV. Furthermore, the APE_{annual} of the synthetic data suggests a blue shift of the spectral distribution in Lima for the entire synthetic data, similar to the experimental results for the composed year (2019 - 2020).
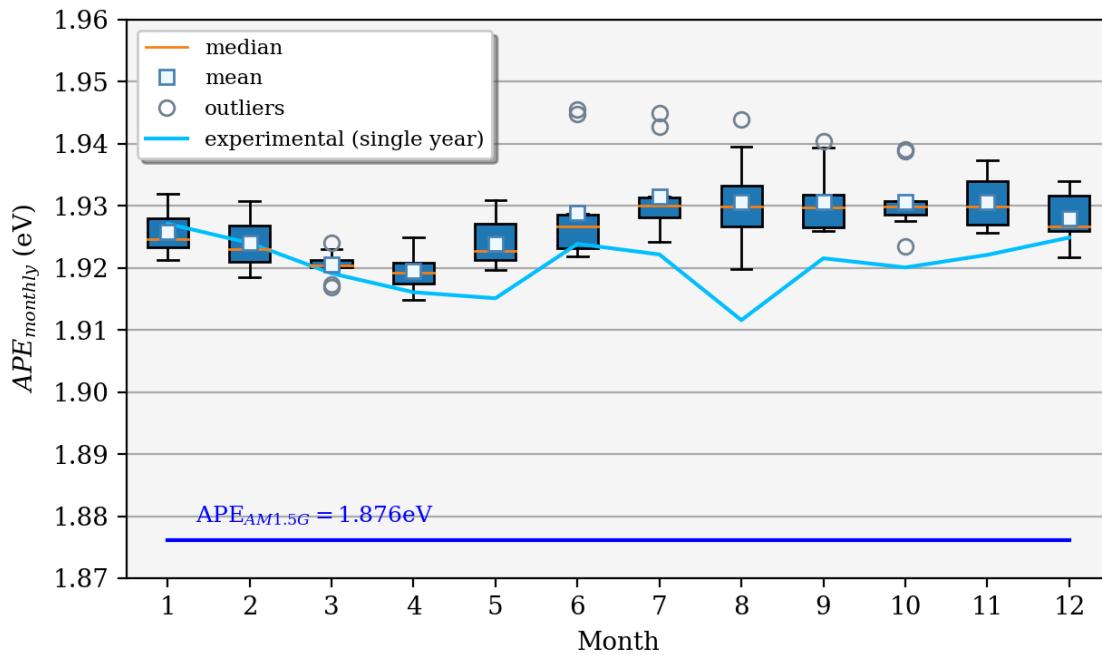
Figure 36. Boxplots of the synthetic (NSRDB) average monthly irradiance-weighted APE along with the experimental one superposed in the light blue line.

The synthetic $APE_{monthly}$ distribution for the 11 years of synthetic data is shown in Figure 36 as a monthly boxplot with 10 data points corresponding to each year in each box. The synthetic results show a slight seasonality, with a mean $APE_{monthly}$ value being lowest in the autumnal months around April and highest in the winter months around July.

Knowledge of atmospheric variables, including air mass, cloud cover, diffuse irradiance fraction, albedo, and the atmospheric characteristics that define the spectral distribution under clear and overcast sky conditions, would be necessary to explain such seasonality in the spectral distribution. The scope of this work does not include that analysis.

The experimental $APE_{monthly}$ exhibits a different behavior and distinctive values from July to November but a similar seasonality trend and values to those of the synthetic during the first half of the year, including December. The former is associated with the summer months (December, January, February, and March), characterized by many clear sky days. It may be assumed that during these months, the APE values associated with clear skies and high irradiance will contribute more significantly to the $APE_{monthly}$. As previously mentioned, SMARTS, which has shown a high

spectrum prediction accuracy for clear-sky, provides accurate information on the optical characteristics of the atmosphere for FARMS-NIT. The latter could account for the observed agreement between experimental and synthetic $APE_{monthly}$. When low irradiances prevail in the other months, including atmospheric components for cloudy skies may increase the accuracy of spectrum modeling.

7.3. Testing the spectral impact' empirical method with synthetic data

The experimental $MM_{monthly}$ and $APE_{monthly}$ in the nine chosen sites demonstrated in Chapter 5 to have a global linear relationship. Chapter 6 used this global linear relationship to predict the annual spectral impact on PV performance for the chosen sites and two additional sites in Brazil using their APE_{annual} s. Such a linear relationship constituted an empirical and direct method of obtaining the spectral impact on a weighted annual (monthly) basis from a weighted annual (monthly) APE. To broaden the validation scope of this new method, this work resorts to applying the interrelation analysis to synthetic data generated by FARMS -NIT, covering 14 locations with low, medium, and high latitudes.
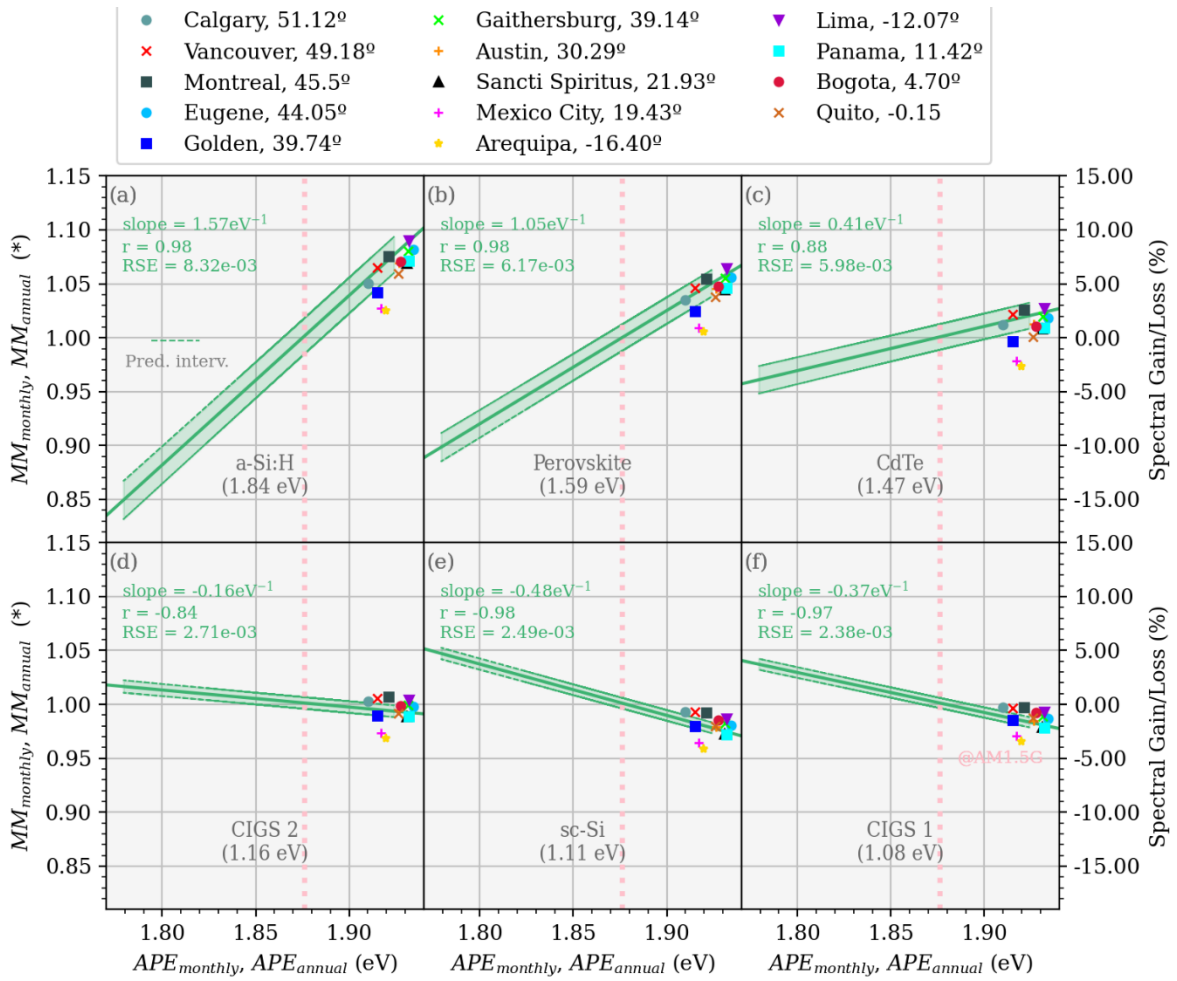
Figure 37. Synthetic MM_{annual} vs APE_{annual} scatter plot on the experimental $MM_{monthly}$ vs $APE_{monthly}$ linear regression. Slopes and prediction intervals correspond to experimental data from Table 2 in Chapter 5.

Figure 37 depicts the points corresponding to the $MM_{monthly}$ and $APE_{monthly}$ of the synthetic data on the linear regressions of the experimental data. Interestingly, despite the uncertainties that this data presents compared to the experimental data, as demonstrated in the previous section, the synthetic results annually follow the trends of the experimental linear regressions. In addition, for wider bandgap technologies, most of the annual synthetic results are within the experimental prediction interval. Arequipa and Mexico City are the sites whose results are farthest from what was predicted experimentally. Additionally, the synthetic spectra exhibit an extra blue-shifted APE_{annual} compared to the experimental results (Lima, Gaithersburg, Golden, and Eugene), i.e., in these cases, the annual synthetic APE of the year considered (2019) overestimates the experimental APE in the years mentioned in Chapter 3. However, the fact that most synthetic data points fall within the experimentally acquired prediction interval affirms the validity of the proposed method for predicting the annual

spectral impact on PV performance. This makes evident the global character of this method proposed in the present work.
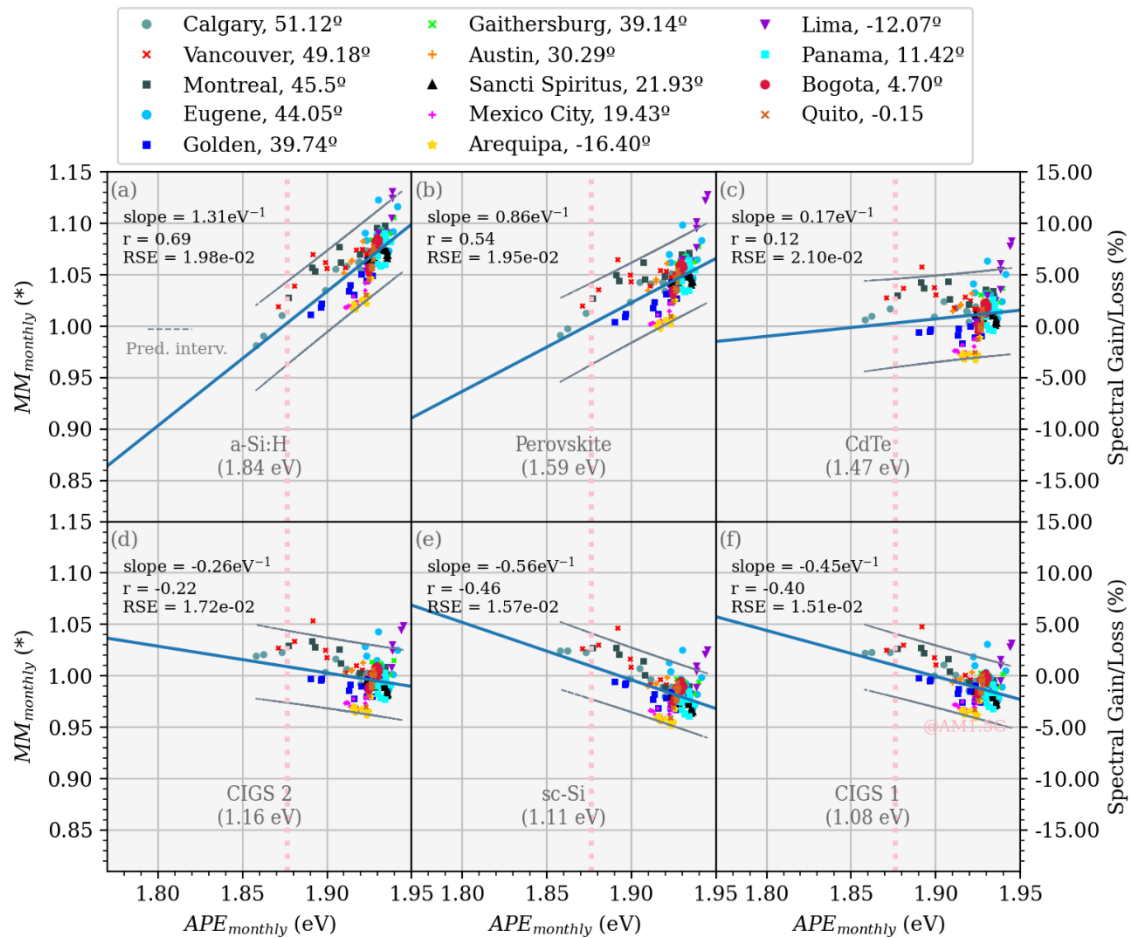
Figure 38. Linear relationship between $MM_{monthly}$ (and spectral gains/losses) and $APE_{monthly}$ based on synthetic data of 14 locations for six different PV technologies: (a) a-Si: H, (B) Perovskite, (c) CdTe, (d) CIGS 2, (f) sc-Si and (g) CIGS 1. Slopes and prediction intervals are recalculated with synthetic data.

Figure 38 shows the results of $MM_{monthly}$ and $APE_{monthly}$ based on the synthetic data. The slopes and prediction intervals correspond to the linear fit recalculated from the synthetic data. The synthetic data points exhibit a wide dispersion, as seen in the RSE above 1.52×10^{-2}, with a small absolute value r, even 0.12 for CdTe and -0.22 for CIGS 2. This wide dispersion makes it impractical to represent a linear relationship, and thus, the method based solely on synthetic data does yield the same predictive character as when based on experimental data. Also, a blue shift is observed in the monthly results compared to the experimental data. In this sense, there is no evident relationship for the $MM_{monthly}$ and $APE_{monthly}$ based on synthetic data. In contrast, the MM_{annual} and APE_{annual} based on synthetic

spectra do follow the predictive trends, and in most cases, wider bandgaps spectral impact can be predicted by the method proposed here.

7.4. Conclusions

This chapter applied the method proposed in the previous chapters to synthetic spectral data from 14 different sites, covering a wide range of low, mid, and high latitudes. The main purpose of this chapter was to evaluate if the linearity and predictive character observed between experimental MM and APE data was reproducible with synthetic data. First, this chapter compared the synthetic spectral data with experimental spectral data in Lima, taking the APE as a representative indicator of the spectral distribution. The comparison indicates that the synthetic and experimental monthly APE values differ most in the winter months (June, July, August, and September) and are most similar in the summer months (December, January, February, and March). The suitability of the models to synthesize spectral data under clear skies is confirmed. The discrepancy during the winter months most likely originates from the uncertainty of the models to synthesize spectral data under cloudy skies. Lima, commonly in winter, presents a uniform cloudiness and few moments of sky clarity.

A validation was also made with historical synthetic data, thus demonstrating that the APE_{annual}s are close to the experimental value with only a slight difference of 0.003 eV. By superimposing the results of MM_{annual} and APE_{annual} using synthetic data on experimental linear regressions, the synthetic MM_{annual} and APE_{annual} maintain the trend suggested by the linear regressions of the experimental spectral data. However, it was not possible to reconstruct the monthly linear regressions using synthetic spectra because of the wide dispersion.

Thus, the trends exhibited by the annual results based on synthetic spectra attest to the goodness of the prediction of the spectral impact presented by the linear regressions that this thesis proposes. However, the uncertainties associated with the synthetic data are outside the scope of this work, and therefore it is not possible to determine the prediction accuracy. In addition, performing the monthly regression proposed in this method is impractical due to the lack of information about the uncertainties of the synthetic data. The above synthetic spectral data validation for Lima was reported in [50].

8. Conclusions and outlook

This work analyzed the interrelationships between different spectral indicators based on GTI, GHI, and GNI spectral data from nine sites around the world measured at ground level. Taking the latitude as an implicit variable of the spectral distribution, a general decreasing trend of the APE_{annual} was observed as the absolute value of latitude increased. While there is such a general trend for the selected sites, the impact of site-specific conditions on the APE_{annual} variation can be significant, rendering the latitude inadequate to predict the APE_{annual}. Furthermore, the seasonal spectrum variation for GTIs exhibited a relationship with latitude, with larger $APE_{monthly}$ variations at higher latitudes. Both relations between the APE and the latitude originate from the dependence of the spectral distribution on the AM, which is a composite function of latitude. The APE and the BF verified condensing the spectral distribution by a single scalar value in various time scales. Also, although the APE and the BF can represent the spectral distribution as a scalar value and a bijective relationship was reported, they can differ in indicating blue- and red-shift spectra for the same dataset, as demonstrated in Golden.

The empirical relationships between device-dependent and -independent indicators offer a practical alternative for calculating the spectral impact. This work reviewed the general relationship between the $IUF/IUF^*_{monthly}$ and the $BF_{monthly}$. These two indicators exhibit a linear relationship that could be related to the form of their equations assuming proportionality between integrated regions of the spectrum. This supposed proportionality would be accentuated for extensive data by applying the weighted average to irradiance, contributing to the linearity between these two indicators.

On the other hand, interestingly, the $IUF/IUF^*_{monthly}$ and $APE_{monthly}$ present a linear relationship and even with a lower RSE than with the $BF_{monthly}$.

The linear relationship between $MM_{monthly}$ and $APE_{monthly}$ was shown globally. This work finds this relationship of great significance because it allows a direct estimation of the spectral impact on a monthly basis. Contrasting this linear relationship with the one for an ideal EQE allows some additional conclusions. On the one hand, it allows us to give three hypotheses that would contribute to the explanation of such a relationship. These are very similar to those found for the $IUF/IUF^*_{monthly}$ vs.

$BF_{monthly}$ since the variable term of MM with ideal EQE resembles the inverse of the APE. On the other hand, the comparison of the ideal and experimental $MM_{monthly}$ as a function of the $APE_{monthly}$ gives us information on how the shape of the EQE affects the spectral sensitivity of different PV technologies. Then the linear regression equations between the $MM_{monthly}$ and $APE_{monthly}$ exhibit a predictive character by allowing us to determine the value of MM_{annual} from only knowing the APE_{annual} with a variable RSE depending on the PV technology.

Furthermore, the present work evaluated the global validity with multi-climatic spectral data of two alternative indicators, $SAUF$ and SEF, which are equivalent to the IUF/IUF^* and the irradiance-weighted MM, respectively. These two indicators gave a good estimate of their equivalent indicators on a monthly scale as expressed by their RMSE comparable to the RSE in their correspondent predictive linear regression.

Next, this work validated Lima's on-demand synthetic spectral data obtained from the NSRDB using the APE. Verifying that in the summer months, there is a better prediction of the experimental spectral data; in the winter months, it is the opposite. This would be due to the accurate spectral forecast that FARMS-NIT has for clear skies, unlike cloudy skies. Finally, the synthetic spectral data from the NSRDB of 14 locations were used to validate the proposed method to predict the annual spectral impact from the APE_{annual}. Despite the uncertainties associated with the synthetic spectral data, the results follow the trend of the global linear regressions of $MM_{monthly}$vs. $APE_{monthly}$, qualitatively verifying their functionality.

In this way, this thesis experimentally showed that linear relationships for different spectral indicators remain valid globally. It also established three hypotheses that support such experimental evidence, thus reducing the calculation complexity of the spectral impact potentially for any site and a qualitative validation with synthetic spectral data. Therefore, the results found here increase the knowledge base in evaluating the spectral effects on the energy yield in a particular climate and for a given technology. For future works, although this method allowed us to predict the spectral impact at two locations in Brazil, better accuracy of the proposed method would imply adding more sites to the linear regression. In addition, a study of the propagation of uncertainties of the spectra extrapolation methods on the

different spectral indicators could also be added. Likewise, a deeper analysis of the uncertainties in the synthetic data would allow a quantitative validation of the proposed method.

A. Publications

Publications in the frame of this thesis:

1) <u>M. A. Sevillano-Bendezú</u>, M. Khenkin, G. Nofuentes, J. de la Casa, C. Ulbrich, J. A. Töfflinger. *Predictability and interrelations of spectral indicators for PV performance in multiple latitudes and climates*. 2022. Solar Energy. Volume 259, 174-187.
Doi: https://doi.org/10.1016/j.solener.2023.04.067 (**Q1 scopus**)

2) <u>M. A. Sevillano-Bendezú</u>, V. Pleshcheva, B. Calsi, L. A. Conde , J. Montes-Romero, J. Aguilera Tejero, J. de la Casa, J. A. Töfflinger. *Assessing the accuracy of analytical methods for PV module electric parameter extraction under different sky conditions*. 2023. **Under review in Renewable Energy Elsevier** (**Q1 scopus**).

3) <u>M. A. Sevillano-Bendezú</u>, L A Conde, J de la Casa, J A Töfflinger. *Average photon energy assessment based on modelled spectra from the National Solar Radiation Database for Lima, Peru*. 2022. J. Phys.: Conf. Ser. 2180 012018.
DOI: https://iopscience.iop.org/article/10.1088/1742-6596/2180/1/012018/meta (**Q4 scopus**)

4) G. A. Farias-Basulto, <u>M A Sevillano-Bendezú</u>, M. Riedel, M. Khenkin, R. Schlatmann, R. Klenk, C. Ulbrich. *Analysis of measured annual solar spectra at different angles in central Europe*. 2022. **Under review in Solar Energy Elsevier** (**Q1 scopus**).

5) M. A. Jara Zamalloa, <u>M. A. Sevillano-Bendezú</u>, C. Ulbrich, G. Nofuentes, R. Grieseler, J. A. Töfflinger. Overirradiance Conditions and their Impact on the Spectral Distribution at Low- and Mid-Latitude Sites. 2023. Solar Energy volumen 259 99-106.
DOI: https://doi.org/10.1016/j.solener.2023.05.010 (**Q1 scopus**)

6) G. S. Kinsey, N. C.Riedel-Lyngskær, M Alonso-Abella, M Boyd, M Braga, C Shou, R R Cordero, B Duck, C J Fell, S Feron, G E.Georghiou, N Habryl, J J.John, N Ketjoy, G López, A Louwen, E Loyiso Maweza, T Minemoto, A Mittal, C Molto, G Neves, G Nofuentes Garrido, M Norton, B R Paudyal, E Bueno Pereira, Y Poissant, L Pratt, Q Shen, Th Reindl, M Rennhofer, C DRodríguez-Gallegos, R Rüther, W van Sark, <u>M A Sevillano-Bendezú</u>, H Seigneur, J A Tejero, M Theristis, J A Töfflinger, C Ulbrich, W Amaral Vilela, X Xia, M A Yamasoe. *Impact of measured spectrum variation on solar photovoltaic efficiencies worldwide*. 2022. Renewable Energy 2180 012018.
DOI: https://doi.org/10.1016/j.renene.2022.07.011 (**Q1 scopus**)

7) L A Conde, J R Angulo, <u>M A Sevillano-Bendezú</u>, G Nofuentes, J A Töfflinger, J de la Casa. *Spectral effects on the energy yield of various photovoltaic technologies in Lima (Peru)*. 2021. Energy 223 120034.
DOI: https://doi.org/10.1016/j.energy.2021.120034 (**Q1 scopus**)

Other publications involving the author as a PhD fellow

8) J Dulanto, S Fengler, <u>M A Sevillano-Bendezú</u>, R Grieseler, J A Guerra, J A Töfflinger, Th Dittrich. *Hydrogen effects at sputtered Tb-doped AlNxOy:H / c-Si(p) interfaces: A transient surface photovoltage spectroscopy study*. 2022. Thin Solid Films Volume 759 139474.
DOI: https://doi.org/10.1016/j.tsf.2022.139474 (**Q1 scopus**)

9) A E Berastain, L A Conde, J Angulo, A M Carhuavilca, M García, <u>M A Sevillano-Bendezú</u>, J Montes-Romero, J De la Casa, L Chirinos and J A Töfflinger. *Resolving challenges of monitoring PV systems: a case study for three 1.5 kW generators in Lima, Peru*. 2022. J. Phys.: Conf. Ser. 2180 012006.
DOI: https://iopscience.iop.org/article/10.1088/1742-6596/2180/1/012006/meta (**Q4 scopus**)

10) J Dulanto, <u>M A Sevillano-Bendezú</u>, R Grieseler, J A Guerra, L Korte, T Dittrich and J A Töfflinger. *Silicon interface passivation studied by modulated surface photovoltage spectroscopy*. 2021. J. Phys.: Conf. Ser. 1433 012007.

DOI: https://iopscience.iop.org/article/10.1088/1742-6596/1841/1/012003/meta (**Q4 scopus**)

11) M A Zamalloa Jara, H Berg, L A Conde, <u>M A Sevillano-Bendezú</u>, A M Carhuavilca, R Grieseler and J A Töfflinger. *Extreme Overirradiance events and their spectral distribution in Lima, Peru.* 2021. J. Phys.: Conf. Ser. 1841 012006.
DOI: https://iopscience.iop.org/article/10.1088/1742-6596/1841/1/012006 (**Q4 scopus**)

12) R Perich, <u>M A Sevillano-Bendezú</u>, J Montes-Romero, L Conde, J R Angulo. J de la Casa, J A Töfflinger. *Study of analytical methods for extracting electric parameters of thin film photovoltaic modules.* 2020. Tecnia vol 30 1 53-58.
(**Non-peer-reviewed journal**)

13) *Implementation of a laboratory for the outdoor characterization of photovoltaic technologies under the climatic conditions of Lima.* 2020. Tecnia vol 30 1 80-89. L A Conde, J Montes-Romero, A Carhuavilca, R Perich , J A Guerra, <u>M A Sevillano-Bendezú</u>, B Calsi, J R Angulo, J de la Casa J A Töfflinger.
(**Non-peer-reviewed journal**)

References

[1]   IRENA 2022 *World Energy Transitions Outlook 2022: 1.5°C Pathway* (Abu Dhabi)

[2]   IRENA 2022 *Renewable capacity statistics 2022* (Abu Dhabi)

[3]   Belluardo G, Ingenhoven P, Sparber W, Wagner J, Weihs P and Moser D 2015 Novel method for the improvement in the evaluation of outdoor performance loss rate in different PV technologies and comparison with two other methods *Sol. Energy* **117** 139–52

[4]   Moser D, Del Buono M, Jahn U, Herz M, Richter M and De Brabandere K 2017 Identification of technical risks in the photovoltaic value chain and quantification of the economic impact *Prog. Photovoltaics Res. Appl.* **25** 592–604

[5]   International Energy Agency 2020 *Report IEA-PVPS T13-18:2020 Uncertainties in Yield Assessments and PV LCOE*

[6]   International Energy Agency 2020 *Report IEA-PVPS T13-20:2020 Climatic Rating of Photovoltaic Task 13 Performance, Operation and Reliability of Photovoltaic Systems*

[7]   Schweiger M and Herrmann W 2015 Energy Rating Label for PV Modules for Improving Energy Yield Prediction in Different Climates *31st Eur. Photovolt. Sol. Energy Conf. Exhib.* 1888–92

[8]   Ruben Vogt M, Riechelmann S, Gracia-Amillo A M, Driesse A, Kokka A, Maham K, Karha P, Kenny R, Schinke C, Bothe K, Blakesley J, Music E, Plag F, Friesen G, Corbellini G, Riedel-Lyngskar N, Valckenborg R, Schweiger M and Herrmann W 2022 PV Module Energy Rating Standard IEC 61853-3 Intercomparison and Best Practice Guidelines for Implementation and Validation *IEEE J. Photovoltaics* **12** 844–52

[9]   Blakesley J C, Huld T, Müllejans H, Gracia-Amillo A, Friesen G, Betts T R and Hermann W 2020 Accuracy, cost and sensitivity analysis of PV energy rating *Sol. Energy* **203** 91–100

[10]   Schweiger M and Herrmann W 2015 Comparison of energy yield data of fifteen PV module technologies operating in four different climates *2015 IEEE 42nd Photovoltaic Specialist Conference (PVSC)* (IEEE) pp 1–6

[11]   Dirnberger D, Blackburn G, Müller B and Reise C 2015 On the impact of solar spectral irradiance on the yield of different PV technologies *Sol. Energy Mater. Sol. Cells* **132** 431–42

[12]   Kinsey G S, Riedel-Lyngskær N C, Miguel A-A, Boyd M, Braga M, Shou C, Cordero R R, Duck B C, Fell C J, Feron S, Georghiou G E, Habryl N, John J J, Ketjoy N, López G, Louwen A, Maweza E L, Minemoto T, Mittal A, Molto C, Neves G, Garrido G N, Norton M, Paudyal B R, Pereira E B, Poissant Y, Pratt L, Shen Q, Reindl T, Rennhofer M, Rodríguez-Gallegos C D, Rüther R, van Sark W, Sevillano-Bendezú M A, Seigneur H, Tejero J A, Theristis M, Töfflinger J A, Ulbrich C, Vilela W A, Xia X and Yamasoe M A 2022 Impact of measured spectrum variation on solar photovoltaic efficiencies worldwide *Renew. Energy* **196** 995–1016

[13]   Ripalda J M, Chemisana D, Llorens J M and García I 2020 Location-Specific Spectral and Thermal Effects in Tracking and Fixed Tilt Photovoltaic Systems *iScience* **23**

[14]   Haegel N M, Atwater H, Barnes T, Breyer C, Burrell A, Chiang Y-M, De Wolf S, Dimmler B, Feldman D, Glunz S, Goldschmidt J C, Hochschild D, Inzunza R, Kaizuka I, Kroposki B, Kurtz S, Leu S, Margolis R, Matsubara K, Metz A, Metzger W K, Morjaria M, Niki S, Nowak S, Peters I M, Philipps S, Reindl T, Richter A, Rose D, Sakurai K, Schlatmann R, Shikano M, Sinke W, Sinton R, Stanbery B J, Topic M, Tumas W, Ueda Y, van de Lagemaat J, Verlinden P, Vetter M, Warren E, Werner M, Yamaguchi M and Bett A W 2019 Terawatt-scale

photovoltaics: Transform global energy *Science (80-.).* **364** 836–8

[15]   Jordan D C, Haegel N and Barnes T M 2022 Photovoltaics module reliability for the terawatt age *Prog. Energy* **4**

[16]   Pooltananan N, Sripadungtham P, Limmanee A and Hattha E 2010 Effect of spectral irradiance distribution on the outdoor performance of photovoltaic modules *ECTI-CON2010: The 2010 ECTI International Confernce on Electrical Engineering/Electronics, Computer, Telecommunications and Information Technology* pp 71–3

[17]   Jardine C, Betts T, Gottschlg R, Infield D G and Lane K 2002 Influence of spectral effects on the performance of multijunction amorphous silicon cells *Proc. PV Eur. – From PV Technol. to Energy Solut.* (Rome, Italy)

[18]   Williams S R, Betts T R, Helf T, Gottschalg R, Beyer H G and Infield D G 2003 Modelling long-term module performance based on realistic reporting conditions with consideration to spectral effects *3rd World Conference onPhotovoltaic Energy Conversion, 2003. Proceedings of* vol 2 pp 1908-1911 Vol.2

[19]   Kojima A, Teshima K, Shirai Y and Miyasaka T 2009 Organometal Halide Perovskites as Visible-Light Sensitizers for Photovoltaic Cells *J. Am. Chem. Soc.* **131** 6050–1

[20]   Kim H-S, Lee C-R, Im J-H, Lee K-B, Moehl T, Marchioro A, Moon S-J, Humphry-Baker R, Yum J-H, Moser J E, Grätzel M and Park N-G 2012 Lead Iodide Perovskite Sensitized All-Solid-State Submicron Thin Film Mesoscopic Solar Cell with Efficiency Exceeding 9% *Sci. Rep.* **2** 591

[21]   Min H, Lee D Y, Kim J, Kim G, Lee K S, Kim J, Paik M J, Kim Y K, Kim K S, Kim M G, Shin T J and Il Seok S 2021 Perovskite solar cells with atomically coherent interlayers on SnO2 electrodes *Nature* **598** 444–50

[22]   National Renewable Energy Laboratory Best Research-Cell Efficiency Chart

[23]   Köhnen E, Jošt M, Morales-Vilches A B, Tockhorn P, Al-Ashouri A, Macco B, Kegelmann L, Korte L, Rech B, Schlatmann R, Stannowski B and Albrecht S 2019 Highly efficient monolithic perovskite silicon tandem solar cells: Analyzing the influence of current mismatch on device performance *Sustain. Energy Fuels* **3** 1995–2005

[24]   Futscher M H and Ehrler B 2016 Efficiency Limit of Perovskite/Si Tandem Solar Cells *ACS Energy Lett.* **1** 863–8

[25]   Warmann E C and Atwater H A 2019 Predicting Geographic Energy Production for Tandem PV Designs Using a Compact Set of Spectra Correlated by Irradiance *IEEE J. Photovoltaics* **9** 1596–601

[26]   Khenkin M, Emery Q, Remec M, Erdil U, Köbler H, Li J, Abate A, Unger E, Schlatmann R and Ulbrich C 2022 Perovskite Solar Cells in Real-World Conditions: What Did We Learn from Outdoor Experiments So Far? *Proceedings of the International Conference on Hybrid and Organic Photovoltaics* (València: Fundació Scito)

[27]   Chantana J, Imai Y, Kawano Y, Hishikawa Y, Nishioka K and Minemoto T 2020 Impact of average photon energy on spectral gain and loss of various-type PV technologies at different locations *Renew. Energy* **145** 1317–24

[28]   Sharma M K and Bhattacharya J 2022 Dependence of spectral factor on angle of incidence for monocrystalline silicon based photovoltaic solar panel *Renew. Energy* **184** 820–9

[29]   Dirnberger D, Müller B and Reise C 2015 On the uncertainty of energetic impact on the yield of different PV technologies due to varying spectral irradiance *Sol. Energy* **111** 82–96

[30]   Neves G, Vilela W, Pereira E, Yamasoe M and Nofuentes G 2021 Spectral impact on PV in

low-latitude sites: The case of southeastern Brazil *Renew. Energy* **164** 1306–19

[31]   Martín N and Ruiz J M 1999 A new method for the spectral characterisation of PV modules *Prog. Photovoltaics Res. Appl.* **7** 299–310

[32]   Stark C and Theristis M 2015 The impact of atmospheric parameters on the spectral performance of multiple photovoltaic technologies *2015 IEEE 42nd Photovoltaic Specialist Conference (PVSC)* (IEEE) pp 1–5

[33]   Gueymard C A, Habte A and Sengupta M 2018 Reducing uncertainties in large-scale solar resource data: The impact of aerosols *IEEE J. Photovoltaics* **8** 1732–7

[34]   Gueymard C A 2019 The SMARTS spectral irradiance model after 25 years: New developments and validation of reference spectra *Sol. Energy* **187** 233–53

[35]   Nelson L, Frichtl M and Panchula A 2013 Changes in cadmium telluride photovoltaic system performance due to spectrum *IEEE J. Photovoltaics* **3** 488–93

[36]   Lee M, Panchula A, Solar F and Francisco S 2016 Spectral Correction for Photovoltaic Module Performance Based on Air Mass and Precipitable Water 1351–6

[37]   King D L, Kratochvil J A and Boyson W E 1997 Measuring solar spectral and angle-of-incidence effects on photovoltaic modules and solar irradiance sensors *Conf. Rec. IEEE Photovolt. Spec. Conf.* 1113–6

[38]   Betts T R, Infield D G and Gottschalg R 2004 Spectral irradiance correction for PV system yield calculations *19th EUPVSEC* 2533–6

[39]   Peng J, Lu L and Wang M 2019 A new model to evaluate solar spectrum impacts on the short circuit current of solar photovoltaic modules *Energy* 29–37

[40]   Duck B C and Fell C J 2016 Improving the spectral correction function *2016 IEEE 43rd Photovoltaic Specialists Conference (PVSC)* vol 2016-Novem (IEEE) pp 2647–52

[41]   Duck B C and Fell C J 2015 Comparison of methods for estimating the impact of spectrum on PV output *2015 IEEE 42nd Photovolt. Spec. Conf. PVSC 2015*

[42]   Marion B 2010 Preliminary Investigation of Methods for Correcting for Variations in Solar Spectrum under Clear Skies Preliminary Investigation of Methods for Correcting for Variations in Solar Spectrum under Clear Skies

[43]   Shuvro R A, Xiong J and Deng Y 2021 Spectral Correction Model Validation Using Spectroradiometer Measurements for CdTe Modules *Conf. Rec. IEEE Photovolt. Spec. Conf.* 1368–72

[44]   Bird R E 1984 A simple, solar spectral model for direct-normal and diffuse horizontal irradiance *Sol. Energy* **32** 461–71

[45]   Belluardo G, Barchi G, Baumgartner D, Rennhofer M, Weihs P and Moser D 2016 Uncertainty analysis of a radiative transfer model using Monte Carlo method within 280–2500 nm region *Sol. Energy* **132** 558–69

[46]   Xie Y, Sengupta M and Dudhia J 2016 A Fast All-sky Radiation Model for Solar applications (FARMS): Algorithm and performance evaluation *Sol. Energy* **135** 435–45

[47]   Sengupta M, Xie Y, Lopez A, Habte A, Maclaurin G and Shelby J 2018 The National Solar Radiation Data Base (NSRDB) *Renew. Sustain. Energy Rev.* **89** 51–60

[48]   Xie Y, Sengupta M and Wang C 2019 A Fast All-sky Radiation Model for Solar applications with Narrowband Irradiances on Tilted surfaces (FARMS-NIT): Part II. The cloudy-sky model *Sol. Energy* **188** 799–812

[49]   Kinsey G S 2021 Solar cell efficiency divergence due to operating spectrum variation *Sol. Energy* **217** 49–57

[50]   Sevillano-Bendezú M A, Conde L A, De La Casa J and Töfflinger J A 2022 Average photon energy assessment based on modelled spectra from the National Solar Radiation Database for Lima, Peru *J. Phys. Conf. Ser.* **2180** 0–6

[51]   Xie Y, Habte A, Sengupta M and Vignola F 2021 *An Evaluation of the Spectral Irradiance Data from the NSRDB* (Golden, CO (United States))

[52]   Rodrigo P M, Fernández E F, Almonacid F M and Pérez-Higueras P J 2017 Quantification of the spectral coupling of atmosphere and photovoltaic system performance: Indexes, methods and impact on energy harvesting *Sol. Energy Mater. Sol. Cells* **163** 73–90

[53]   Alonso-Abella M, Chenlo F, Nofuentes G and Torres-Ramírez M 2014 Analysis of spectral effects on the energy yield of different PV (photovoltaic) technologies: The case of four specific sites *Energy* **67** 435–43

[54]   Ishii T, Otani K, Itagaki A and Utsunomiya K 2013 A simplified methodology for estimating solar spectral influence on photovoltaic energy yield using average photon energy *Energy Sci. Eng.* **1** 18–26

[55]   Minemoto T, Nakada Y, Takahashi H and Takakura H 2009 Uniqueness verification of solar spectrum index of average photon energy for evaluating outdoor performance of photovoltaic modules *Sol. Energy* **83** 1294–9

[56]   Kataoka N, Yoshida S, Ueno S and Minemoto T 2014 Evaluation of solar spectral irradiance distribution using an index from a limited range of the solar spectrum *Curr. Appl. Phys.* **14** 731–7

[57]   Chantana J, Mano H, Horio Y, Hishikawa Y and Minemoto T 2017 Spectral mismatch correction factor indicated by average photon energy for precise outdoor performance measurements of different-type photovoltaic modules *Renew. Energy* **114** 567–73

[58]   Tsuji M, Rahman M M, Hishikawa Y, Nishioka K and Minemoto T 2018 Uniqueness verification of solar spectrum obtained from three sites in Japan based on similar index of average photon energy *Sol. Energy* **173** 89–96

[59]   Imai Y, Chantana J, Kawano Y, Hishikawa Y and Minemoto T 2019 Description of performance degradation of photovoltaic modules using spectral mismatch correction factor under different irradiance levels *Renew. Energy* **141** 444–50

[60]   Takeguchi K, Nakayama K, Chantana J, Kawano Y, Nishimura T, Hishikawa Y and Minemoto T 2021 Spectral gain and loss of different-type photovoltaic modules through average photon energy of various locations in Japan *Sol. Energy* **214** 1–10

[61]   Takeguchi K, Chantana J, Kawano Y, Nishimura T and Minemoto T 2022 Gaussian distribution of average photon energy and spectral gain and loss of several-type photovoltaic modules at different outdoor sites around the world *Opt. Commun.* **505** 127516

[62]   Nofuentes G, García-Domingo B, Muñoz J V. and Chenlo F 2014 Analysis of the dependence of the spectral factor of some PV technologies on the solar spectrum distribution *Appl. Energy* **113** 302–9

[63]   Markvart T 2007 Thermodynamics of losses in photovoltaic conversion *Appl. Phys. Lett.* **91** 2012–5

[64]   Markvart T 2000 Light harvesting for quantum solar energy conversion *Prog. Quantum Electron.* **24** 107–86

[65]   Markvart T 2008 Solar cell as a heat engine: Energy-entropy analysis of photovoltaic

conversion *Phys. Status Solidi Appl. Mater. Sci.* **205** 2752–6

[66]   Caballero J A, Fernandez E F, Theristis M, Almonacid F and Nofuentes G 2018 Spectral Corrections Based on Air Mass, Aerosol Optical Depth, and Precipitable Water for PV Performance Modeling *IEEE J. Photovoltaics* **8** 552–8

[67]   Cohen-Tannoudji C, Diu B and Aloë F 1977 *Quantum mechanics; 1st ed.* (New York, NY: Wiley)

[68]   Rau U 2007 Reciprocity relation between photovoltaic quantum efficiency and electroluminescent emission of solar cells *Phys. Rev. B - Condens. Matter Mater. Phys.* **76** 1–8

[69]   Tsuno Y, Hishikawa Y and Kurokawa K 2008 A method for spectral response measurements of various PV modules *23rd European Photovoltaic Solar Energy Conference* pp 2723–7

[70]   Schweiger M, Ulrich M, Nixdorf I, Rimmelspacher L, Jahn U and Herrmann W 2012 Spectral Analysis of Various Thin-Film Modules Using High Precision Spectral Response Data and Solar Spectral Irradiance Data *27th Eur. Photovolt. Sol. Energy Conf. Exhib.* 3284–90

[71]   Bliss M, Smith A, Betts T R, Baker J, De Rossi F, Bai S, Watson T, Snaith H and Gottschalg R 2019 Spectral Response Measurements of Perovskite Solar Cells *IEEE J. Photovoltaics* **9** 220–6

[72]   I. E. Commission 2008 *Photovoltaic devices - Part 3: measurement principles for terrestrial photovoltaic (PV) solar devices with reference spectral irradiance data* (IEC 60904–3 ed2)

[73]   Paudyal B R and Imenes A G 2021 Uniqueness verification of blue fraction as a parameter of spectral irradiance quantification 2563–8

[74]   Eke R, Betts T R and Gottschalg R 2017 Spectral irradiance effects on the outdoor performance of photovoltaic modules *Renew. Sustain. Energy Rev.* **69** 429–34

[75]   IEC 2008 *IEC 60904-7 Edition 3.0 Part 7: Computation of the spectral mismatch correction for measurements of photovoltaic devices*

[76]   Meydbray J, Emery K and Kurtz S 2012 Pyranometers and reference cells, the difference *PV Mag.* 108–10

[77]   Rodrigo P M, Varona J, Soria-Moya A, Almonacid-Cruz B and Fernández E F 2019 Comparative assessment of simplified indexes for the spectral characterisation of photovoltaic systems *Meas. J. Int. Meas. Confed.* **133** 1–8

[78]   Ascencio-Vásquez J, Brecl K and Topič M 2019 Methodology of Köppen-Geiger-Photovoltaic climate classification and implications to worldwide mapping of PV system performance *Sol. Energy* **191** 672–85

[79]   Ascencio Vasquez J 2019 Data for: Methodology of Köppen-Geiger-Photovoltaic climate classification and implications to Worldwide Mapping of PV System Performance

[80]   Paudyal B R, Somasundaram S G, Louwen A, Reinders A H M E, van Sark W G J H M, Stellbogen D, Ulbrich C and Imenes A G 2022 Analysis of spectral irradiance variation in northern Europe using average photon energy as a single parameter *Sol. Energy* (Submitted)

[81]   Paudyal B R and Imenes A G 2020 Analysis of spectral irradiance distribution for PV applications at high latitude *2020 47th IEEE Photovoltaic Specialists Conference (PVSC)* vol 2020-June (IEEE) pp 1834–41

[82]   Driesse, Anton and Stein J S Global normal spectral irradiance in Albuquerque: a one-year open dataset for PV research, SAND2020-12693 https://pvpmc.sandia.gov/download/7984/

[83]   Boyd M, Chen T and Dougherty B NIST Campus Photovoltaic (PV) Arrays and Weather

Station Data Sets. National Institute of Standards and Technology. U.S. Department of Commerce, Washington, D.C. [Data set]. https://doi.org/10.18434/M3S67G

[84]   Solar Radiation Monitoring Laboratory Univ. Oregon (SRML) Spectral Data http://solardat.uoregon.edu/

[85]   Andreas A and Stoffel T 1981 NREL Solar Radiation Research Laboratory (SRRL): Baseline Measurement System (BMS); Golden, Colorado (Data); NREL Report No. DA-5500-56488. https://midcdmz.nrel.gov/apps/sitehome.pl?site=BMS

[86]   Tatsiankou V, Hinzer K, Schriemer H, Kazadzis S, Kouremeti N, Gröbner J and Beal R 2018 Extensive validation of solar spectral irradiance meters at the World Radiation Center *Sol. Energy* **166** 80–9

[87]   Xie Y and Sengupta M 2018 A Fast All-sky Radiation Model for Solar applications with Narrowband Irradiances on Tilted surfaces (FARMS-NIT): Part I. The clear-sky model *Sol. Energy* **174** 691–702

[88]   Jacobson M Z and Jadhav V 2018 World estimates of PV optimal tilt angles and ratios of sunlight incident upon tilted and tracked PV panels relative to horizontal panels *Sol. Energy* **169** 55–66

[89]   F. Holmgren W, W. Hansen C and A. Mikofski M 2018 Pvlib Python: a Python Package for Modeling Solar Energy Systems *J. Open Source Softw.* **3** 884

[90]   Conde L A, Angulo J R, Sevillano-Bendezú M Á, Nofuentes G, Töfflinger J A and de la Casa J 2021 Spectral effects on the energy yield of various photovoltaic technologies in Lima (Peru) *Energy* **223** 120034

[91]   Herrmann W, Nixdorf I and Bonilla Castro J 2020 Uncertainty of PV Module Energy Rating Caused by Spectral Effects *37th Eur. Photovolt. Sol. Energy Conf. Exhib.* 816–21

[92]   Rau U, Blank B, Müller T C M and Kirchartz T 2017 Efficiency Potential of Photovoltaic Materials and Devices Unveiled by Detailed-Balance Analysis *Phys. Rev. Appl.* **7** 1–9

[93]   Shockley W and Queisser H J 1961 Detailed balance limit of efficiency of p-n junction solar cells *J. Appl. Phys.* **32** 510–9

[94]   Polo J, Alonso-Abella M, Martín-Chivelet N, Alonso-Montesinos J, López G, Marzo A, Nofuentes G and Vela-Barrionuevo N 2020 Typical Meteorological Year methodologies applied to solar spectral irradiance for PV applications *Energy* **190**

[95]   Lindig S, Moser D, Curran A J, Rath K, Khalilnejad A, French R H, Herz M, Müller B, Makrides G, Georghiou G, Livera A, Richter M, Ascencio-Vásquez J, van Iseghem M, Meftah M, Jordan D, Deline C, van Sark W, Stein J S, Theristis M, Meyers B, Baumgartner F and Luo W 2021 International collaboration framework for the calculation of performance loss rates: Data quality, benchmarks, and trends (towards a uniform methodology) *Prog. Photovoltaics Res. Appl.* **29** 573–602

[96]   Schweiger M, Herrmann W, Gerber A and Rau U 2017 Understanding the energy yield of photovoltaic modules in different climates by linear performance loss analysis of the module performance ratio *IET Renew. Power Gener.* **11** 558–65

[97]   Gottschalg R, Betts T R, Infield D G and Kearney M J 2004 On the importance of considering the incident spectrum when measuring the outdoor performance of amorphous silicon photovoltaic devices *Meas. Sci. Technol.* **15** 460–6

[98]   Minemoto T, Yamasaki K and Takakura H 2009 Relationship of Spectral Irradiance Distribution and Average Photon Energy for Analyzing the impact of Solar Spectrum on Photovoltaic Module performance *26th Eur. Photovolt. Sol. Energy Conf. Exhib.* **26** 3345–8

[99]   Polo J, Alonso-Abella M, Ruiz-Arias J A and Balenzategui J L 2017 Worldwide analysis of spectral factors for seven photovoltaic technologies *Sol. Energy* **142** 194–203

[100]   Braga M, do Nascimento L R and Rüther R 2019 Spectral modeling and spectral impacts on the performance of mc-Si and new generation CdTe photovoltaics in warm and sunny climates *Sol. Energy* **188** 976–88

[101]   Holmgren W F, Andrews R W, Lorenzo A T and Stein J S 2015 PVLIB Python 2015 *2015 IEEE 42nd Photovolt. Spec. Conf. PVSC 2015*

[102]   Nakada Y, Takahashi H, Ichida K, Minemoto T and Takakura H 2010 Influence of clearness index and air mass on sunlight and outdoor performance of photovoltaic modules *Curr. Appl. Phys.* **10** S261–4

[103]   Minemoto T, Toda M, Nagae S, Gotoh M, Nakajima A, Yamamoto K, Takakura H and Hamakawa Y 2007 Effect of spectral irradiance distribution on the outdoor performance of amorphous Si//thin-film crystalline Si stacked photovoltaic modules *Sol. Energy Mater. Sol. Cells* **91** 120–2

[104]   Minemoto T, Nagae S and Takakura H 2007 Impact of spectral irradiance distribution and temperature on the outdoor performance of amorphous Si photovoltaic modules *Sol. Energy Mater. Sol. Cells* **91** 919–23

[105]   Rodziewicz T and Rajfur M 2019 Numerical procedures and their practical application in PV modules' analyses. Part II: Useful fractions and APE *Opto-electronics Rev.* **27** 149–60

[106]   Sevillano-Bendezú M A, Khenkin M, Nofuentes G, de la Casa J, Ulbrich C and Töfflinger J A 2023 Predictability and interrelations of spectral indicators for PV performance in multiple latitudes and climates *Sol. Energy* **259** 174–87

[107]   Lee M and Panchula A F 2017 Variation in spectral correction of PV module performance based on different precipitable water estimates *2017 IEEE 44th Photovolt. Spec. Conf. PVSC 2017* 1–6

[108]   Peng J, Lu L and Wang M 2019 A new model to evaluate solar spectrum impacts on the short circuit current of solar photovoltaic modules *Energy* **169** 29–37

[109]   Passow K and Lee M 2017 Effect of spectral shift on solar PV performance *2016 IEEE Conf. Technol. Sustain. SusTech 2016* 246–50

[110]   Theristis M, Fernandez E F, Almonacid F and Perez-Higueras P 2016 Spectral Corrections Based on Air Mass, Aerosol Optical Depth, and Precipitable Water for CPV Performance Modeling *IEEE J. Photovoltaics* **6** 1598–604

[111]   Lee M, Ngan L, Hayes W, Sorensen J and Panchula A F 2015 Understanding next generation cadmium telluride photovoltaic performance due to spectrum *2015 IEEE 42nd Photovolt. Spec. Conf. PVSC 2015*

[112]   Belluardo G, Barchi G, Baumgartner D, Rennhofer M, Weihs P and Moser D 2016 Uncertainty analysis of a radiative transfer model using Monte Carlo method within 280–2500 nm region *Sol. Energy* **132** 558–69

[113]   Velilla E, Ramirez D, Uribe J I, Montoya J F and Jaramillo F 2019 Outdoor performance of perovskite solar technology: Silicon comparison and competitive advantages at different irradiances *Sol. Energy Mater. Sol. Cells* **191** 15–20

[114]   Berk A, Anderson G P, Bernstein L S, Acharya P K, Dothe H, Matthew M W, Adler-Golden S M, Chetwynd, Jr. J H, Richtsmeier S C, Pukall B, Allred C L, Jeong L S and Hoke M L 1999 MODTRAN4 radiative transfer modeling for atmospheric correction *Opt. Spectrosc. Tech. Instrum. Atmos. Sp. Res. III* **3756** 348

[115]   Emde C, Buras-Schnell R, Kylling A, Mayer B, Gasteiger J, Hamann U, Kylling J, Richter B, Pause C, Dowling T and Bugliaro L 2016 The libRadtran software package for radiative transfer calculations (version 2.0.1) *Geosci. Model Dev.* **9** 1647–72

[116]   Ricchiazzi P, Yang S, Gautier C and Sowle D 1998 SBDART: A Research and Teaching Software Tool for Plane-Parallel Radiative Transfer in the Earth's Atmosphere *Bull. Am. Meteorol. Soc.* **79** 2101–14

[117]   Rodziewicz T, Rajfur M, Teneta J, Świsłowski P and Wacławek M 2021 Modelling and analysis of the influence of solar spectrum on the efficiency of photovoltaic modules *Energy Reports* **7** 565–74